UNIVERSITY OF CALIFORNIA
Los Angeles

Studies of Comets and Active Asteroids:
From Dynamics to Physical Properties

A dissertation submitted in partial satisfaction
of the requirements for the degree
Doctor of Philosophy in Geophysics and Space Physics

by

Wentao Xu (aka Man-To Hui)

2019

ABSTRACT OF THE DISSERTATION

Studies of Comets and Active Asteroids:
From Dynamics to Physical Properties

by

Wentao Xu (aka Man-To Hui)
Doctor of Philosophy in Geophysics and Space Physics
University of California, Los Angeles, 2019
Professor David Clifford Jewitt, Chair

In order to have a better understanding of the early history of the solar system, it is scientifically important to study comets and active asteroids, which are believed to be leftovers from the formation epoch. This work presents our studies of two of the least understood families of cometary objects – active asteroids and near-Sun comets, in terms of their non-gravitational effects and physical properties. We also present a summary of our two short-term surveys specifically for Kreutz-group comets, and an examination of a widely adopted cometary nucleus-extraction technique.

We first systematically investigate the non-gravitational effects of the known active asteroids. Two of the members (313P/Gibbs & 324P/La Sagra) exhibit statistically significant non-gravitational effects, while for the remaining members we are only able to place upper limits. The result is broadly consistent with the fact that the mass loss of active asteroids is generally less than that of typical comets. Thus, previous dynamical studies of active asteroids without consideration of the non-gravitational effects are still valid, and the majority were likely formed in situ in the main belt rather than from other cometary sources.

For near-Sun comets, we conducted ground-based surveys from the Canada-France-Hawaii telescope (CFHT) and the VLT Survey Telescope (VST) in 2012 and 2014, respectively, without detection of any dwarf Kreutz-group comets. Our non-detection of two bright members which were later discovered by the *Solar and Heliospheric Observatory* (*SOHO*)

but within our CFHT search region suggests that dwarf Kreutz comets brighten much more rapidly than previously thought, or they undergo outburst at larger heliocentric distances. We also present an unprecedentedly detailed study of near-Sun comet C/2015 D1 (*SOHO*), which was the first sunskirting comet observed from the ground over the past half century. This comet disintegrated around perihelion due to excessive thermal stress within its nucleus, or to rotational instability. The enormous mass loss ($\dot{M}_{\rm N} \sim 10^5$ kg s^{-1}) caused a strong non-gravitational effect. Together with photometric measurements, the nucleus mass and radius are inferred ($M_{\rm N} \sim 10^8$-10^9 kg, $R_{\rm N} \sim$ 50-150 m), and we probe the emission of dust grains and dust-size distribution based on the morphology, as well as its composition using *SOHO* multiband observations.

Finally, we examine the nucleus-extraction technique, an important tool for revealing cometary nucleus sizes, based on which statistics of the nucleus-size distribution are established. By testing the method on our synthetic comet images, we identify an obvious systematic bias stemming from neglect of the distortion of the coma brightness profile after convolution with point-spread functions (PSF). Thus, we conclude that published nucleus-size determinations using this technique are likely invalid. Our main suggestion is to better apply the technique on high spatial resolution images of weakly active comets when the nucleus signal occupies $\gtrsim$10% of the total around the central region.

The dissertation of Wentao Xu (aka Man-To Hui) is approved.

James Bauer

Jean-Luc Margot

David A. Paige

An Yin

David Clifford Jewitt, Committee Chair

University of California, Los Angeles

2019

To my family members . . .

who have supported and encouraged me,

allowing me to pursue my dreams and achieve fulfilment

TABLE OF CONTENTS

LIST OF FIGURES

LIST OF TABLES

ACKNOWLEDGMENTS

The thesis is on the basis of three published papers and one submitted manuscript, which are listed in the following.

Chapter 2:

- M.-T. Hui & D. Jewitt (2017). *Non-Gravitational Acceleration of Active Asteroids.* AJ 153, 80

This paper is the first systematic analysis of non-gravitational effects of the active asteroids. I meticulously conducted orbit determination with thence available astrometry, whereby I obtained and evaluated their non-gravitational parameters. The contribution by coauthor David Jewitt is that he suggested the project and provided extensive suggestions on the manuscript.

Chapter 3:

- Q.-Z. Ye, M.-T. Hui, R. Kracht, & P. Wiegert. *Where are the Mini Kreutz-family Comets?* ApJ 796, 83 (2014)

The paper summarises a specific CFHT survey for dwarf Kreutz-group comets in 2012 September and October and compares pre-perihelion light curves of five Kreutz comets with heliocentric distance coverage to ∼1 AU, wherein a diversity amongst the group members is suggested. The first author Quan-Zhi Ye was the principal investigator of the CFHT survey, who wrote the proposal based on discussions with me, visually scanned the CFHT images for Kreutz comets, conducted data analysis and wrote the whole manuscript. As the second author, I measured all the astrometry and photometry of the selected *SOHO*/*STEREO* comets, performed orbit determination, visually scanned the CFHT images, and provided suggestions and comments on the manuscript. Rainer Kracht and Paul Wiegert both searched the CFHT images as well and provided comments on the manuscript.

- M.-T. Hui, Q.-Z. Ye, M. Knight, K. Battams, & D. Clark (2015). *Gone in a Blaze of Glory: the Demise of Comet C/2015 D1 (SOHO)*. ApJ 813, 73

The paper examines C/2015 D1 (*SOHO*), which was the brightest and the first sunskirting comet ever observed from the ground over the past half century, in multiple aspects including photometry, morphology, physical properties, its non-gravitational effect, and the disintegration mechanism. Being the lead author, I initiated the idea, measured astrometry of the comet in *SOHO*'s C3 images and photometry in all the *SOHO* images, determined the orbital solution, processed images from Xingming Observatory, analysed and interpreted results, including those from the coauthors, and wrote the majority of the manuscript. The contribution of each coauthor is: Quan-Zhi Ye performed morphology simulation of the comet and wrote a corresponding section, Matthew Knight attempted observations from Lowell Observatory, about which he wrote a section, verified my *SOHO* photometry measurements, and corrected for overexposed data points, Karl Battams measured astrometry of the comet in *SOHO*'s C2 images and contributed a paragraph, and David Clark searched for prediscovery observations of the comet in archival database and wrote a corresponding section.

Chapter 4:

- M.-T. Hui & J.-Y. Li (2018). *Is the Cometary Nucleus Extraction Technique Reliable?* PASP 130, 104501

The paper presents a systematic evaluation of the reliability of a widely-adopted nucleus-extraction technique for the very first time. As the first author, I wrote codes to perform all the simulation and computation, conducted the whole analysis, and wrote the manuscript. The idea of the work was originally sparked in a discussion with coauthor Jian-Yang Li, who provided extensive advice and comments, and edited the manuscript.

Herein I feel obligated to express my gratitude to quite a number of people. First and foremost, thanks to David Jewitt, my advisor, for his generous support, patience, tolerance,

and guidance that help me reach my potential as a scientist. It is a tremendous honor and fortune for me to be able to work with him, particularly under the circumstances that his name has been known to me since I was in primary school. I was dearly excited when receiving the UCLA offer that I could work with such a great mind. This eventually ended my two-year's dark time within which I kept receiving rejection letters for my applications, and occasionally I would even have quarrels with my family about my future. During my graduate career, I have benefitted a lot from discussions with him; he is so insightful that he is capable of conveying obscure concepts in a straightforward and easily understandable way, which I am still learning.

Thanks to Jing Li, Dave's wife, for her help and great food. Before I came to the US for graduate school, I had never imagined that Dave and Jing could go to LAX to pick me up, and helped me settle down. My first meal in LA was in a Vietnamese restaurant on the way from the airport to UCLA, treated by them. All of these things were like from yesterday that are vividly in my memory. I also thank Gerbs Bauer, Jean-Luc Margot, David Paige, and An Yin for serving as co-advisors, offering me guidance, and helping me overcome obstacles.

I am grateful to many astronomers, professional and amateur alike, who have been inspiring and helping me, and also treating me as a friend during science conferences. These include Jessica Agarwal, Karl Battams, Dong-Hua Chen, Xing Gao, Henry Hsieh, Yoonyoung Kim, Matthew Knight, Rainer Kracht, Yuna Grace Kwon, Jian-Yang Li, Joseph Marcus, Shigeki Murakami, Nalin Samarasinha, David Tholen, Chadwick Trujillo, Paul Wiegert, Bin Yang, Quan-Zhi Ye, Jin Zhu, and many others.

Thanks to the students, professors, researchers, and staff at UCLA who have made my graduate time so much fun. It is impossible to include everyone here, but the following people deserve special mention: Margaret Deng, Xinnan Du, Ariel Graykowski, Lauri Holbrook, Abby Kavner, Jessica Lin, Kevin McKeegan, Dave Milewski, Raquel Nuno, and Hilke Schlichting. Thanks to all my playmates from the UCLA Chinese soccer team as well, with whom I had a wonderful time fighting for triumphs, glories and champions. Without them I would have conceded far more goals.

Thanks to my Chinese calligraphy teacher, Tak-Lung Cheung, with whom I have been practising Chinese calligraphy purely for fun and interest for over two decades. To a significant degree, my characteristics, particularly perseverance and diligence, were formed under his strong influence. Also my life attitudes and temper carry uncanny resemblance to his. Sadly, he passed away in 2019 January, and could not see me degreed with a PhD. Yet his spirit will live in me for the rest of my life for sure.

Finally, thanks to my parents, and other family members for their love, encouragement, tasty food, and varieties of other support. I also take the chance to commemorate my paternal grandparents. They would be delighted to see how I progressed to where I am today, as I will soon become a PhD for the very first time in my family history.

VITA

2016	M.S. (Planetary Sciences), UCLA.
2014–present	Graduate Student Researcher and Teaching Assistant, Earth, Planetary and Space Sciences, UCLA.
2012	B.Sc. (Physics), Wuhan University.

PUBLICATIONS

Note: Only first-author publications are listed here because of the two-page limit.

Man-To Hui, Yoonyoung Kim, & Xing Gao (2019). *New Active Asteroid (6478) Gault.* Monthly Notices of the Royal Astronomical Society, under review.

Man-To Hui, Davide Farnocchia, & Marco Micheli (2019). *C/2010 U3 (Boattini): A Bizarre Comet Active at Record Heliocentric Distance.* The Astronomical Journal, Volume 157, Issue 4, article id. 162, 16 pp.

Man-To Hui & Jian-Yang Li (2018). *Is the Cometary Nucleus Extraction Technique Reliable?* Publications of the Astronomical Society of the Pacific, Volume 130, Issue 992, 10451 pp.

Man-To Hui (2018). *Two Hyperbolic Baldheads in the Solar System: 2017 U7 and 2018 C2.* The Astronomical Journal, Volume 156, Issue 2, article id. 73, 11 pp.

Man-To Hui, David Jewitt, & David Clark (2017). *Prediscovery Observations of and Orbit of Comet C/2017 K2 (PANSTARRS).* The Astronomical Journal, Volume 155, Issue 1, article id. 25, 9 pp.

Man-To Hui, David Jewitt, & Xinnan Du (2017). *Split Active Asteroid P/2016 J1 (PANSTARRS).* The Astronomical Journal, Volume 153, Issue 4, article id. 141, 8 pp.

Man-To Hui & David Jewitt (2017). *Non-gravitational Acceleration of the Active Asteroids.* The Astronomical Journal, Volume 153, Issue 2, article id. 80, 9 pp.

Man-To Hui & Jing Li (2017). *Resurrection of (3200) Phaethon in 2016.* The Astronomical Journal, Volume 153, Issue 1, article id. 23, 7 pp.

Man-To Hui, Quan-Zhi Ye, & Paul Wiegert (2017). *Constraints on Comet 332P/Ikeya-Murakami.* The Astronomical Journal, Volume 153, Issue 1, article id. 4, 10 pp.

Man-To Hui, Quan-Zhi Ye, Matthew Knight, Karl Battams, & David Clark (2015). *Gone in a Blaze of Glory: the Demise of Comet C/2015 D1 (SOHO).* The Astrophysical Journal, Volume 813, Issue 1, article id. 73, 17 pp.

Man-To Hui & David Jewitt (2015). *Archival Observations of Active Asteroid 313P/Gibbs.* The Astronomical Journal, Volume 149, Issue 4, article id. 134, 8 pp.

Man-To Hui (2013). *Observations of Comet P/2003 T12 = 2012 A3 (SOHO) at Large Phase Angle in STEREO-B.* Monthly Notices of the Royal Astronomical Society, Volume 436, Issue 2, p.1564-1575.

CHAPTER 1

Introduction

1.1 Historical Background

Comets have been fascinating to human beings for millennia. The word itself is derived from ancient Greek, κομήτης, which means "long-haired star". In other ancient civilisations, comets were addressed similarly, reflecting their most prominent characteristics – the presence of a tail. For example, ancient Chinese used "彗星" or "星孛", which mean "broom star" or "bushy star", respectively. The earliest confirmed record of a comet observation is from ancient China (Stephenson & Yau 1984):

"秋，七月，有星孛入於北斗。"

— 《春秋左傳 ·文公·文公十四年》

"*In autumn, in the seventh month, there was a comet that entered the Big Dipper.*"

— *Spring and Autumn Annals*, 14th year of Duke Wen (613 BC)

Since then, the ancient Chinese have kept over a thousand continuous records about comets, from their passage across the sky, to their appearance (e.g., Figure 1.1; Xu et al. 2000). Judging from that the ancient Chinese almost always recorded comets alongside other celestial bodies such as planets and star mansions, it is likely that they posited comets as celestial bodies rather than atmospheric phenomena such as clouds, although explicit discussions have not been found yet. It is also noteworthy that by at the latest circa 648 CE, the Chinese had been able to correctly infer that comets reflect sunlight and that the directions of the tails depend upon the viewing geometry with respect to the Sun:

"史臣案，彗體無光，傅日而為光，故夕見則東指，晨見則西指。在日南北，皆隨日光而指。頓挫其芒，或長或短，光芒所及則為災。"

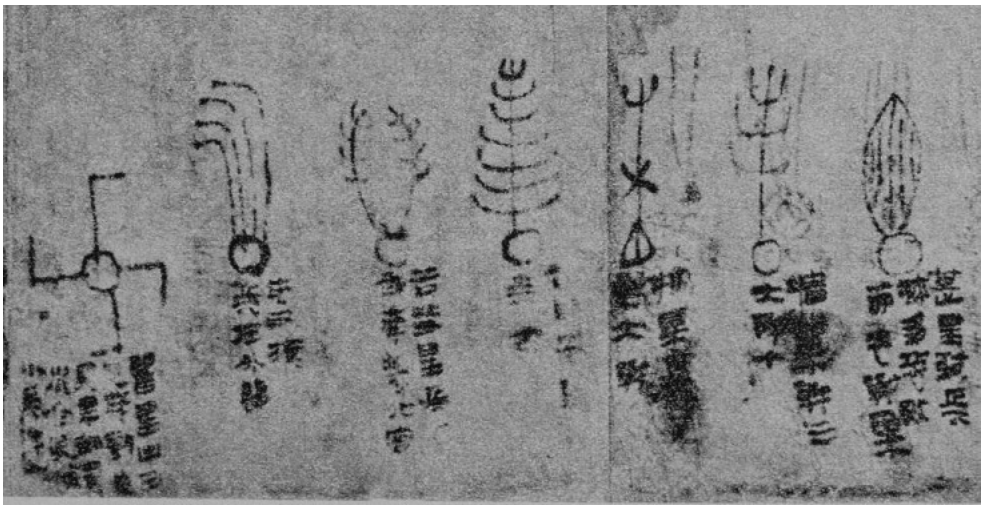

Figure 1.1: Comet in different shapes sketched on silk from BCE 2th century, unearthed from Mawangdui Tomb No. 3, Changsha, Hunan Province, China. The Chinese characters below label their various names and associated omens. From China Arts, Volume 1st, Wen Wu Publishing, Beijing, China, 1979-10.

— 《晉書·天文中》

"I as a historiographer of His Majesty note that comets do not glow, but appear to glow by reflecting sunlight, whereby in evening skies they point eastwards, and in morning skies they point westwards. If they are south or north to the Sun, the pointing as well varies with the Sun. They flicker in brightness, at times appear long, while in others appear short, and disasters descend upon wherever the ray arrives."

— *Book of Jin, Astronomy Part II*

Alas, despite these achievements, modern cometary sciences did not develop in China, but in the Western world. Inferior to the Chinese records before the Renaissance or thereabouts, the Western world have undisputedly regarded comets as some atmospheric phenomenon, possibly owing to the strong influence of Aristotle's viewpoint in his *Meteorology* (circa 330 BCE), wherein he described comets as "hot and dry exhalations" from the Earth that ascended into the atmosphere. The only person who dared to question this hypothesis and believed that comets were more like planets than atmospheric phenomenon was Seneca in

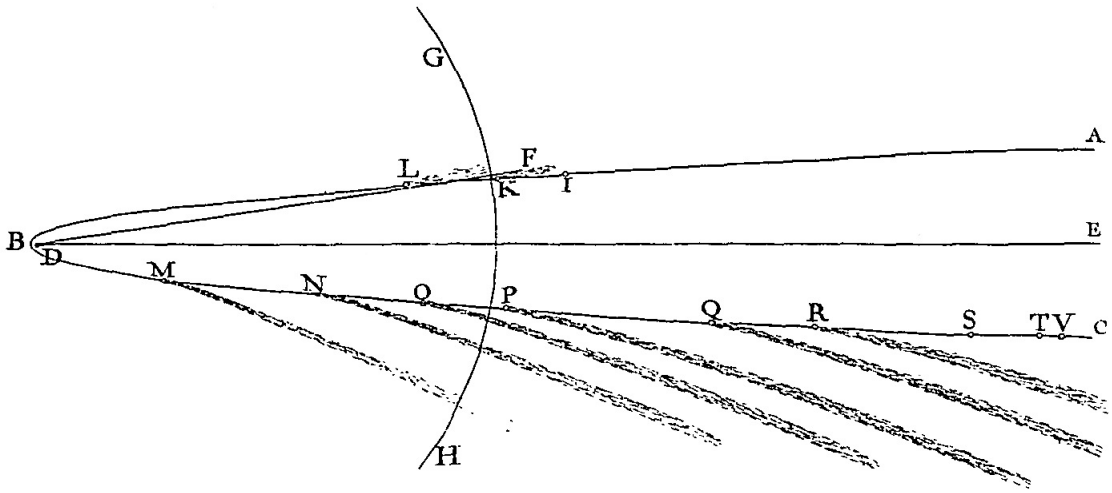

Figure 1.2: Newton's depiction of fitting the orbit of C/1680 V1 as a parabola with his theory of universal gravitation. From Newton (1687).

the first century BCE, yet this idea largely remained in obscurity until the dawn of the Renaissance. It was in the fifteenth century when Paolo dal Pozzo Toscanelli systematically observed a few comets, including the one which was now known as 1P/Halley in 1456. Later than the Chinese by nearly a millennium, or probably even more, Petrus Apianus and Girolamo Fracastoro realised that cometary tails point away from the Sun, which laid a foundation that all the efforts afterwards were trying to explain this physical behaviour of cometary tails (Heidarzadeh 2008).

The sixteenth and seventeenth centuries witnessed a couple of giant leaps in understanding of comets, and the Western world began to surpass the Chinese. Observations of comet C/1577 V1 across Europe showed no evidence about its parallax, suggesting the distance between the comet and the Earth to be even greater than the lunar distance. Thereby the Aristotelian tenet started to collapse, and people began to agree that comets were celestial bodies like planets. Later, in 1687, Isaac Newton for the first time successfully determined that the orbit of comet C/1680 V1 was a highly eccentric ellipse using the theory of universal gravitation (Figure 1.2), and verified Kepler's laws on planetary motion in his *Philosophiæ Naturalis Principia Mathematica* (Newton 1687). In 1705, Edmond Halley ap-

plied Newton's theory of gravitation and managed to link three comets in 1531, 1607 and 1682 as the same object having an orbital period of ∼76 yr. He further predicted that the comet, now named after him as 1P/Halley, would return in 1758, which proved to be correct by Johannes Palitzsch's recovery of it in 1758 December. This is a milestone because it showed that (1) the theory of gravitation is applicable not only to the planets, but also to other celestial bodies, including comets, and (2) trajectories of comets are no longer mysteriously unpredictable. Subsequently, superstitions associated with comets gradually faded away.

In the nineteenth century, as a result of accumulation of established orbits for various comets, people began to recognise that some comets had moderately eccentric orbits with low inclinations and aphelia close to Jupiter, whilst others were in highly eccentric orbits about the Sun, giving rise to an idea that comets can be classified according to their periods as either long-period or short-period comets. The latter were found to be most strongly perturbed by Jupiter, leading to a number of works on the restricted Sun-Jupiter-comet three-body problem (e.g., Tisserand 1896). Extensive observations and studies of Halley's Comet in 1835 revealed the presence of structures including jets, cones and streamers, from which Friedrich Bessel postulated that solid particles that eject from comets are subject to some unknown repulsive force and form a tail (Bessel 1836). Polarimetric and spectroscopic observations of several bright comets in the mid nineteenth century helped to confirm that comets scatter sunlight (Festou et al. 2004, and references therein). Giovanni Schiaparelli revealed that the orbits of comets 109P/Swift-Tuttle and 55P/Tempel-Tuttle closely match those of the Perseid and Leonid meteor streams, respectively, leading again to the hypothesis that comets have mass loss by ejecting solid particles, thereby forming tails. Russian astronomer Fyodor Bredikhin quantified the cometary tail model with the inclusion of a repulsive force from the Sun that varies inversely with heliocentric distance squared (Bredikhin 1903). The nature of the non-gravitational force was soon correctly depicted by Arrhenius (1900) as solar radiation pressure. This classical cometary tail model, further developed by subsequent researchers (e.g., Finson & Probstein 1968a,b), remains widely used today.

Not only the cometary grains were found to be subject to non-gravitational effects, but

also some comets such as 2P/Encke were found to be affected similarly. People noticed that their perihelion passages did not fully follow predictions using the theory of gravitation only, but would systematically deviate by some amount of time (see Festou et al. 2004, and references therein). It was until the mid twentieth century when Marsden (1969) elaborated upon a method of solving for the non-gravitational forces for the first time, which was later improved by, e.g., Marsden et al. (1973), Whipple & Sekanina 1979), Sekanina (1981, 1988), and Yeomans & Chodas (1989).

Spectroscopic studies of comets before the 1950s suggested that observed cometary species in comae were dissociated from chemically more stable species released from cometary nuclei by photochemistry (c.f. Wurm 1943; Swings 1943, and citations therein). Together with previously known facts about cometary nuclei, Whipple (1950, 1951) put forward a "dirty snowball" model, in which a cometary nucleus is actually an icy conglomerate mixed with frozen volatiles, including H_2O and CO_2, and refractory materials. As the comet approaches the Sun, the surface temperature begins to increase, causing the volatiles to sublimate, during which the refractory dust grains are dragged by the gas from the nucleus surface. This model was soon accepted by the community, validated by space missions to comets (with minor revisions though), and became the foundation for all modern models of cometary nuclei.

Around the same time, investigation by various authors of source regions of comets was carried out. These studies proposed the existence of a belt of small bodies beyond the orbit of Neptune (Edgeworth 1949; Kuiper 1951) – the Kuiper belt (or called the Edgeworth-Kuiper belt)[1], and a spherical cloud structure of cometary nuclei at heliocentric distance $r_{\rm h} \sim 10^4$-10^5 AU, which now is called the Oort cloud, and is the source of long-period comets (LPCs). It was Fernández (1980) who first predicted quantitatively that the Kuiper belt is gravitationally stable and thereby can exist in the modern solar system, and is the reservoir of short-period comets (SPCs). This was later confirmed by discoveries of several thousands of Kuiper-belt objects (KBOs) since the discovery of the first KBO (15760) Albion (formerly,

[1]It is worth to point out that Kuiper (1951) did not expect the existence of a trans-Neptunian belt in the present day solar system due to gravitational perturbations by planets, particularly Pluto, whose mass was thence seriously exaggerated.

1992 QB1) by Jewitt & Luu (1992). As for the Oort cloud, although there is no direct observational evidence, because objects therein are too distant and thus too faint, and the cloud itself is optically thin, statistics about orbital distributions of LPCs unambiguously suggest the existence of such a structure at the edge of the solar system (e.g., Marsden et al. 1978; Wiegert & Tremaine 1999; Królikowska & Dybczyński 2010).

1.2 Comet Taxonomy

LPCs and SPCs are categorised according to their orbital periods P. The division line is set at $P = 200$ yr, which is somewhat arbitrary, possibly for historical reasons. LPCs are comets with $P > 200$ yr, and SPCs are otherwise. The SPCs are further subdivided into Jupiter-family comets (JFCs) and Halley-type comets (HTCs), according to their orbital periods being shorter or longer than $P = 20$ yr, respectively. As a result of frequent encounters in the trans-planetary region, SPCs can continuously change their semimajor axes during their physical lifetimes. According to this classification system, some present-day JFCs may once have been HTCs, and vice versa. Levison (1996) took advantage of the Tisserand parameter, which is approximately an invariant in the restricted circular three-body problem, with respect to Jupiter, the most gravitationally dominant planet in the solar system, and proposed a new classification scheme. The expression of the parameter is:

$$T_{\mathrm{J}} = \frac{a_{♃}}{a} + 2\sqrt{\frac{a}{a_{♃}}\left(1 - e^2\right)}\cos i. \tag{1.1}$$

whence a, e, and i are respectively a comet's semimajor axis, eccentricity, and inclination, and those with the symbol ♃ denote Jupiter's. Note that the orbital inclination of the comet are referred to the orbital plane of Jupiter.

As Figure 1.3 shows, the two classification schemes are broadly consistent with each other. In the new scheme, JFCs, which form the dominant population of ecliptic comets ($T_{\mathrm{J}} > 2$), are the comets having $2 < T_{\mathrm{J}} < 3$, HTCs are those with $T_{\mathrm{J}} < 2$ and $a < 40$ AU, and LPCs have $T_{\mathrm{J}} < 2$ and $a \geq 40$ AU. The latter two groups belong to a larger family, which is dynamically associated with the Oort cloud, as their orbital planes are

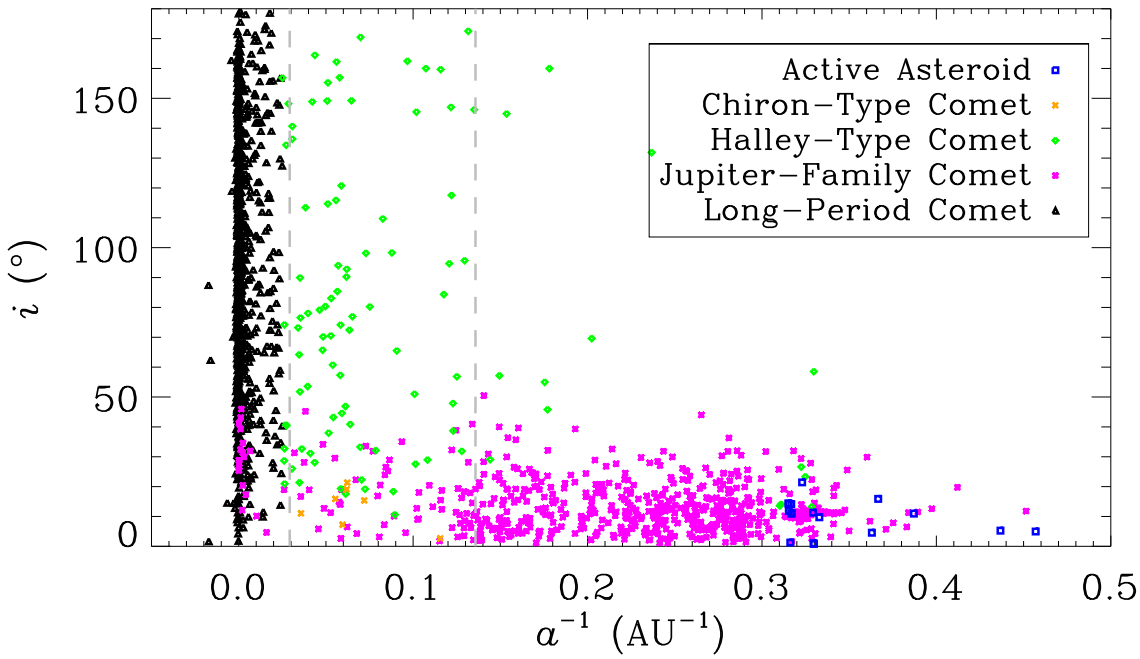

Figure 1.3: Distribution of 1,684 known comets in the reciprocal orbital semimajor axis (a^{-1}) vs inclination (i) plane. Comets with parabolic orbits ($e \equiv 1$) are not shown because their orbits are poorly determined. C/1999 U2 (*SOHO*) is not shown in the plot either, as it has a much smaller $a^{-1} < 0$. Classification of the comets (marked by different colours and symbols) is based on Levison (1996), with some tiny modifications as follows. JFCs have $e < 1$ in addition to $2 < T_{\rm J} < 3.08$, active asteroids have $0 < a < a_{♃}$ and $T_{\rm J} \geq 3.08$, Chiron-type ones are those with $T_{\rm J} \geq 3.08$ and $a > a_{♃}$, HTCs have $T_{\rm J} < 2$, $a < 40$ AU, and $e < 1$, and the remaining comets are LPCs. Otherwise, for example, there are comets in hyperbolic orbits, e.g., C/1980 E1 (Bowell), C/2010 U3 (Boattini), etc., that satisfy the definition of JFCs by Levison (1996), which makes no sense. The two vertical grey dashed lines correspond to orbital periods $P = 200$ yr (left) and 20 yr (right), respectively. Orbital elements of comets are from the JPL Small-Body Database (retrieved on 2018 May 31).

nearly isotropically distributed (see Figure 1.3). This suggests that these objects may have been formed closer to the Sun near the plane of the protoplanetary disc at the early stages of the solar system, but later were scattered by the outer planets during migration (Hahn & Malhortra 1999). As for JFCs, the origin source is suggested to be the trans-Neptunian population, as distribution of their inclinations is concentrated around the ecliptic plane (see Duncan et al. 2004, and references therein). Ecliptic comets with $T_{\rm J} > 3$ cannot intersect the orbit of Jupiter, therefore are considered to be dynamically asteroidal, and those with $a < a_{♃}$ are called active asteroids by Jewitt et al. (2015). In reality, however, because the orbit of Jupiter is not circular, and there are perturbations from other planets, plus non-gravitational effects, comets near these division lines can transition to and fro. For instance, Hsieh & Haghighpour (2016) reported that JFCs can evolve into the main-belt region by gravitationally interacting with terrestrial planets and be temporarily captured into mean-motion resonances with Jupiter on Myr timescales, although the low efficiency (∼0.1-1%) indicates that most of the active asteroids were formed in the main-belt region. As such, researchers adopted more relaxed $T_{\rm J}$ values to discriminate active asteroids and JFCs [e.g., $T_{\rm J} = 3.08$ by Jewitt et al. (2015); see Snodgrass et al. (2017) and citations therein]. The Encke-type ($a < a_{♃}$) and Chiron-type comets (a.k.a. Centaurs, $a > a_{♃}$) by Levison (1996) nevertheless are found to be associated with JFCs (Duncan et al. 2004, and references therein); the latter are thought to be in an intermediate state between KBOs and JFCs, whereas the former can evolve from JFCs due to the presence of non-gravitational effects (e.g., Fernández et al. 2002).

1.3 Cometary Reservoirs

1.3.1 Kuiper Belt

The low inclinations of the JFCs suggest that their reservoir must be a disc-like structure. Two such structures are known in the present day solar system – the main belt and the Kuiper belt. For small bodies from the former, it is gravitationally impossible to become JFCs because they have significantly $T_{\rm J} > 3$, and importantly, their orbits are interior to

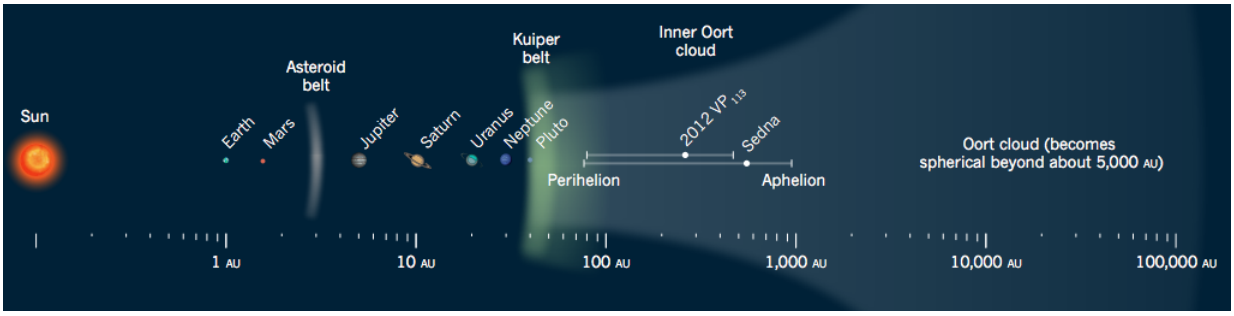

Figure 1.4: Schematic of the three known cometary repositories in the present day solar system – the main belt, the Kuiper belt, and the Oort cloud. Image extracted from Schwamb (2014).

Jupiter's. This leaves the Kuiper belt as the most likely source of JFCs. Levison & Duncan (1997) performed a detailed study about dynamical evolution of JFCs and found that indeed objects leaking from the Kuiper belt are able to form an orbital distribution that closely matches the observed one, given a physical lifetime ∼12 kyr before volatiles are exhausted.

The population in this trans-Neptunian region is traditionally divided into three sub-populations based on their orbital dynamics: the classical KBOs (CKBOs), the resonant KBOs (RKBOs), and the scattered KBOs (SKBOs). The first two are gravitationally stable, with the RKBOs trapped in major mean-motion resonances with Neptune (basically 3:4, 2:3 and 1:2), and the CKBOs in stable non-resonant orbits. As opposed to the CKBOs and RKBOs, the SKBOs are dynamically active by interacting with Neptune, thus making them much easier to evolve into JFCs.[2] In order to evolve to a JFC, the SKBO first needs to become a Uranus crosser by converting previous perihelion to aphelion, then repeat the process to become a Saturn crosser, and finally ends up being the JFC. Vice versa, a JFC can be perturbed to the intermediate state. Objects of this state are called Centaurs or Chiron-type comets, as the first recognised example was 95P/(2060) Chiron, which was discovered in 1977 as asteroidal but later found to be active.

[2]As such, some literatures do not regard SKBOs as members of the Kuiper belt, but form a structure termed the scattered disc.

1.3.2 Oort Cloud

The nearly isotropic distribution of inclinations of LPCs hints that their source – the Oort cloud must also have a spherical shape. Although hitherto the Oort cloud remains unobserved, its existence is unquestionable based on the distribution of the original semimajor axes of the known LPCs, where a prominent spike at $a \sim 10^4$-10^5 AU is seen [e.g., Figure 1 in Dones et al. (2004)]. At such great distance, the Oort-cloud objects are loosely bound to the solar system, and are subject to exterior perturbations including the galactic tide and random passing nearby stars, whereby they can be perturbed to enter the planetary region of the solar system, or become escapees. Over the history of the solar system, a fraction of $\gtrsim$10% of the Oort cloud population has been ejected by passing stellar encounters (Weissman 1980). García-Sánchez et al. (2001) used Hipparcos observations and obtained that the frequency of stellar encounters within 1 pc of the Sun is 11.7 ± 1.3 Myr^{-1}, in which 73% of the stars are M dwarfs with low masses. Yet, the major perturber of the present-day Oort cloud is the galactic disc, because its action is regular and continuous, and its perturbation magnitude is greater than that of typical passing stars. An additional suggested type of perturber is the gas molecular clouds (GMCs), which are rare but important for the long-term stability of the Oort cloud (c.f. Dones et al. 2004)

The number of comets in the Oort cloud is estimated to be 10^{11}-10^{12} in order to account for the observed flux of LPCs (Dones et al. 2004, and references therein). Given a mean mass of the LPCs $\sim 10^{13}$ kg, this corresponds to a total mass of $\sim$1-10 $M_\oplus$, where $M_\oplus \approx 6 \times 10^{24}$ kg is the mass of the Earth. The Oort-cloud objects are thought to be initially distributed much closer to the Sun at the early stage of the solar system, but were scattered by the giant planets, whose perihelion distances were lifted by the galactic tide and stochastic passing stars (Dones et al. 2004, and citations therein).

A discrepancy exists between the expected number of "dynamically old" comets (which are LPCs that reenter the planetary region, i.e., $r_{\rm h} \lesssim 15$ AU, opposed to "dynamically new" ones) and the observed one (Oort 1950), which is termed the fading problem, and is likely accounted by physical degradation due to exhaustion of volatiles or disintegration of the

LPCs (Wiegert & Tremaine 1999).

1.3.3 Main Belt

Before the discovery of 133P/Elst-Pizarro, it had been thought that the Kuiper belt and the Oort cloud were the only two cometary reservoirs in the solar system, and the main-belt region in the inner solar system was unexpected to be so, because of much higher surface temperatures around subsolar points compared to the outer solar system. However, the discovery of 133P/(7968) Elst-Pizarro in 1996 and subsequent more discoveries of similar cometary objects shattered this stereotype, leading to the recognition of the main belt as the third important cometary reservoir of the solar system (Jewitt et al. 2015; Snodgrass et al. 2017, and references therein). These cometary objects, called active asteroids [a.k.a. main-belt comets (MBCs), for those whose orbits are in the main belt and activity is likely driven by sublimation (Snodgrass et al. 2017)], are morphologically indistinguishable from typical JFCs and LPCs, but their orbits are obviously asteroidal with $T_{\rm J} > 3$, meaning that they are decoupled from Jupiter. Although gravitational interaction with the terrestrial planets and temporal capture into the mean-motion resonances with Jupiter are able to implant JFCs into main-belt-like orbits, the efficiency is as low as ∼0.1-1%, and additionally such objects are not dynamically stable over 100 Myr, making that the active asteroids were most likely formed in situ rather than evolved from other cometary sources (Hsieh & Haghighpour 2016).

Due to the proximity to the Sun, it is most likely that the active asteroids have already depleted supervolatiles such as CO and CO_2. On the contrary, water ice is able to survive in their interiors since the formation of the solar system (Schörghofer & Hsieh 2018). In order to trigger ice sublimation of the active asteroids, a fraction of the refractory mantle has to be removed by various physical mechanisms, including small-scale impact events, rotational instability, and thermal fracture. Spectrally, a significant fraction of the outer-belt asteroids have been found to show absorption features corresponding to water chemically bound within hydrated minerals (Carvano et al. 2003). Küppers et al. (2014) even reported detection of

water vapour from in situ observations of Ceres.

The greatest excitement about this newly recognised cometary repository is a potential relation between the main-belt icy objects and water of the Earth. It is widely thought that the early Earth probably required external sources to supply its otherwise escapable water due to the high temperature. Compared to JFCs, LPCs and other typical comets, the Earth subtends a much larger solid angle to the active asteroids, which means that they were more likely to collide with the Earth during the early stage of the solar system. By impact the Earth may have been supplied by volatiles from the main belt, which are vital for advent of life (Morbidelli et al. 2000), thus making the active asteroids even more interesting.

1.4 Observing Comets

Observations of comets provide us with useful information about physical properties of the targets, such as the activity level. The apparent magnitude of a comet in some wavelength λ at heliocentric distance $r_{\rm h}$, cometocentric distance Δ and phase angle α, denoted as $m_\lambda\left(r_{\rm h}, \Delta, \alpha\right)$, can be expressed in the following form:

$$m_\lambda\left(r_{\rm h}, \Delta, \alpha\right) = m_{\odot,\lambda} - 2.5\log\left[\frac{A_{\rm p}\phi\left(\alpha\right)C_{\rm e}r_\oplus^2}{\pi r_{\rm h}^2\Delta^2}\right]. \tag{1.2}$$

Here, $m_\odot$ is the apparent magnitude of the Sun at heliocentric distance $r_\oplus = 1$ AU, $A_{\rm p}$ is the geometric albedo, $C_{\rm e}$ is the effective cross-section of the comet, and ϕ is the phase function. After the changing geometry is corrected, one obtains the reduced magnitude of the comet:

$$m_\lambda\left(1,1,0\right) = m_\lambda\left(r_{\rm h}, \Delta, \alpha\right) - 5\log\left(r_{\rm h}\Delta\right) + 2.5\log\phi\left(\alpha\right). \tag{1.3}$$

The phase function $\phi\left(\alpha\right)$ can be partitioned into the contribution from the nucleus and that from the coma. Let the ratio between the effective cross-section of the coma and that of the nucleus be η. Then the phase function is simply the weighted mean as

$$\phi\left(\alpha\right) = \frac{\eta\phi_{\rm C}\left(\alpha\right) + \phi_{\rm N}\left(\alpha\right)}{\eta + 1}, \tag{1.4}$$

where subscripts C and N label coma and nucleus, respectively. For an active comet, the contribution from the nucleus is negligible in typical photometric aperture sizes, i.e., $\eta \to \infty$,

the phase function of the comet is determined by ϕ_{C}. If the comet is dormant or inactive as it ages, $\eta \approx 0$, its phase function is essentially that of the nucleus.

Empirically, an approximation scheme by Bowell et al. (1989) called the HG formalism[3] is adopted for ϕ_{N} as:

$$\phi_{\mathrm{N}} = (1-\mathscr{G})\left[\mathfrak{W}\phi_1 + (1-\mathfrak{W})\,\phi_1'\right] + \mathscr{G}\phi_2\left[\mathfrak{W}\phi_2 + (1-\mathfrak{W})\,\phi_2'\right], \tag{1.5}$$

where

$$\mathfrak{W} = \exp\left[-90.56\tan^2\left(\frac{\alpha}{2}\right)\right], \tag{1.6}$$

$$\phi_j = 1 - \frac{\mathscr{C}_j \sin\alpha}{0.119 + 1.341\sin\alpha - 0.754\sin^2\alpha}, \tag{1.7}$$

$$\phi_j' = \exp\left[-\mathscr{A}_j \tan^{\mathscr{B}_j}\left(\frac{\alpha}{2}\right)\right],\ j = 1, 2, \tag{1.8}$$

$$\mathscr{A}_1 = 3.332,\ \mathscr{A}_2 = 1.862,$$

$$\mathscr{B}_1 = 0.631,\ \mathscr{B}_2 = 1.218,$$

$$\mathscr{C}_1 = 0.986,\ \mathscr{C}_2 = 0.238.$$

As for the phase function of the coma, a good empirical approximation was given by Marcus (2007) as:

$$\phi_{\mathrm{C}} = \frac{\delta_{90}}{1+\delta_{90}}\left[k\left(\frac{1+g_{\mathrm{f}}^2}{1+g_{\mathrm{f}}^2+2g_{\mathrm{f}}\cos\alpha}\right)^{3/2} + (1-k)\left(\frac{1+g_{\mathrm{b}}^2}{1+g_{\mathrm{b}}^2+2g_{\mathrm{b}}\cos\alpha}\right)^{3/2} + \frac{1}{\delta_{90}}\right], \tag{1.9}$$

in which $\delta_{90} \geq 0$ is the ratio of the dust-to-gas intensity observed at phase angle $\alpha = 90°$, $0 \leq k \leq 1$ is a partitioning coefficient, and $g_{\mathrm{f}} > 0$ and $g_{\mathrm{b}} < 0$ are the forward- and back-scattering asymmetry factors, respectively. Based on observations of six comets, Marcus (2007) suggested $k = 0.95$, $g_{\mathrm{f}} = 0.9$ and $g_{\mathrm{b}} = -0.6$, leaving δ_{90} as the only parameter depending upon physical properties of the comet and the observing bandpass. Note that Marcus (2007) opted to normalise ϕ_{C}' at $\alpha = 90°$, whereas the HG formalism is at $\alpha = 0°$. In order to apply Equation (1.4), one needs to remove this discrepancy by renormalising either the HG formalism at $\alpha = 90°$, or Equation (1.9) at $\alpha = 0°$.

[3]Bowell et al. (1989) used H to denote the reduced magnitude and G for the slope of the phase curve. We changed the symbols respectively to $m_\lambda(1,1,0)$ and $\mathscr{G}$ to avoid ambiguity.

While a temporal change in the reduced magnitude of an inactive comet indicates that the nucleus is non-spherical or the surface has heterogeneous albedo distribution, for an active comet it typically means a temporal variation of its activity, particularly when C_{e} is increasing with time. The mass-loss rate of the comet is related to the effective cross-section of the comet, approximated by

$$\dot{M}_{\mathrm{N}} = \frac{4\rho_{\mathrm{d}}\bar{\mathfrak{a}}\dot{C}_{\mathrm{e}}}{3}, \tag{1.10}$$

if the size distribution of the cometary dust grains is unknown or only poorly constrained. Here ρ_{d} is the bulk density of the dust grains, whose mean radius is $\bar{\mathfrak{a}}$. One can perform morphology simulation to disclose the size distribution of the dust particles prior to computation of the mass-loss rate, whereby Equation (1.10) has to be replaced by a more sophisticated form (see Section 1.5.3).

In order to support the mass loss predominantly driven by sublimation of ices, a minimum active area is required, which can be used to place a lower limit to the nucleus size of the comet. We can write the energy equilibrium equation for an ice sublimating patch as

$$\frac{(1 - A_{\mathrm{B}})\, r_{\oplus}^{2} S_{\odot}}{r_{\mathrm{h}}^{2}} \cos\zeta = \epsilon\sigma_{\mathrm{SB}} T^{4} + L\,(T)\,\mathscr{U}\, m_{\mathrm{H}} Z\,(T) + \mathscr{E}_{\mathrm{c}}, \tag{1.11}$$

where A_{B} is the Bond albedo, $S_{\odot} = 1361$ W m^{-2} is the solar constant, ζ is the angle between the direction to the Sun and the surface normal, ϵ is the emissivity of the surface, $\sigma_{\mathrm{SB}} = 5.67 \times 10^{-8}$ W m^{-2} K^{-4} is the Stefan-Boltzmann constant, $L\,(T)$ and $Z\,(T)$ are respectively the latent heat and the production flux rate of sublimating substance having molecular weight $\mathscr{U}$ at temperature T, $m_{\mathrm{H}} = 1.67 \times 10^{-27}$ kg is the mass of a hydrogen atom, and $\mathscr{E}_{\mathrm{c}}$ is the energy flux conducting towards the nucleus. Here let us neglect the thermal conduction term, because cometary nuclei are porous and have extremely low conductivities, resulting in $\mathscr{E}_{\mathrm{c}}$ typically much smaller than the first two terms, which are respectively the energy flux going into thermal radiation and sublimation, for active comets (c.f. Huebner et al. 2006, and citations therein).

The production flux rate in Equation (1.11) can be solved with prior knowledge of $L\,(T)$, in combination with the Clausius-Clapeyron equation, which gives the pressure exerted by a sublimating substance as a function of temperature. Then the minimum active surface area,

denoted as $\mathscr{S}_{\rm min}$, to support the observed mass loss of the comet is simply given by

$$\mathscr{S}_{\rm min} = \frac{\dot{M}_{\rm N}}{\mathscr{U} m_{\rm H} \bar{Z}}, \tag{1.12}$$

which can be translated to a lower limit to the nucleus radius:

$$\begin{aligned} R_{\rm N} &\geq \sqrt{\frac{\mathscr{S}_{\rm min}}{4\pi}} \\ &= \sqrt{\frac{\dot{M}_{\rm N}}{4\pi \mathscr{U} m_{\rm H} \bar{Z}}}. \end{aligned} \tag{1.13}$$

Here $\bar{Z}$ is the mean production flux rate across the whole nucleus surface. If the cometary nucleus in an isothermal state, then $\bar{Z}$ can be solved from Equation (1.11) by setting $\cos\zeta = 1/4$. Its value cannot exceed the one corresponding to the subsolar point at $\zeta = 0$, where the surface temperature is also the highest in the simplified thermal model.

When close to the Sun (e.g., $r_{\rm h} < 1$ AU), the second term in the right-hand side of Equation (1.11) dominantly takes over the energy flux, whereby inequality (1.13) can be approximated by

$$R_{\rm N} \gtrsim \sqrt{\frac{\dot{M}_{\rm N} L r_{\rm h}^2}{4\pi r_{\oplus}^2 S_{\odot}}}. \tag{1.14}$$

In reality, however, one should be cautious that there is growing evidence that disintegration of the nucleus and sublimation occur simultaneously in some comets, and consequently, the observed mass loss can be much larger than supported by sublimation alone, and inequalities (1.13) or (1.14) do not necessarily yield a lower limit to the nucleus size. The presence of an icy grain halo that is formed by dirty icy grains already lifted from the nucleus surface (e.g., Combi et al. 2013) can affect such estimates in a similar way.

1.5 Dynamics of Comets

1.5.1 Motion of Cometary Nuclei

Astrometry of a comet from no fewer than three different epochs can be used to solve for its motion. Because of the measurement uncertainty, the longer the observing arc, the better

quality is its orbital solution. In an inertial reference frame, the general equation of motion of a comet in a Newtonian gravitational field can be expressed as

$$\ddot{\mathbf{r}} = -G\left[M_\odot \frac{\mathbf{r}-\mathbf{r}_\odot}{|\mathbf{r}-\mathbf{r}_\odot|^3} + \sum_{j=1}^{N} M_j \frac{\mathbf{r}-\mathbf{r}_j}{|\mathbf{r}-\mathbf{r}_j|^3}\right], \tag{1.15}$$

where $\mathbf{r}$ is the position vector of the comet with respect to the origin of the reference system, $\mathbf{r}_j$ are the position vectors of objects with masses M_j ($j = 1, 2, ..., N$), $\mathbf{r}_\odot$ is the position vector of the Sun whose mass is denoted as $M_\odot$, and G is the gravitational constant. Let $\mathbf{r}_\mathrm{h} = \mathbf{r} - \mathbf{r}_\odot$. Similarly for the Sun, its equation of motion is

$$\ddot{\mathbf{r}}_\odot = -G\sum_{j=1}^{N} M_j \frac{\mathbf{r}_\odot - \mathbf{r}_j}{|\mathbf{r}_\odot - \mathbf{r}_j|^3}, \tag{1.16}$$

where the mass of the comet, which is much smaller compared to those of other bodies, is ignored. Let $\mathbf{r}'_j = \mathbf{r}_j - \mathbf{r}_\odot$, and transform the origin to the heliocentre by subtracting Equation (1.16) from Equation (1.15), then we obtain

$$\ddot{\mathbf{r}}_\mathrm{h} = G\left[-M_\odot \frac{\mathbf{r}_\mathrm{h}}{r_\mathrm{h}^3} + \sum_{j=1}^{N} M_j \left(\frac{\mathbf{r}'_j - \mathbf{r}_\mathrm{h}}{|\mathbf{r}'_j - \mathbf{r}_\mathrm{h}|^3} - \frac{\mathbf{r}'_j}{r_j'^3}\right)\right],$$

or, dropping the primes without causing any ambiguity, since the transfer is now complete,

$$\ddot{\mathbf{r}}_\mathrm{h} = G\left[-M_\odot \frac{\mathbf{r}_\mathrm{h}}{r_\mathrm{h}^3} + \sum_{j=1}^{N} M_j \left(\frac{\mathbf{r}_j - \mathbf{r}_\mathrm{h}}{|\mathbf{r}_j - \mathbf{r}_\mathrm{h}|^3} - \frac{\mathbf{r}_j}{r_j^3}\right)\right], \tag{1.17}$$

which is the equation of motion of the comet without any external forces beyond the solar system or non-gravitational forces in the Newtonian framework. However, neglecting a relativistic correction can lead to accumulation of errors when one is performing long-term N-body integration, especially for comets with small q. Taking this into consideration, the post-Newtonian equation of motion of the comet is [see e.g., Will (2016) for the approximate form of the post-Newtonian term]:

$$\ddot{\mathbf{r}}_\mathrm{h} = G\left\{-M_\odot \frac{\mathbf{r}_\mathrm{h}}{r_\mathrm{h}^3} + \sum_{j=1}^{N} M_j \left(\frac{\mathbf{r}_j - \mathbf{r}_\mathrm{h}}{|\mathbf{r}_j - \mathbf{r}_\mathrm{h}|^3} - \frac{\mathbf{r}_j}{r_j^3}\right) + \frac{M_\odot}{c^2 r_\mathrm{h}^3}\left[\frac{4GM_\odot \mathbf{r}_\mathrm{h}}{r_\mathrm{h}} - V^2 \mathbf{r}_\mathrm{h} + 4\left(\mathbf{r}_\mathrm{h}\cdot\mathbf{V}\right)\mathbf{V}\right]\right\}. \tag{1.18}$$

Here $\mathbf{V} = \dot{\mathbf{r}}_\mathrm{h}$ is the heliocentric velocity of the cometary nucleus. For long-term evolution of the LPCs, one actually needs to add perturbations beyond the solar system, in particular the galactic tide, which is the dominant perturber. Interested readers can refer to Wiegert & Tremaine (1999) for details.

1.5.2 Non-Gravitational Effects

Since the nineteenth century, it has been known that comets, particularly those active ones, or those with small nuclei, are subject to non-gravitational effects due to anisotropic mass loss that gives rise to a recoil force. Neglecting these effects occasionally leads to failure attempts in orbit determination of these comets, or unacceptably large astrometric residuals. Marsden et al. (1973) proposed a symmetrical non-gravitational force model where the force varies proportionally with sublimation of water ice from an isothermal cometary nucleus, and is symmetric about perihelion. The expression for the non-gravitational acceleration is written as

$$\mathcal{A}_{\mathrm{R}}\hat{\mathbf{e}}_{\mathrm{R}} + \mathcal{A}_{\mathrm{T}}\hat{\mathbf{e}}_{\mathrm{T}} + \mathcal{A}_{\mathrm{N}}\hat{\mathbf{e}}_{\mathrm{N}} = \left(A_1\hat{\mathbf{e}}_{\mathrm{R}} + A_2\hat{\mathbf{e}}_{\mathrm{T}} + A_3\hat{\mathbf{e}}_{\mathrm{N}}\right) g\left(r_{\mathrm{h}}\right). \tag{1.19}$$

Here, $\mathcal{A}_{\mathrm{R}}$, $\mathcal{A}_{\mathrm{T}}$, and $\mathcal{A}_{\mathrm{N}}$ are the three components of the non-gravitational acceleration, whose magnitude is $\mathcal{A} = \sqrt{\mathcal{A}_{\mathrm{R}}^2 + \mathcal{A}_{\mathrm{T}}^2 + \mathcal{A}_{\mathrm{N}}^2}$, respectively in the heliocentric radial, transverse and normal (RTN) directions, whose unit vectors are denoted as $\hat{\mathbf{e}}_{\mathrm{R}}$, $\hat{\mathbf{e}}_{\mathrm{T}}$ and $\hat{\mathbf{e}}_{\mathrm{N}}$, respectively, A_j $(j = 1, 2, 3)$ are termed non-gravitational parameters, and $g\left(r_{\mathrm{h}}\right)$ is a dimensionless empirical momentum-transfer law having a formalism as

$$g\left(r_{\mathrm{h}}\right) = k_1 \left(\frac{r_{\mathrm{h}}}{r_0}\right)^{-k_2} \left[1 + \left(\frac{r_{\mathrm{h}}}{r_0}\right)^{k_3}\right]^{-k_4}, \tag{1.20}$$

in which, for isothermal sublimation of water ice, $r_0 = 2.808$ AU is a scaling distance, $k_2 = 2.15$, $k_3 = 5.093$, $k_4 = 4.6142$, and $k_1 = 0.111262$ is a normalisation factor making $g = 1$ at $r_{\mathrm{h}} = 1$ AU. Although $g\left(r_{\mathrm{h}}\right)$ is empirical, r_0 does appear to bear some physical meaning that it is correlated to the latent heat of sublimating substance (Sekanina & Kracht 2014, 2015). Herein it is crucial to point out a serious logical flaw in the assumption by Marsden et al. (1973) that the momentum-transfer law should not be fitted from the isothermal sublimation model of water ice because otherwise it conflicts with the presence of the non-gravitational effects.

The RTN components of the non-gravitational acceleration can be expressed in terms of a lag angle ψ, which is the angle between the radial direction and the direction of the non-gravitational acceleration, and an azimuthal angle ξ in the plane perpendicular to the

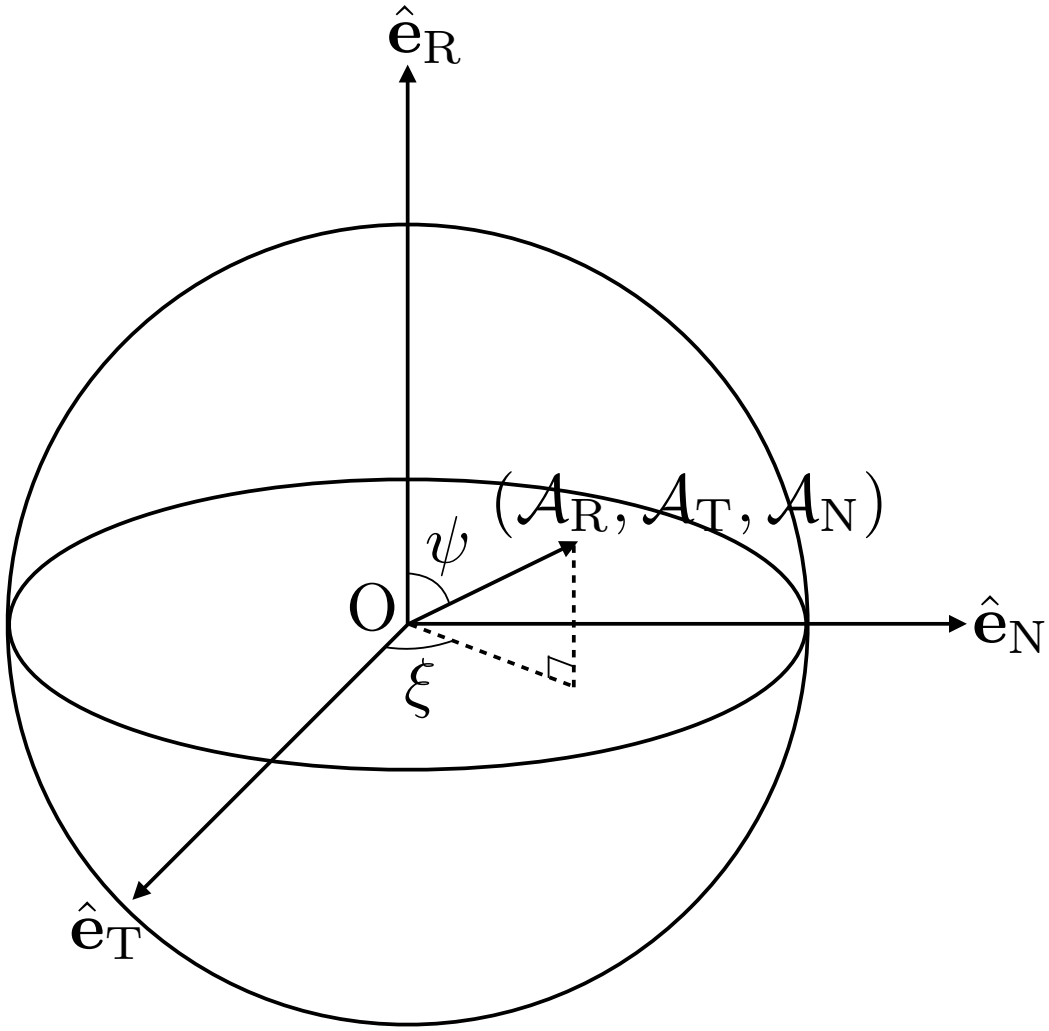

Figure 1.5: Configuration of the radial, transverse and normal (RTN) coordinate system centered at point O, the cometary nucleus. The direction of the non-gravitational acceleration is given by vector $(\mathcal{A}_{\mathrm{R}}, \mathcal{A}_{\mathrm{T}}, \mathcal{A}_{\mathrm{N}})$. The lag angle ψ and the azimuthal angle ξ are marked.

radial direction (Figure 1.5). The conversion between the two systems is as follows:

$$\begin{aligned}
\mathcal{A}_{\mathrm{R}} &= \mathcal{A}\cos\psi, \\
\mathcal{A}_{\mathrm{T}} &= \mathcal{A}\sin\psi\cos\xi, \\
\mathcal{A}_{\mathrm{N}} &= \mathcal{A}\sin\psi\sin\xi.
\end{aligned} \tag{1.21}$$

While this symmetrical non-gravitational force model has been accepted as the standard and widely applied, occasionally it fails to establish satisfactory orbital linkages. Photometric observations of some comets show that their brightness variation can be strongly asymmetric with respect to perihelion, but have a systematic shift due to the thermal inertia. Accordingly, Yeomans & Chodas (1989) introduced yet another parameter $\Delta\tau$ accounting for such an effect by replacing $g\left(r_{\mathrm{h}}\right)$ with $g\left(r'_{\mathrm{h}}\right) = g\left(r_{\mathrm{h}}\left(t+\Delta\tau\right)\right)$. Compared to the standard symmetric model, this adjustment generally improves orbital solutions.

Various space missions to comets suggest that cometary activity is highly localised on cometary nuclei, which inspired a more recent rotating-jet model (e.g., Sekanina 1988; Szutowicz 2000). The advantage of this model is that it is physically more realistic, and to some degree the spin of a cometary nucleus can be estimated (Chesley & Yeomans 2005).

The presence of the non-gravitational force results in changes of the orbit elements, most notably the change in the orbital period ΔP. Gauss' form of Lagrange's planetary equation for the change in the semimajor axis is (Danby 1992)

$$\dot{a} = \frac{P}{\pi}\left(\mathcal{A}_{\mathrm{R}}\frac{e\sin\theta}{\sqrt{1-e^2}} + \mathcal{A}_{\mathrm{T}}\frac{a\sqrt{1-e^2}}{r_{\mathrm{h}}}\right), \tag{1.22}$$

where θ is the true anomaly. Applying the chain rule, we find

$$\begin{aligned}
\dot{P} &= \frac{3P}{2a}\dot{a} \\
&= \frac{3P^2}{2\pi}\left(\mathcal{A}_{\mathrm{R}}\frac{e\sin\theta}{a\sqrt{1-e^2}} + \mathcal{A}_{\mathrm{T}}\frac{\sqrt{1-e^2}}{r_{\mathrm{h}}}\right).
\end{aligned} \tag{1.23}$$

Hence, the orbital period change over a complete orbital revolution is

$$\begin{aligned}\Delta P &= \int_0^P \dot{P}\mathrm{d}t \\ &\approx \frac{3P^2}{2\pi}\int_0^P \left(\mathcal{A}_\mathrm{R}\frac{e\sin\theta}{a\sqrt{1-e^2}} + \mathcal{A}_\mathrm{T}\frac{\sqrt{1-e^2}}{r_\mathrm{h}}\right)\mathrm{d}t. \end{aligned} \tag{1.24}$$

If the non-gravitational force is symmetric about perihelion, the first term inside the parentheses of Equation (1.24) is an odd function for $0 \leq t \leq P$, and therefore it will vanish but only the second term is left. We can see that if $\mathcal{A}_\mathrm{T} > 0$, which means that the transverse component of the non-gravitational acceleration is along the same direction as the transverse heliocentric velocity of the comet, its orbital period will increase ($\Delta P > 0$). Otherwise, we have $\Delta P < 0$, meaning that the non-gravitational effect accelerates the comet in the transverse direction. For example, 1P/Halley has an average value of $\overline{\Delta P} = +4.1$ days per perihelion return (Yeomans & Kiang 1981).

The non-gravitational effect of a comet can also provide us with insight into some physical properties of the cometary nucleus, such as its nucleus size, density, and mass loss, thanks to conservation of momentum

$$M_\mathrm{N}\mathcal{A} + \kappa\dot{M}_\mathrm{N}v = 0. \tag{1.25}$$

Here M_N is the nucleus mass, v is the effective speed of the ejected substance with respect to the cometary nucleus, and $0 < \kappa < 1$ is a dimensionless asymmetry coefficient, with the lower boundary suggesting isotropic release of the substance, and the upper one corresponding to perfectly collimated emission of material. More realistically, if the local mass flux is proportional to the solar illumination, then $k = 2/3$ (see Appendix A). In real cases, the outgassing flux is even more peaked (Rickman 1989).

Equation (1.25) can be transformed differently in accordance with various purposes. If one aims to obtain the nucleus mass as a function of time, then it yields

$$M_\mathrm{N}(t) = M_\mathrm{N}^{(0)}\exp\left[-\int_{t_0}^{t}\frac{\mathcal{A}(t')}{\kappa(t')\,v(t')}\mathrm{d}t'\right], \tag{1.26}$$

where $M_{\mathrm{N}}^{(0)}$ is the nucleus mass at some initial time t_0. Closely related, the erosion of the nucleus mass, denoted as $\mathcal{E}_{\mathrm{M}}$, is given by

$$\begin{aligned}\mathcal{E}_{\mathrm{M}}(t) &\equiv 1-\frac{M_{\mathrm{N}}(t)}{M_{\mathrm{N}}^{(0)}} \\ &= 1-\exp\left[-\int_{t_0}^{t}\frac{\mathcal{A}(t')}{\kappa(t')\,v(t')}\mathrm{d}t'\right].\end{aligned} \tag{1.27}$$

It is noteworthy that the majority of comets have their composite non-gravitational parameters $A=\sqrt{A_1^2+A_2^2+A_3^2}\lesssim 10^{-8}$ AU day^{-2}. Consequently, unless the investigated timespan is long (e.g., $t-t_0\sim 1$ kyr), it is convenient to regard M_{N} as constant values, and the mass-loss rate can be approximated by the one of dominant sublimating substance, such as water ice, having molecular weight $\mathscr{U}$. Then one can solve for the nucleus mass by changing Equation (1.25) into the following form:

$$M_{\mathrm{N}}=\frac{\kappa Q\mathscr{U}m_{\mathrm{H}}v}{\mathcal{A}}, \tag{1.28}$$

where Q is the total production rate of the volatile, and $m_{\mathrm{H}}=1.67\times 10^{-27}$ kg is the mass of a hydrogen atom. For SPCs particularly, whose multiple apparitions are observed and show changes in perihelion moments, we can estimate their mass by combining Equations (1.19), (1.21), (1.24) and (1.28). We thus obtain

$$M_{\mathrm{N}}\approx\frac{3\kappa\mathscr{U}m_{\mathrm{H}}P^2}{2\pi\Delta P}\int_0^P Q(t)\,v(t)\left(\frac{e\sin\theta\cos\psi}{a\sqrt{1-e^2}}+\frac{\sqrt{1-e^2}\sin\psi\cos\xi}{r_{\mathrm{h}}}\right)\mathrm{d}t. \tag{1.29}$$

If the production rate as a function of time varies symmetrically about perihelion, integral of the first term in the parentheses in the right-hand side of Equation (1.29) over an orbital period is zero. Yet in reality, this is often not the case; post-perihelion production rates tend to outnumber pre-perihelion ones, as it takes time for the heat wave from the Sun to penetrate into the nucleus interior.

In all, quantifying non-gravitational effects for comets is important, as this is a informative means to probe some physical properties of cometary nuclei from a dynamical perspective. The equation of motion of a cometary nucleus under the non-gravitational force is

expressed by summation of Equations (1.18) and (1.19):

$$\ddot{\mathbf{r}}_{\mathrm{h}} = G\left\{-M_{\odot}\frac{\mathbf{r}_{\mathrm{h}}}{r_{\mathrm{h}}^{3}} + \sum_{j=1}^{N} M_{j}\left(\frac{\mathbf{r}_{j}-\mathbf{r}_{\mathrm{h}}}{\left|\mathbf{r}_{j}-\mathbf{r}_{\mathrm{h}}\right|^{3}} - \frac{\mathbf{r}_{j}}{r_{j}^{3}}\right) + \frac{M_{\odot}}{c^{2}r_{\mathrm{h}}^{3}}\left[\frac{4GM_{\odot}\mathbf{r}_{\mathrm{h}}}{r_{\mathrm{h}}} - V^{2}\mathbf{r}_{\mathrm{h}} + 4\left(\mathbf{r}_{\mathrm{h}}\cdot\mathbf{V}\right)\mathbf{V}\right]\right\}$$
$$+ \mathcal{A}_{\mathrm{R}}\hat{\mathbf{e}}_{\mathrm{R}} + \mathcal{A}_{\mathrm{T}}\hat{\mathbf{e}}_{\mathrm{T}} + \mathcal{A}_{\mathrm{N}}\hat{\mathbf{e}}_{\mathrm{N}}. \tag{1.30}$$

1.5.3 Motion of Cometary Dust

Cometary dust is an irregular-shaped heterogeneous mixture of glassy silicate, crystalline grains, organic refractory material, and other minerals, which is believed to be the least thermally evolved substance surviving from the early solar nebula (Hanner & Bradley 2004). These dust grains are released from previously embedding ices during sublimation and dragged off the nucleus surface by gas flows. Most commonly, they have dimensions $\mathfrak{a} \gg 1$ μm in radius (Fulle 2004). When far from the nucleus ($\gtrsim$20 nucleus radii, where dust motion begins to be decoupled from gas drag), they lose all the near-nucleus memory about boundary conditions such as nucleus topography but form a dust tail subject to the gravitational field, mainly due to the Sun, plus radiation forces (c.f. Burns et al. 1979). The latter is comprised of two components – the dominant solar radiation pressure resulting from momentum exchange between dust grains and photons, and the secondary Poynting-Robertson (PR) drag due to the speed of light being finite.

The acceleration due to the solar radiation pressure is commonly expressed in terms of parameter β, which is the ratio between the solar radiation pressure force and the local solar gravity, thanks to the fact that the radiation pressure force varies as r_{h}^{-2} as does gravity. The parameter β is related to physical properties of cometary dust:

$$\begin{aligned}\beta &= \frac{3Q_{\mathrm{pr}}L_{\odot}}{16\pi cGM_{\odot}\rho_{\mathrm{d}}\mathfrak{a}} \\ &\equiv \frac{\mathcal{C}}{\rho_{\mathrm{d}}\mathfrak{a}},\end{aligned} \tag{1.31}$$

where Q_{pr} is the dimensionless scattering efficiency for radiation pressure, $L_{\odot} = 3.9\times10^{26}$ W is the solar luminosity at heliocentric distance $r_{\oplus} = 1$ AU, and $c \approx 3\times10^{8}$ m s^{-1} is the speed of light. Given the sizes of the dust grains, we have $Q_{\mathrm{pr}} \approx 1$ and thereby $\mathcal{C} \approx 5.95\times10^{-4}$

kg m^{-2} is roughly a constant insensitive to physical properties of the grains. Once we have constraints about the motion of dust grains of a comet, in essence we can understand some of its physical properties.

The equation of motion of cometary dust is expressed by Equation (1.18) added by the solar radiation terms:

$$\ddot{\mathbf{r}}_{\mathrm{h}} = G\left\{-M_{\odot}\frac{\mathbf{r}_{\mathrm{h}}}{r_{\mathrm{h}}^{3}} + \sum_{j=1}^{N} M_{j}\left(\frac{\mathbf{r}_{j}-\mathbf{r}_{\mathrm{h}}}{\left|\mathbf{r}_{j}-\mathbf{r}_{\mathrm{h}}\right|^{3}} - \frac{\mathbf{r}_{j}}{r_{j}^{3}}\right) + \frac{M_{\odot}}{c^{2}r_{\mathrm{h}}^{3}}\left[\frac{4GM_{\odot}\mathbf{r}_{\mathrm{h}}}{r_{\mathrm{h}}} - V^{2}\mathbf{r}_{\mathrm{h}} + 4\left(\mathbf{r}_{\mathrm{h}}\cdot\mathbf{V}\right)\mathbf{V}\right]\right\}$$
$$+\beta\frac{GM_{\odot}}{r_{\mathrm{h}}^{2}}\left[\left(1-\frac{2\mathbf{V}\cdot\hat{\mathbf{e}}_{\mathrm{R}}}{c}\right)\hat{\mathbf{e}}_{\mathrm{R}} - \left(\frac{\mathbf{V}\cdot\hat{\mathbf{e}}_{\mathrm{T}}}{c}\right)\hat{\mathbf{e}}_{\mathrm{T}}\right], \tag{1.32}$$

in which the last two terms in the right-hand side are due to the PR drag. For short-term (e.g., a few months) morphology analysis, it is convenient to ignore planetary perturbation, post-Newtonian correction, and the PR drag, as these effects usually do not contribute noticeable difference within such short timescales, and the computation time is much faster than otherwise. Therefore, one simply needs to solve for Keplerian motion of cometary dust:

$$\ddot{\mathbf{r}}_{\mathrm{h}} = \left(\beta-1\right)\frac{GM_{\odot}}{r_{\mathrm{h}}^{3}}\mathbf{r}_{\mathrm{h}}. \tag{1.33}$$

When $\beta < 1$, the dust grain orbits about the Sun in a reduced gravitational field. When $\beta = 1$, it has uniform linear motion. Otherwise, it is driven by a repulsive central force and moving in a hyperbolic trajectory (Appendix B). For a certain combination of the ejection velocity $\mathbf{V}_{\mathrm{ej}}$, β parameter, and the release epoch from the observation Δt, there is only a unique orbit for the dust grain of some comet, which can be solved rigorously (Appendix C).

Dust grains of various sizes released at a common epoch from the nucleus form loci of a synchrone, while grains of a common size (thereby subject to the same β, assuming a common ρ_{d} value) and released in a series of epochs form loci of a syndyne. The nonzero ejection speed widens syndyne and synchrone lines symmetrically about those with zero ejection speed. Hence, it is informative and convenient to apply a zeroth-order approximation where all the grains are assumed to leave the nucleus with a zero ejection speed. Results from this approach are called Finson-Probstein (FP) diagrams (Finson & Probstein 1968a, see Figure 1.6).

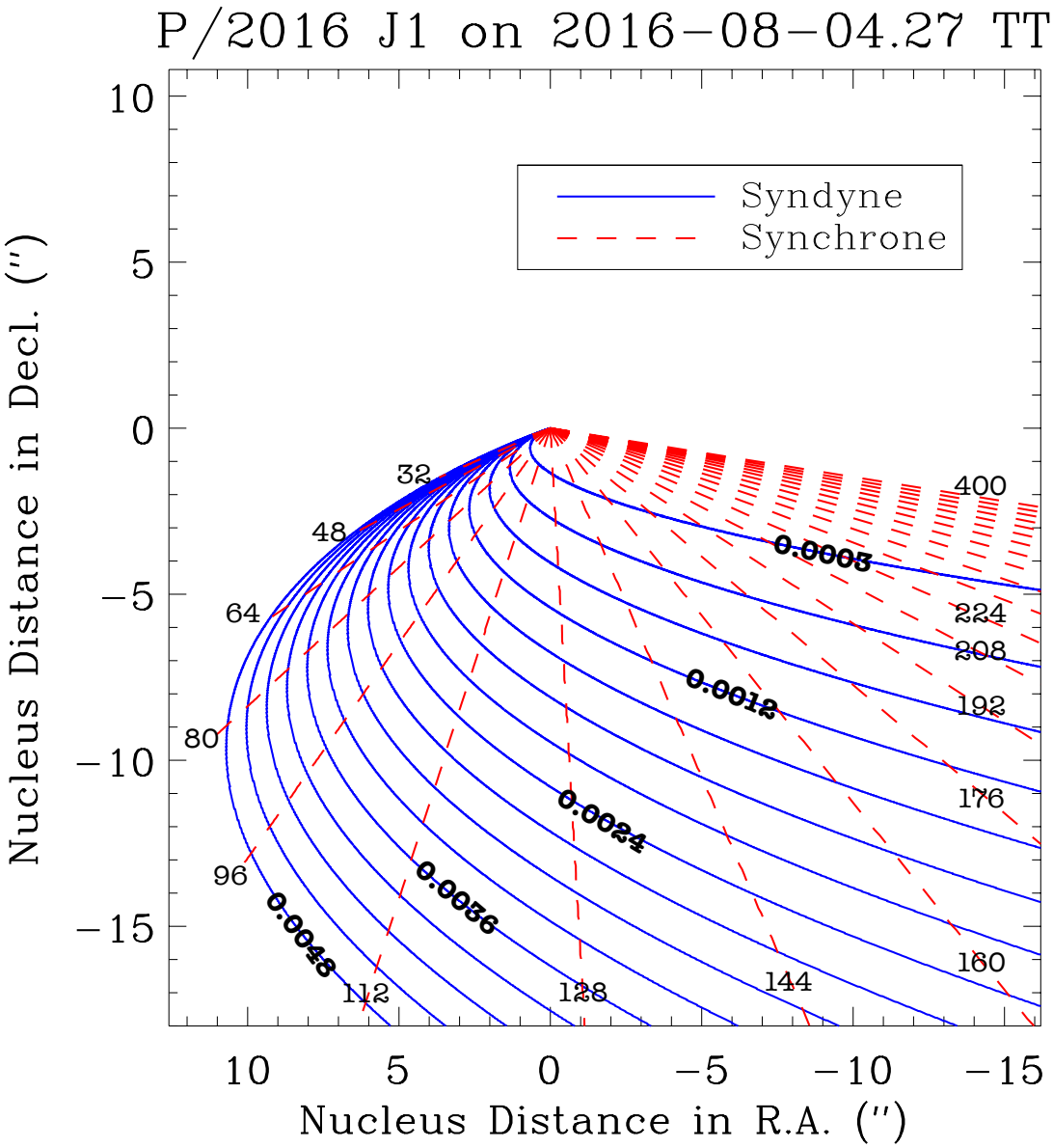

Figure 1.6: Example of application of the Finson-Probstein diagram. The plot shows syndynes (blue) and synchrones (red, values in days) of active asteroid P/2016 J1 (PANSTARRS) on TT 2016 August 04. Loci of dust grains were computed by purely solving the Keplerian motion. Reproduced from Hui et al. (2017).

Although computation of the FP diagrams does provide expedient and quantitative constraints about dust-size and release time ranges, it fails to yield information such as mass-loss rate and dust-size distribution of the grains. In real applications, we always first compute the FP diagram to constrain ranges of dust sizes and release time, and then we proceed to solve Equation (1.32), by employing our implemented version of MECURY6 (Chambers 1999), which performs N-body integration, for position vectors of the dust, later to be transformed to an observer-centric coordinate system,

The modelled image of the comet (e.g., Figure 1.7) at some CCD coordinates is given by

$$\mathcal{I} \propto \int_0^N A_{\mathrm{p}} \phi(\alpha) \left(\frac{\mathfrak{a}}{r_{\mathrm{h}} \Delta} \right)^2 \mathrm{d}N(\mathfrak{a}, t), \tag{1.34}$$

where $\mathrm{d}N(\mathfrak{a}, t)$ is the number of dust grains having radii between $\mathfrak{a}$ and $\mathfrak{a}+\mathrm{d}\mathfrak{a}$, which is often assumed to follow a power law with a constant slope index γ as $\mathrm{d}N(\mathfrak{a}, t) = \mathfrak{K}(r_{\mathrm{h}}(t))\, \mathfrak{a}^{-\gamma} \mathrm{d}\mathfrak{a}\mathrm{d}t$, for $\mathfrak{a}_{\mathrm{min}} \leq \mathfrak{a} \leq \mathfrak{a}_{\mathrm{max}}$. The parameter $\mathfrak{K}$ is primarily a function of r_{h}, which usually increases as r_{h} decreases.

The mass-loss rate of the comet can be computed as follows:

$$\begin{aligned} \dot{M}_{\mathrm{N}}(t) &= \int_{\mathfrak{a}_{\mathrm{min}}}^{\mathfrak{a}_{\mathrm{max}}} \frac{4}{3} \pi \rho_{\mathrm{d}} \mathfrak{a}^3 \frac{\mathrm{d}N(\mathfrak{a}, t)}{\mathrm{d}t} \\ &= \begin{cases} \dfrac{4\pi\rho_{\mathrm{d}} \mathfrak{K}(r_{\mathrm{h}}(t))}{3(4-\gamma)} \left(\mathfrak{a}_{\mathrm{max}}^{4-\gamma} - \mathfrak{a}_{\mathrm{min}}^{4-\gamma} \right), & \text{if } \gamma \neq 4 \\ \dfrac{4\pi\rho_{\mathrm{d}} \mathfrak{K}(r_{\mathrm{h}}(t))}{3} \ln\left(\dfrac{\mathfrak{a}_{\mathrm{max}}}{\mathfrak{a}_{\mathrm{min}}} \right), & \text{otherwise} \end{cases}. \end{aligned} \tag{1.35}$$

Then we can obtain the time-average mass-loss rate during a time interval from $t - \Delta t$ to t,

$$\overline{\dot{M}}_{\mathrm{N}} = \frac{\int_{t-\Delta t}^{t} \dot{M}_{\mathrm{N}}(t')\, \mathrm{d}t'}{\Delta t}. \tag{1.36}$$

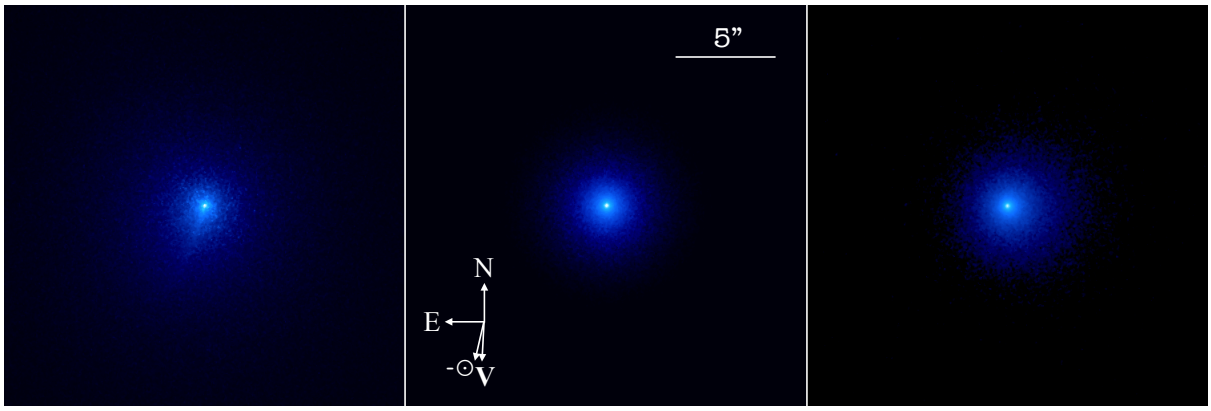

Figure 1.7: Example of morphology simulation for comet C/2017 K2 (PANSTARRS). The left two panels are modelled images whilst the right one is the observation by the *Hubble Space Telescope* (*HST*) on UT 2017 June 27. The two models both have $\gamma = 3.5$ and $\mathfrak{a}_{\rm max}$ = 2 mm, with minimum grain radii (left) $\mathfrak{a}_{\rm min}$ = 10 μm and (middle) $\mathfrak{a}_{\rm min}$ = 500 μm. Modelled ejection speeds for dust grains of 1 mm in radius are both 1.9 m s^{-1}. As shown clearly, the second model approximately matches the *HST* observation, while the first one presents a prominent tail which is absent in the observation. The dust release time is set to $\Delta t \leq 1500$ days prior to the observed epoch. A total number of $\sim 10^6$–10^7 simulated particles were generated in both simulations. Dimensions of each panel are $20'' \times 20''$. The cardinal directions and the projected antisolar ($-\odot$) direction and the heliocentric velocity vector ($\mathbf{V}$) are indicated. Taken from Hui et al. (2018).

Likewise, the effective cross-section of the comet is given by

$$C_{\rm e}\left(t\right) = \int\limits_{t-\Delta t}^{t} \int\limits_{\mathfrak{a}_{\rm min}}^{\mathfrak{a}_{\rm max}} \pi \mathfrak{a}^{2-\gamma} \mathfrak{K}\left(r_{\rm h}\left(t'\right)\right) {\rm d}\mathfrak{a}{\rm d}t'$$
$$= \begin{cases} \dfrac{\pi\left(\mathfrak{a}_{\rm max}^{3-\gamma} - \mathfrak{a}_{\rm min}^{3-\gamma}\right)}{3-\gamma} \displaystyle\int\limits_{t-\Delta t}^{t} \mathfrak{K}\left(r_{\rm h}\left(t'\right)\right) {\rm d}t', & \text{if } \gamma \neq 3 \\ \pi \ln\left(\dfrac{\mathfrak{a}_{\rm max}}{\mathfrak{a}_{\rm min}}\right) \displaystyle\int\limits_{t-\Delta t}^{t} \mathfrak{K}\left(r_{\rm h}\left(t'\right)\right) {\rm d}t', & \text{otherwise} \end{cases} . \tag{1.37}$$

To express the mass-loss rate in terms of the effective cross-section, we use Equations

(1.35) and (1.37) to eliminate $\mathfrak{K}$, and find

$$\dot{M}_{\mathrm{N}}(t) = \begin{cases} \dfrac{4\rho_{\mathrm{d}}\left(\mathfrak{a}_{\max} - \mathfrak{a}_{\min}\right)}{3} \ln^{-1}\left(\dfrac{\mathfrak{a}_{\max}}{\mathfrak{a}_{\min}}\right) \dot{C}_{\mathrm{e}}(t), & \text{if } \gamma = 3 \\ \dfrac{4\rho_{\mathrm{d}}\mathfrak{a}_{\min}\mathfrak{a}_{\max}}{3\left(\mathfrak{a}_{\max} - \mathfrak{a}_{\min}\right)} \ln\left(\dfrac{\mathfrak{a}_{\max}}{\mathfrak{a}_{\min}}\right) \dot{C}_{\mathrm{e}}(t), & \text{if } \gamma = 4 \\ \dfrac{4}{3}\rho_{\mathrm{d}}\left(\dfrac{3-\gamma}{4-\gamma}\right)\left(\dfrac{\mathfrak{a}_{\max}^{4-\gamma} - \mathfrak{a}_{\min}^{4-\gamma}}{\mathfrak{a}_{\max}^{3-\gamma} - \mathfrak{a}_{\min}^{3-\gamma}}\right) \dot{C}_{\mathrm{e}}(t), & \text{otherwise} \end{cases} . \tag{1.38}$$

Unfortunately, in most cases, parameter γ cannot be constrained with a high level of confidence, because it does not affect the morphology but the surface brightness profile [see Figure 8 in Ishiguro (2008)]. The best opportunity to unambiguously determine γ is after the activity of the comet subsides, when the decrease of the effective cross-section is mainly due to smaller-sized dust grains, which are more abundant, swept away by the solar radiation pressure more efficiently.

REFERENCES

[1] Arrhenius, S. A. 1900. Über die Ursache der Nordlichter. Phys. Zeitschr., 2, 81

[2] Bessel, F. W. 1836, Astronomische Nachrichten, 13, 185

[3] Bowell, E., Hapke, B., Domingue, D., et al. 1989, Asteroids II, eds. R. Binzel, T. Gehrels & M. Matthews, University of Arizona Press, Tucson, p. 524

[4] Burns, J. A., Lamy, P. L., & Soter, S. 1979, Icarus, 40, 1

[5] Bredikhin, F.A., 1903. Mechanische Untersuchugen über Cometformen: In systematischer Darstellung. St. Petersburg, Russia

[6] Carvano, J. M., Mothé-Diniz, T., & Lazzaro, D. 2003, Icarus, 161, 356

[7] Chambers, J. E. 1999, MNRAS, 304, 793

[8] Chesley, S. R., & Yeomans, D. K. 2005, IAU Colloq. 197: Dynamics of Populations of Planetary Systems, 289

[9] Combi, M. R., Mäkinen, J. T. T., Bertaux, J.-L., et al. 2013, Icarus, 225, 740

[10] Danby, J. M. A. 1992, Fundamentals of Celestial Mechanics (Richmond, VA, U.S.A.: Willman-Bell, Inc., 2003. 2nd ed., revised & enlarged)

[11] Dones, L., Weissman, P. R., Levison, H. F., & Duncan, M. J. 2004, Comets II, 153

[12] Duncan, M., Levison, H., & Dones, L. 2004, Comets II, M. C. Festou, H. U. Keller, and H. A. Weaver (eds.), University of Arizona Press, Tucson, 745 pp., p.193

[13] Edgeworth, K. E. 1949, MNRAS, 109, 600

[14] Fernández, J. A. 1980, MNRAS, 192, 481

[15] Fernández, J. A., Gallardo, T., & Brunini, A. 2002, Icarus, 159, 358

[16] Festou, M. C., Keller, H. U., & Weaver, H. A. 2004, Comets II, University of Arizona Press, Tucson, 2004.

[17] Finson, M. J., & Probstein, R. F. 1968a, ApJ, 154, 327

[18] Finson, M. L., & Probstein, R. F. 1968b, ApJ, 154, 353

[19] Fulle, M. 2004, Comets II, M. C. Festou, H. U. Keller, and H. A. Weaver (eds.), University of Arizona Press, Tucson, 745 pp., 565

[20] García-Sánchez, J., Weissman, P. R., Preston, R. A., et al. 2001, A&A, 379, 634

[21] Hahn, J. M., & Malhotra, R. 1999, AJ, 117, 3041

[22] Hanner, M. S., & Bradley, J. P. 2004, Comets II, University of Arizona Press, Tucson, 555

[23] Heidarzadeh, T. 2008, A History of Physical Theories of Comets, From Aristotle to Whipple, by Tofigh Heidarzadeh. ISBN 978-1-4020-8322-8. Published by Springer Science+Business Media, LLC, New York, NY USA, 2008

[24] Hsieh, H. H., & Haghighipour, N. 2016, Icarus, 277, 19

[25] Huebner, W. F., Benkhoff, J., Capria, M.-T., et al. 2006, Heat and Gas Diffusion in Comet Nuclei, by Walter F. Huebner, Johannes Benkhoff, Maria-Theresa Capria, Angioletta Coradini, Christina De Sanctis, Roberto Orosei, and Dina Prialnik. SR-004, June, 2006. ISBN 1608-280X. Published for The International Space Science Institute, Bern, Switzerland, by ESA Publications Division, Noordwijk, The Netherlands, 2006

[26] Hui, M.-T., Jewitt, D., & Du, X. 2017, AJ, 153, 141

[27] Hui, M.-T., Jewitt, D., & Clark, D. 2018, AJ, 155, 25

[28] Ishiguro, M. 2008, Icarus, 193, 96

[29] Jewitt, D., Hsieh, H., & Agarwal, J. 2015, Asteroids IV, eds. P. Michel, F. DeMeo, & W. Bottke, University of Arizona Space Science Series, 895 pp, p. 221

[30] Jewitt, D., & Luu, J. 1993, Nature, 362, 730

[31] Królikowska, M., & Dybczyński, P. A. 2010, MNRAS, 404, 1886

[32] Kuiper, G. P. 1951, Proceedings of the National Academy of Science, 37, 1

[33] Küppers, M., O'Rourke, L., Bockelée-Morvan, D., et al. 2014, Nature, 505, 525

[34] Levison, H. F. 1996, Completing the Inventory of the Solar System, 107, 173

[35] Levison, H. F., & Duncan, M. J. 1997, Icarus, 127, 13

[36] Marcus, J. N. 2007, International Comet Quarterly, 29, 39

[37] Marsden, B. G., Sekanina, Z., & Yeomans, D. K. 1973, AJ, 78, 211

[38] Marsden, B. G., Sekanina, Z., & Everhart, E. 1978, AJ, 83, 64

[39] Marsden, B. G. 1969, AJ, 74, 720

[40] Morbidelli, A., Chambers, J., Lunine, J. I., et al. 2000, Meteoritics and Planetary Science, 35, 1309

[41] Newton, I. 1687, Philosophiæ Naturalis Principia Mathematica. Auctore Js. Newton, by Newton, Isaac, 1687

[42] Oort, J. H. 1950, Bulletin of the Astronomical Institutes of the Netherlands, 11, 91

[43] Rickman, H. 1989, Advances in Space Research, 9, 59

[44] Schörghofer, N., & Hsieh, H. H. 2018, Journal of Geophysical Research (Planets), 123, 2322

[45] Schwamb, M. E. 2014, Nature, 507, 435

[46] Sekanina, Z. 1981, Annual Review of Earth and Planetary Sciences, 9, 113

[47] Sekanina, Z. 1988, AJ, 95, 911

[48] Sekanina, Z., & Kracht, R. 2014, arXiv:1404.5968

[49] Sekanina, Z., & Kracht, R. 2015, ApJ, 801, 135

[50] Snodgrass, C., Agarwal, J., Combi, M., et al. 2017, A&A Rev., 25, 5

[51] Stephenson, R., & Yau, K. 1984, New Scientist, vol. 102, pp.30-32

[52] Szutowicz, S. 2000, A&A, 363, 323

[53] Swings, P. 1943, MNRAS, 103, 86

[54] Tisserand, F. 1896, Traité de Méchanique Céleste, Gauthier-Villars, Paris, vol. 4, p. 203

[55] Weissman, P. R. 1980, Nature, 288, 242

[56] Whipple, F. L. 1950, ApJ, 111, 375

[57] Whipple, F. L. 1951, ApJ, 113, 464

[58] Whipple, F. L., & Sekanina, Z. 1979, AJ, 84, 1894

[59] Wiegert, P., & Tremaine, S. 1999, Icarus, 137, 84

[60] Will, C. M. 2016, Gravity: Where Do We Stand? ISBN 978-3-319-20223-5. Springer International Publishing Switzerland, 2016, p. 9, 9

[61] Wurm, K. 1943, Die Natur der Kometen. Mitt. der Hamburger Sternwarte in Bergedorf, 8(51), 57

[62] Xu, Z., Pankenier, D. W., & Jian, Y. 2000, East Asian Archaeoastronomy: Historical Records of Astronomical Observations of China, Japan, and Korea, Amsterdam: Gordon and Breach, 2000, ix, 430 p., 8 plates, Earth Space Institute (ESI) book series, vol. 5, ISBN 905699302X

[63] Yeomans, D. K., & Kiang, T. 1981, MNRAS, 197, 633

[64] Yeomans, D. K., & Chodas, P. W. 1989, AJ, 98, 1083

CHAPTER 2

Non-Gravitational Effects: the Case of the Active Asteroids

This chapter has been reformatted from the following published paper:

Man-To Hui & David Jewitt (2017). *Non-gravitational Acceleration of the Active Asteroids.* The Astronomical Journal, Volume 153, Issue 2, article id. 80, 9 pp.

2.1 Overview

Active asteroids have the dynamical characteristics of asteroids but exhibit transient mass loss, resulting in the production of comet-like appearance (Hsieh and Jewitt 2006). A working definition is that they are bodies which present evidence of mass loss, have semimajor axes, a, smaller than Jupiter's semimajor axis, and have Tisserand parameter with respect to Jupiter, $T_{\rm J} \geq 3.08$. There are currently $\sim$20 known active asteroids. A number of mechanisms drive the mass loss, including the likely sublimation of exposed ice, asteroid-asteroid impact, and rotational disruption probably driven by radiation torques (Jewitt 2012; Jewitt et al. 2015).

The dynamics of active asteroids are of particular interest. Numerical simulations have been conducted to study the dynamical stability of some of these objects (c.f. Jewitt et al. 2015 and citations therein). Recent work by Hsieh & Haghighipour (2016) investigated orbital evolution of test particles dynamically close to the $T_{\rm J} \simeq 3$ boundary between asteroids and comets. They found that, due to gravitational interactions with terrestrial planets and temporary trapping by mean-motion resonances with Jupiter, the fraction of the Jupiter-family comets fortuitously evolved into main-belt like orbits on Myr timescales could be as

large as ∼0.1–1%. However, most such main-belt captures would be transient, and long-term stable orbits with both small eccentricities and inclinations should be much more rare.

Non-gravitational accelerations, if present, might significantly influence the dynamics of small bodies. Fernández et al. (2002) and Levison et al. (2006) found that capture into comet 2P/Encke's orbit is possible when assisted by plausible non-gravitational forces from outgassed material, but takes much longer than the expected outgassing lifetimes of comets. They suggested that 2P/Encke might have completed this capture while spending most of its time in a dormant state. Forces due to photon momentum (the Yarkovsky effect (e.g., Chesley et al. 2003; Vokrouhlický et al. 2008; Chesley et al. 2012; Nugent et al. 2012; Farnocchia et al. 2014) and radiation pressure) are expected to be tiny compared to forces resulting from protracted anisotropic mass loss but have been detected in small asteroids.

To date, the only independently reported measurement of non-gravitational acceleration due to outgassing in an active asteroid is a 3σ detection for 133P/(7968) Elst-Pizarro (Chesley et al. 2010a). In order to develop a better understanding of the active asteroids, we attempt to measure their non-gravitational accelerations.

2.2 Data Analysis and Method

Marsden et al. (1973) developed a standard orbit determination technique with non-gravitational effects. The non-gravitational acceleration of a small body, in terms of its radial (i.e., in the antisolar direction), transverse, and normal components $\mathcal{A}_{\mathrm{R}}$, $\mathcal{A}_{\mathrm{T}}$, and $\mathcal{A}_{\mathrm{N}}$, is related to three non-gravitational parameters A_j $(j = 1, 2, 3)$, which are expressed in the same right-handed Cartesian orthogonal coordinates system by

$$\begin{pmatrix} \mathcal{A}_{\mathrm{R}} \\ \mathcal{A}_{\mathrm{T}} \\ \mathcal{A}_{\mathrm{N}} \end{pmatrix} = \begin{pmatrix} A_1 \\ A_2 \\ A_3 \end{pmatrix} \cdot g\left(r_{\mathrm{h}}\right), \tag{2.1}$$

where $g\left(r_{\mathrm{h}}\right)$ is the dimensionless standard momentum-transfer law at heliocentric distance, r_{h}, in AU. Marsden et al. (1973) defined $g(r_{\mathrm{h}})$ as:

$$g\left(r_{\mathrm{h}}\right)=k_1\left(\frac{r_{\mathrm{h}}}{r_0}\right)^{-k_2}\left[1+\left(\frac{r_{\mathrm{h}}}{r_0}\right)^{k_3}\right]^{-k_4}, \tag{2.2}$$

in which $k_2 = 2.15$, $k_3 = 5.093$, $k_4 = 4.6142$, the scaling distance $r_0 = 2.808$ AU, and the normalisation factor $k_1 = 0.111262$, such that $g = 1$ at $r_{\mathrm{h}} = 1$ AU. Accelerations $\mathcal{A}_j$ and A_j are traditionally expressed in AU day^{-2}. The momentum-transfer law comes from the assumption by Marsden et al. (1973) that the non-gravitational acceleration of a small body is proportional to the rate of sublimation of water-ice on an isothermal nucleus, with the momentum-transfer law reflecting the proportionality, such that the non-gravitational parameters A_j are always constant. (Sublimation of other materials such as sodium and forsterite can be approximated by the same formalism with different parameters (c.f. Sekanina & Kracht 2015), but the sublimation rates of these much less volatile materials are negligible compared to that of water.) In keeping with previous work, we proceed by assuming that the momentum-transfer law due to isothermal water-ice sublimation gives rise to the non-gravitational effects of the active asteroids.

We downloaded astrometric observations of all the active asteroids from the Minor Planet Center (MPC) Database Search[1], and then employed *Find_ Orb* by B. Gray for orbit determination. The code uses numerical ephemeris DE431, and includes relativistic effects due to the gravity of the Sun, and perturbations by the eight major planets. Pluto and the thirty most massive asteroids[2] are also included. Astrometric observations were debiased and weighted as described in Farnocchia et al. (2014) and Chesley et al. (2010b) before orbit determination.

We first calculated purely gravitational orbital solutions for each of the active asteroids, assuming $A_j = 0$ $(j = 1, 2, 3)$. Weights would be relaxed to be comparable with corresponding ad hoc astrometric residuals. We next rejected astrometric observations whose residuals

[1] `http://www.minorplanetcenter.net/db_search`

[2] The masses of the 30 most massive asteroids range from $\sim 7 \times 10^{18}$ kg (375 Ursula) to 9×10^{20} kg (1 Ceres). The values are based on the BC-405 asteroid ephemeris by Baer et al. (2011).

were greater than $\pm 3''.0$ from ad hoc osculating solutions, in an iterative manner. For main-belt objects, such residuals are large compared to systematic errors from the timing or plate constant solutions. They may result from centroiding errors possibly due to the faintness or non-stellar appearance of the object, from interference with background sources or adjacent cosmic rays or from other, unspecified errors. The threshold was chosen to exclude bad outliers while keeping as many data points as possible. Next, we included A_j $(j = 1, 2, 3)$ as free parameters to be obtained from the best fit orbital solutions. The procedures for filtering outliers and relaxing weights were applied iteratively until convergence was achieved. This normally took three to five runs, somewhat dependent upon the quality of data. We finally recorded the converged orbital solutions along with A_j $(j = 1, 2, 3)$.

2.3 Results

We summarize the resulting non-gravitational parameters of the active asteroids in Table 2.1. Included are statistically confident detections (SNR > 3) of non-gravitational accelerations for 324P/La Sagra in all the three components, for (3200) Phaethon in the radial direction, and for 313P/Gibbs in the transverse direction. The other active asteroids show no statistically significant evidence (SNR ≤ 3) for non-gravitational effects.

Our non-detection of the radial component of non-gravitational acceleration in 133P/(7968) Elst-Pizarro contradicts a 3σ detection reported by Chesley et al. (2010a). However, if only observations prior to 2011 are considered, our result becomes similar to that of Chesley et al. (2010a). Therefore, we conclude that the reported detection is tied to the specific astrometric dataset employed, and cannot be trusted as real. Likewise, active asteroid 259P/Garradd shows marginal evidence of a radial non-gravitational acceleration with SNR $= 2.97$ (see Table 2.1). However, the result is found to change wildly depending on the particular astrometric observations selected. Moreover, the fit to 259P/Garradd relies on the smallest number of observations (40, compared to hundreds or thousands for other objects in Table 2.1). Therefore, we do not regard it as a significant detection.

Table 2.1: Non-Gravitational Parameters of Active Asteroids

Object	A_1 (AU day^{-2})	SNR(A_1)	A_2 (AU day^{-2})	SNR(A_2)	A_3 (AU day^{-2})	SNR(A_3)	Data arc	# obs†	# opp‡	RMS ($''$)
107P	-1.15×10^{-11}	2.03	-3.56×10^{-14}	2.58	$+1.64 \times 10^{-11}$	1.97	1949–2016	909 (17)	18	0.57
133P	$+5.09 \times 10^{-10}$	2.62	$+3.63 \times 10^{-12}$	0.33	-1.14×10^{-10}	0.33	1979–2016	716 (13)	18	0.50
176P	-4.83×10^{-10}	2.64	-1.04×10^{-11}	0.42	-9.12×10^{-11}	0.18	1999–2016	568 (2)	14	0.48
238P	-4.18×10^{-8}	1.13	-3.40×10^{-8}	2.13	$+6.12 \times 10^{-12}$	$< 1\%$	2005–2011	141 (0)	4	0.59
259P	-2.88×10^{-8}	2.97	$+5.17 \times 10^{-9}$	0.70	$+1.10 \times 10^{-8}$	2.61	2008–2012	40 (6)	4	0.73
288P	-1.26×10^{-10}	0.20	$+4.69 \times 10^{-12}$	0.09	-5.31×10^{-10}	1.38	2000–2015	160 (0)	9	0.52
311P	$+2.28 \times 10^{-9}$	1.85	$+3.12 \times 10^{-11}$	2.23	-6.36×10^{-10}	1.10	2005–2015	158 (3)	5	0.45
313P	$+3.27 \times 10^{-8}$	1.75	$+2.13 \times 10^{-8}$	4.45	-4.82×10^{-9}	1.83	2003–2014	94 (3)	3	0.63
324P	-2.96×10^{-7}	10.46	-1.47×10^{-7}	10.50	-3.75×10^{-8}	7.41	2010–2015	421 (2)	4	0.48
331P	-1.09×10^{-7}	2.24	$+5.16 \times 10^{-10}$	0.87	$+6.58 \times 10^{-9}$	0.96	2004–2015	148 (10)	6	0.86
493	$+6.71 \times 10^{-11}$	0.73	-2.47×10^{-12}	1.80	$+1.74 \times 10^{-12}$	0.01	1902–2016	1388 (29)	27	0.51
596	$+7.53 \times 10^{-12}$	0.22	-1.16×10^{-12}	1.75	-1.85×10^{-10}	2.14	1908–2016	3418 (71)	41	0.40
2201	$+4.67 \times 10^{-13}$	0.15	$+2.95 \times 10^{-14}$	2.29	-3.36×10^{-12}	0.32	1931–2015	823 (23)	25	0.51
3200	$+6.97 \times 10^{-12}$	3.40	-1.44×10^{-15}	0.92	$+8.88 \times 10^{-13}$	0.59	1983–2016	3161 (60)	30	0.46
62412	$+5.20 \times 10^{-10}$	0.83	-1.53×10^{-14}	$< 1\%$	$+1.02 \times 10^{-9}$	1.08	1999–2016	737 (2)	13	0.54
P/2010 A2	-1.76×10^{-7}	1.56	$+7.97 \times 10^{-8}$	2.21	-1.10×10^{-7}	1.34	2010–2012	127 (95)	2	1.23
P/2012 T1	-6.52×10^{-6}	1.42	-1.06×10^{-6}	1.58	$+2.22 \times 10^{-7}$	1.27	2012–2013	165 (1)	1	0.45
P/2013 R3	$+1.65 \times 10^{-6}$	1.04	$+6.80 \times 10^{-7}$	1.40	-5.23×10^{-8}	2.19	2013–2014	316 (5)	1	0.63

† Total number of observations of all types (optical and radar) used in fit. Number of discarded data bracketed.

‡ Number of observed oppositions

Notes. The non-gravitational parameters are calculated based on the isothermal water-ice sublimation model devised by Marsden et al. (1973). SNR(A_j) ($j = 1, 2, 3$) is the ratio of $|A_j|$ over its 1σ uncertainty. All of the astrometric observations were retrieved on 2016 July 14–15.

2.3.1 313P/Gibbs

Hui & Jewitt (2015) previously discussed the non-gravitational motion of this ∼1 km diameter object. We did not debias the astrometric observations and simply set equal weights to all the data. Nevertheless, the result is consistent with the one in the present work in which we employed more stringent techniques to weight the data. In this sense, the detection of A_2, at 4.5σ confidence (Table 2.1) is relatively insensitive to the method by which the astrometric observations are handled. We thus conclude that it is likely a genuine detection of the transverse non-gravitational acceleration. Admittedly, in order to strengthen this conclusion, more observations of the object are desirable.

2.3.2 324P/La Sagra

324P/La Sagra shows the strongest non-gravitational acceleration of all the active asteroids, with detections $>7\sigma$ in all three components (see Table 2.1). The solutions are unlikely to be caused by contamination from undetected systematics in the astrometry because random exclusions of large subsets of the astrometric data hardly change the result. For example, discarding all the data from 2015 leads to no change in the significance of the A_j parameters. Other tests, including arbitrary assignment of equal weights to all the data, have been made, without materially changing the result. While the detection of non-gravitational acceleration appears to be secure, the solution is nevertheless somewhat puzzling. In particular, the radial component, A_1, is negative (radial non-gravitational acceleration towards the Sun), which seems physically unrealistic in the context of sublimation from the hot day-side of the nucleus. This may indicate that the applied momentum-transfer law by Marsden et al. (1973) is inappropriate to this case, because the mass-loss rate does not vary symmetrically with heliocentric distance (or, equivalently, perihelion time) as described by Equation (2.2) (see Figure 6 in Jewitt et al. (2016)). Another possibility is that it suggests a circumpolar or high-latitude active source and certain combinations of the spin-axis orientation of its nucleus (Yeomans et al. 2004).

2.3.3 (3200) Phaethon

Since the discovery in 1983, asteroid (3200) Phaethon had never been observed to show any signs of activity until 2009, 2012 and 2016 when it brightened by a factor of two around perihelion detected by the *Solar Terrestrial Relations Observatory* (*STEREO*) spacecraft (Jewitt & Li 2010; Li & Jewitt 2013; Hui & Li 2016). Intriguingly, we have a SNR = 3.4 detection for its radial non-gravitational parameter A_1, which is statistically significant. Tests such as discarding all observations prior to 1990, or applying an equal weight scheme do affect the SNR slightly, but always leave SNR ~ 3. However, we can destroy the significance of the detection by, for instance, discarding all the data from the discovery epoch to the mid-1990s. Alternatively, if a much stricter cutoff for astrometric residuals is employed (e.g. $\lesssim 1''.5$), resulting in removing observations overwhelmingly from the 1980s and early 1990s, the SNR shrinks to $\sim$2 and thus A_1 becomes insignificant. We therefore take the conservative position that the radial non-gravitational component is likely spurious.[3] This is supported by the observation that (3200) Phaethon remains inactive until it is close to the Sun, where the activity is likely triggered by some process (thermal fracture, desiccation?) other than the sublimation of water ice (Jewitt & Li 2010).

2.4 Discussion

2.4.1 Test of the Procedure

We conducted another test of the algorithms used by the orbit determination code *Find_Orb* to be sure that the software does not introduce false detections of non-gravitational motion. For this purpose, we selected a dozen asteroids $\sim$10 km in diameter and having apparent magnitudes, orbits and observational histories similar to the majority of the active asteroids. The 10 km asteroids, being $\sim 10^3$ times more massive than the mostly $\sim$1 km scale active asteroids (Table 2.3), are unlikely to exhibit any measurable non-gravitational acceleration

[3]The radar observations of Phaethon during the close encounter with the Earth in 2017 December (after this work was published) have reduced the orbital uncertainty considerably. Hanuš et al. (2018) reported a 3.6σ detection of the Yarkovsky effect of the asteroid, with A_1 consistent with ours within the noise level.

and thus serve as tests of the orbital fitting. A list of candidates was generated by the JPL Small-Body Database Search Engine[4]. We applied the same procedures and techniques described in Section 2.2 to obtain orbital solutions including A_j ($j = 1, 2, 3$) as free parameters. The results are summarized in Table 2.2.

As expected, none of the asteroids show significant ($>3\sigma$) non-gravitational parameters. Some of the active asteroids have fewer observations than have the selected moderate sized asteroids. We therefore truncated all the observations prior to 2010 for each of these asteroids and re-performed orbit determination. Again none shows detections on the non-gravitational parameters with SNR > 3. This confirms past work done with *Find_ Orb* (e.g., Micheli et al. 2014) independently showing the reliability of the code. The validity of our cutoff set at SNR $= 3$ is justified as well.

[4]`http://ssd.jpl.nasa.gov/sbdb_query.cgi`. Data retrieved on 2016 July 14.

Table 2.2: Non-Gravitational Parameters of Some Moderate-Size Asteroids

Object	A_1 (AU day^{-2})	SNR(A_1)	A_2 (AU day^{-2})	SNR(A_2)	A_3 (AU day^{-2})	SNR(A_3)	Data arc	# obs†	# opp‡	RMS ($''$)
3818	-2.73×10^{-11}	1.65	$+2.31 \times 10^{-13}$	0.62	$+3.19 \times 10^{-11}$	1.16	1979–2015	1166 (16)	20	0.49
7916	-3.29×10^{-12}	0.23	$+1.72 \times 10^{-13}$	0.61	$+2.56 \times 10^{-11}$	1.03	1978–2015	1080 (5)	18	0.53
9344	$+1.86 \times 10^{-11}$	0.58	$+1.93 \times 10^{-12}$	2.59	$+1.12 \times 10^{-10}$	2.45	1991–2016	1222 (6)	16	0.54
11313	$+6.59 \times 10^{-12}$	0.09	-1.48×10^{-12}	1.69	$+1.67 \times 10^{-10}$	1.90	1976–2016	1219 (3)	18	0.52
13426	-7.85×10^{-12}	0.45	-2.37×10^{-13}	0.86	$+1.97 \times 10^{-11}$	0.71	1975–2015	792 (2)	14	0.54
16392	-9.26×10^{-11}	1.84	-2.37×10^{-13}	0.13	$+5.85 \times 10^{-11}$	0.57	1977–2016	1085 (2)	19	0.50
18333	$+2.52 \times 10^{-11}$	1.02	-1.20×10^{-13}	0.09	$+3.83 \times 10^{-11}$	0.71	1987–2016	1100 (4)	16	0.54
20099	-6.45×10^{-12}	0.05	-5.11×10^{-12}	0.51	$+2.97 \times 10^{-11}$	0.14	1991–2015	852 (1)	17	0.49
20293	$+3.16 \times 10^{-11}$	2.09	-9.05×10^{-13}	1.66	$+6.33 \times 10^{-11}$	1.94	1980–2016	1099 (5)	15	0.52
23059	$+6.32 \times 10^{-13}$	0.05	-3.62×10^{-13}	0.76	$+1.97 \times 10^{-11}$	0.80	1991–2016	1240 (1)	15	0.47
25343	-1.36×10^{-11}	0.50	-1.66×10^{-12}	2.54	$+7.86 \times 10^{-11}$	1.95	1992–2015	866 (6)	16	0.56
26662	$+4.64 \times 10^{-11}$	1.08	-4.82×10^{-13}	0.62	$+7.31 \times 10^{-11}$	2.09	1974–2015	636 (1)	17	0.56

† Total number of observations of all types (optical and radar) used in fit. Number of discarded data bracketed.

‡ Number of observed oppositions

Notes. All of the asteroids have diameters ∼10 km. The non-gravitational parameters are calculated based on the isothermal water-ice sublimation model devised by Marsden et al. (1973). All of the astrometric observations were retrieved on 2016 July 14–15.

2.4.2 Mass-Loss Estimates

The mass-loss rate needed to provide a given non-gravitational acceleration can be estimated thanks to momentum conservation, using

$$\dot{M}_{\mathrm{N}}(t) = -\frac{M_{\mathrm{N}}(t)\, g\left(r_{\mathrm{h}}(t)\right) \sqrt{A_1^2 + A_2^2 + A_3^2}}{\kappa(t)\, v(t)}, \tag{2.3}$$

where M_{N} is the mass of the body, v is the outflow speed of the ejecta, and κ is a dimensionless factor which accounts for the collimation efficiency. The latter lies in the range $0 \leq \kappa \leq 1$, with $\kappa = 0$ for isotropic ejection and $\kappa = 1$ for perfectly collimated mass loss. We approximate the outflow speed as a function of heliocentric distance by mean thermal speed $v_{\mathrm{th}} = \sqrt{8 k_{\mathrm{B}} T / (\pi \mathscr{U} m_{\mathrm{H}})}$, where $\mathscr{U} = 18$ is the molecular mass for the water-ice sublimation scenario, $m_{\mathrm{H}} = 1.67 \times 10^{-27}$ kg is the mass of the hydrogen atom and $k_{\mathrm{B}} = 1.38 \times 10^{-23}$ J K^{-1} is the Boltzmann constant. We solve for the surface temperature, T, using the energy balance equation

$$\frac{(1 - A_{\mathrm{B}})\, S_{\odot}}{r_{\mathrm{h}}^2} \cos\zeta = \epsilon \sigma_{\mathrm{SB}} T^4 + L(T)\, \mathscr{U} m_{\mathrm{H}} Z(T) \tag{2.4}$$

in combination with the Clausius-Clapeyron relation for water ice. Here, A_{B} is the Bond albedo, $S_{\odot} = 1361$ W m^{-2} is the solar constant, $\cos\zeta$ is the effective projection factor for the surface, r_{h} is expressed in AU, ϵ is the emissivity, $\sigma_{\mathrm{SB}} = 5.67 \times 10^{-8}$ W m^{-2} K^{-4} is the Stefan-Boltzmann constant, $L(T)$ in J kg^{-1} is the latent heat of vaporization, and $Z(T)$ is the molecular production rate of the sublimating substance in s^{-1} m^{-2}. In this study, we assume $\epsilon = 1$, and $\cos\zeta = 1/4$, the latter corresponding to an isothermal nucleus, while $L(T)$ is documented in Huebner et al. (2006). The Bond albedos of the active asteroids are computed according to their geometric albedos by following the method by Bowell et al. (1989). The choice of $\cos\zeta = 1/4$ is made to remain consistent with the isothermal assumption by Marsden et al. (1973) (but see Appendix 2.A).

The collimation efficiency remains observationally unconstrained, although observations showing that cometary emissions are largely sunward suggest that small values of κ are unrealistic. We choose $\kappa \equiv 0.8$ for the sake of definiteness. Combined with Equation (2.4), the time-average mass-loss rate around the orbit can be numerically estimated by

transforming Equation (3.14) to

$$\overline{\dot{M}}_{\mathrm{N}} \simeq -\frac{\pi \rho_{\mathrm{d}} D_{\mathrm{N}}^{3} \sqrt{A_{1}^{2}+A_{2}^{2}+A_{3}^{2}}}{6 \kappa P} \int_{0}^{P} \frac{g\left(r_{\mathrm{h}}(t)\right)}{v_{\mathrm{th}}\left(r_{\mathrm{h}}(t)\right)} \mathrm{d}t, \tag{2.5}$$

where ρ_{d} is the bulk density, D_{N} is the diameter of the body, and P is the orbital period. We assume nominal density $\rho_{\mathrm{d}} = 10^{3}$ kg m^{-3} for all the active asteroids, while D_{N} is extracted from either the JPL Small-Body Database Browser or Table 2 in Jewitt et al. (2015). The results are listed in Table 2.3. We calculated the uncertainty of $\overline{\dot{M}}_{\mathrm{N}}$ solely from the covariance matrix of A_j ($j = 1, 2, 3$) based upon error propagation. For cases where objects have SNR ≤ 3 for $\overline{\dot{M}}_{\mathrm{N}}$, we list 5σ upper limits to the values.

The upper limits to mass-loss rates inferred dynamically are consistent with, but less stringent than, published mass-loss rates inferred from physical observations. Although A_2 is formally significant for 313P/Gibbs, large uncertainties in A_1 and A_3 degrade the total SNR to < 3, and therefore only a 5σ upper limit for its $\overline{\dot{M}}_{\mathrm{N}}$ is given in the table. The dynamical estimate for the mass-loss rate of 324P/La Sagra (36 ± 3 kg s^{-1}), however, exceeds values obtained from physical observations ($\sim$0.2–4 kg s^{-1}; Moreno et al. (2011), Hsieh et al. (2012), Jewitt et al. (2016)) by at least an order of magnitude. Notably, while 324P/La Sagra was active, it exhibited the highest ratio of the ejected dust mass to the nucleus mass amongst the active asteroids currently known (Hsieh 2014), suggesting an inherently higher water-ice content. Intriguingly, it is one of the active asteroids identified by Hsieh & Haghighipour (2016) as a potential captured Jupiter-family comet. This is likely correlated to our finding that 324P/La Sagra has the most significant detection in the non-gravitational acceleration. For (3200) Phaethon, since the detection of its radial non-gravitational acceleration is likely spurious, we only present a 5σ upper limit (< 200 kg s^{-1}) in Table 2.3. This weak limit is consistent with the perihelion value ($\sim$3 kg s^{-1}; Jewitt et al. 2013), as well as the average rate needed to sustain the Geminid stream over its lifetime (Jewitt et al. 2015). In neither case, however, is a firm physical interpretation possible, because it is not known how well the adopted momentum-transfer law represents mass loss that may be highly stochastic in nature.

2.4.3 Change in Orbital Elements

The presence of a non-zero non-gravitational force results in a change of the orbit. Here we proceed to study changes in the semimajor axis, a, and eccentricity, e, due to the non-gravitational effect, which can be calculated by means of Gauss' form of Lagrange's planetary equations

$$\dot{a} = \frac{P}{\pi}\left[\mathcal{A}_{\mathrm{R}}\frac{e\sin\theta}{\sqrt{1-e^2}} + \mathcal{A}_{\mathrm{T}}\frac{a\sqrt{1-e^2}}{r_{\mathrm{h}}}\right], \tag{2.6}$$

$$\dot{e} = \frac{P\sqrt{1-e^2}}{2\pi a}\left[\mathcal{A}_{\mathrm{R}}\sin\theta + \mathcal{A}_{\mathrm{T}}\left(\cos\theta + \cos E\right)\right], \tag{2.7}$$

where θ is the true anomaly, and E is the eccentric anomaly (Danby 1992). We consider their time-average values by

$$\bar{\dot{a}} \simeq \frac{A_2 a\sqrt{1-e^2}}{\pi}\int_0^P \frac{g\left(r_{\mathrm{h}}\right)}{r_{\mathrm{h}}}\mathrm{d}t, \tag{2.8}$$

$$\bar{\dot{e}} \simeq \frac{A_2\sqrt{1-e^2}}{2\pi a}\int_0^P g\left(r_{\mathrm{h}}\right)\left[\cos\theta + \frac{1}{e}\left(1-\frac{r_{\mathrm{h}}}{a}\right)\right]\mathrm{d}t, \tag{2.9}$$

Here we have assumed that all of the orbital elements are changing very slowly, such that only θ-dependent functions cannot be taken out of the integral. All the terms containing $\sin\theta$ in the right-hand side of Equations (2.6) and (2.7) are eliminated thanks to the orbital symmetry.

By substituting time t with the true anomaly θ (see Appendix 2.B), we obtain

$$\bar{\dot{a}} \simeq \frac{PA_2}{\pi^2 a}\int_0^\pi r_{\mathrm{h}} g\left(r_{\mathrm{h}}\right)\mathrm{d}\theta, \tag{2.10}$$

$$\bar{\dot{e}} \simeq \frac{PA_2}{2\pi^2 a^3}\int_0^\pi r_{\mathrm{h}}^2 g\left(r_{\mathrm{h}}\right)\left[\cos\theta + \frac{1}{e}\left(1-\frac{r_{\mathrm{h}}}{a}\right)\right]\mathrm{d}\theta, \tag{2.11}$$

Note that Equations (2.10) and (2.11) are only applicable to objects not in strong mean-motion resonances with Jupiter, the most massive planet in the solar system, because the gravitational influence from Jupiter is simply ignored. Indeed, none of the active asteroids are in strong mean-motion resonances with Jupiter. We list the results in Table 2.3. 324P/La Sagra has the most interesting result, with astoundingly large $\bar{\dot{a}}$ and $\bar{\dot{e}}$. The trend indicates that its heliocentric orbit is rapidly becoming smaller and more circular. The timescale

to drift ∼1 AU, if the non-gravitational effect is persistent, would be $\sim 10^5$ yr. Sustained dynamical evolution on this timescale means that we cannot be sure of the origin of this body, either as a short-period comet trapped from the Kuiper belt or as an icy asteroid from another part of the main-belt. On the other hand, however, its huge A_2 suggests a very short active lifetime, limited by the availability of volatiles. Using only physical observations, Jewitt et al. (2016) reported a lifetime to mass loss of $\sim 10^5$ yr and concluded that, to survive for the expected ∼0.4 Gyr collisional lifetime, the body must lie dormant for all but 0.02–0.08% of the time. In this regard, the inferences from the orbit and from physical observations are concordant.

2.4.4 Other Physical Mechanisms

We are aware that several mechanisms other than sublimation account for mass-loss from some of the active asteroids (Jewitt et al. 2015). While the Yarkovsky effect and the solar radiation pressure force can impart non-gravitational accelerations on an active asteroid in a continuous manner similar to sublimation activity, non-gravitational forces due to rotational instability and impacts obviously cannot be described by the momentum-transfer law in the formalism by Marsden et al. (1973). In particular, mass shedding from rotational instability is believed to be extremely stochastic, as evidenced by distinguishing differences in morphologies between active asteroids possibly experiencing rotational instability (311P/PANSTARRS, 331P/Gibbs, P/2010 A2, and P/2013 R3; Jewitt et al. 2015). We should not expect any detection in non-gravitational effects for these objects, because, first, there is no preference on directions of mass shedding, and second, astrometry from relatively low-resolution observations normally contains larger errors in centroiding optocenters, once there are other fragments apparently close to the primary. Indeed, we have no detections in non-gravitational effects for the active asteroids undergoing suspected rotational instability (see Table 2.1).

The momentum-transfer law by Marsden et al. (1973) also fails for active asteroids suffering from collision-induced mass loss, including (493) Griseldis (Tholen et al. 2015)

and (596) Scheila (Ishiguro et al. 2011a,b). The momentum-transfer law for impacts should instead be a Dirac delta function at the time of collision. We investigate changes in the orbital elements for these two active asteroids, considering gravity alone, by comparing the results before and after the impact for each object. No statistically significant detection of orbital change is made. We think that this is in agreement with Ishiguro et al. (2011a) that the impactor ($\sim$10 m) was much smaller than (596) Scheila ($\sim 10^2$ km). For (493) Griseldis, there is unfortunately no size estimate for the impactor.

2.4.4.1 Solar Radiation

The non-gravitational acceleration of a spherical body subjected to solar radiation pressure is given by

$$\left(\mathcal{A}_{\mathrm{R}}\right)_{\mathrm{rad}} = \frac{3\left(1 + A_{\mathrm{B}}\right) S_{\odot}}{2 c \rho_{\mathrm{d}} D_{\mathrm{N}} r_{\mathrm{h}}^{2}}, \tag{2.12}$$

where $c = 3 \times 10^8$ m s^{-1} is the speed of light, and r_{h} is expressed in AU. We examine the time-average radiation acceleration at mean heliocentric distance $\langle r_{\mathrm{h}} \rangle = a \sqrt[4]{1 - e^2}$ (see Appendix 2.B) for each active asteroid. If its source is regarded as from water-ice sublimation, the corresponding radial non-gravitational parameter is then given by $\left(\tilde{A}_1\right)_{\mathrm{rad}} \simeq \left(\overline{\mathcal{A}}_{\mathrm{R}}\right)_{\mathrm{rad}} / g\left(\langle r_{\mathrm{h}} \rangle\right)$, where $g\left(r_{\mathrm{h}}\right)$ remains unchanged from Equation (2.2).

We present the results in Table 2.3, where we can see that the observed A_1 is at least an order of magnitude larger than $\left(\tilde{A}_1\right)_{\mathrm{rad}}$. It therefore suggests that either this effect is too small among the active asteroids, or the uncertainty from the observations is too large to enable such a detection. So far only some near-earth asteroids of $\sim$10 m size have been observed to show measurable acceleration due to solar radiation pressure (e.g. Micheli et al. 2014). Therefore, we think that the influence of the solar radiation pressure on the (much larger) active asteroids is negligible.

2.4.4.2 Yarkovsky Effect

The other important physical mechanism which can give rise to a non-gravitational acceleration of a sub- or kilometer-sized asteroid is the Yarkovsky effect. Its transverse acceleration

Table 2.3: Physical and Derived Properties

Object	$D_{\mathrm{N}}^{(1)}$ (km)	$A_{\mathrm{B}}{}^{(2)}$	$-\overline{\dot{M}}_{\mathrm{N}}{}^{(3)}$ (kg s^{-1})	$\left(\overline{\mathcal{A}}_{\mathrm{R}}\right)_{\mathrm{rad}}{}^{(4)}$ (AU day^{-2})	$\left(\widetilde{A}_1\right)_{\mathrm{rad}}{}^{(5)}$ (AU day^{-2})	$\bar{\dot{a}}^{(6)}$ (AU yr^{-1})	$\bar{\dot{e}}^{(7)}$ (yr^{-1})
107P	3.5	0.02	< 5	1.82×10^{-14}	5.06×10^{-13}	-1.9×10^{-9}	-2.7×10^{-10}
133P	3.8	0.02	< 4	9.26×10^{-15}	1.14×10^{-11}	$+3.2 \times 10^{-9}$	$+6.5 \times 10^{-10}$
176P	4.0	0.02	< 5	8.68×10^{-15}	1.24×10^{-11}	-1.2×10^{-8}	-2.5×10^{-9}
238P	0.8	0.02	< 13	4.48×10^{-14}	4.76×10^{-11}	-9.9×10^{-5}	-2.0×10^{-5}
259P	0.6	0.02	< 32	8.25×10^{-14}	8.35×10^{-12}	$+6.7 \times 10^{-5}$	$+1.3 \times 10^{-5}$
288P	3	0.02	< 8	1.26×10^{-14}	8.14×10^{-12}	$+9.5 \times 10^{-9}$	$+2.0 \times 10^{-9}$
311P	< 0.5	0.11	< 1	$> 1.59 \times 10^{-13}$	$> 2.56 \times 10^{-12}$	$+3.1 \times 10^{-7}$	$+4.1 \times 10^{-8}$
313P	1.0	0.02	< 12	3.59×10^{-14}	3.76×10^{-11}	$+5.4 \times 10^{-5}$	$+1.1 \times 10^{-5}$
324P	1.1	0.02	36 ± 3	3.31×10^{-14}	2.95×10^{-11}	-1.4×10^{-4}	-2.8×10^{-5}
331P	1.8	0.02	$\lesssim 77$	2.13×10^{-14}	1.28×10^{-11}	$+2.1 \times 10^{-7}$	$+2.0 \times 10^{-8}$
493	46.4	0.02	$\lesssim 10^3$	7.81×10^{-16}	7.84×10^{-13}	-2.7×10^{-9}	-5.5×10^{-10}
596	113.3	0.01	$\lesssim 10^5$	3.60×10^{-16}	1.30×10^{-13}	-2.2×10^{-9}	-4.5×10^{-10}
2201	1.8	0.17	< 2	6.68×10^{-14}	3.81×10^{-13}	$+2.8 \times 10^{-9}$	$+3.8 \times 10^{-10}$
3200	5.1	0.04	< 200	9.36×10^{-14}	6.66×10^{-14}	-9.4×10^{-10}	-2.6×10^{-10}
62412	7.8	0.03	< 70	4.51×10^{-15}	5.87×10^{-12}	-4.6×10^{-12}	-7.3×10^{-13}
P/2010 A2	0.12	0.04	< 1	5.65×10^{-13}	1.29×10^{-11}	$+6.5 \times 10^{-4}$	$+9.8 \times 10^{-5}$
P/2012 T1	2.4	0.02	$\lesssim 10^4$	1.49×10^{-14}	1.57×10^{-11}	-2.5×10^{-3}	-5.2×10^{-4}
P/2013 R3	< 0.4	0.02	< 141	$> 9.77 \times 10^{-14}$	$> 5.09 \times 10^{-11}$	$+3.3 \times 10^{-3}$	$+6.7 \times 10^{-4}$

(1) Diameter

(2) Bond albedo

(3) Time-average mass-loss rate estimated from Equation (2.5)

(4) Computed non-gravitational acceleration due to the solar radiation force

(5) Radial non-gravitational parameter due to the solar radiation force but computed with the momentum-transfer law by Marsden et al. (1973)

(6) Time-average drift in semimajor axis

(7) Time-average drift in eccentricity

Notes. The significance levels of an orbital drift in a and e are predominantly determined by the ones of the non-gravitational parameters, which are the most uncertain parameters compared to the rest orbital elements. See Equations (2.10) and (2.11). Therefore, the SNRs of $\bar{\dot{a}}$ and $\bar{\dot{e}}$ are both given by SNR(A_2), listed in Table 2.1.

is given by

$$
\begin{aligned}
|(\mathcal{A}_{\mathrm{T}})_{\mathrm{Y}}| &= C_{\mathrm{Y}} \frac{\epsilon \sigma_{\mathrm{SB}} T^3}{c \rho_{\mathrm{d}} D_{\mathrm{N}}} \left| \Delta T \cos \psi \right| \\
&\leq C_{\mathrm{Y}} \frac{\epsilon \sigma_{\mathrm{SB}} T^3}{c \rho_{\mathrm{d}} D_{\mathrm{N}}} \left| \Delta T \right|
\end{aligned} \tag{2.13}
$$

where C_{Y} is a dimensionless parameter which is related to the object's shape, ΔT is the temperature difference between the morning and evening hemispheres, and ψ is the obliquity of the object. Thanks to the normalisation to $r_{\mathrm{h}} = 1$ AU, the relationship $(A_2)_{\mathrm{Y}} \propto D_{\mathrm{N}}^{-1}$, where $(A_2)_{\mathrm{Y}}$ is the transverse non-gravitational parameter due to the Yarkovsky effect, is then roughly satisfied. We therefore use $(A_2)_{\mathrm{Y,Bennu}}$, the transverse non-gravitational parameter due to the Yarkovsky effect of asteroid (101955) Bennu, hitherto the most reliable and strongest detection, as a reference to assess expected values for the active asteroids

$$
\left| (A_2)_{\mathrm{Y,exp}} \right| = \left| (A_2)_{\mathrm{Y,Bennu}} \right| \frac{D_{\mathrm{Bennu}}}{D_{\mathrm{N}}}, \tag{2.14}
$$

where $(A_2)_{\mathrm{Y,Bennu}} = -4.5 \times 10^{-14}$ AU day^{-2}, and $D_{\mathrm{Bennu}} = 0.49$ km is Bennu's diameter (Farnocchia et al. 2013; Nolan et al. 2013).

The semimajor-axis drift due to the Yarkovsky effect can be computed by Equation (2.10), with $g(r_{\mathrm{h}}) = r_{\mathrm{h}}^{-k_2}$, where the exact value of k_2 depends upon thermal properties of the asteroid which are, unfortunately, poorly known. However, the choice of k_2 has little effect in a typical range of $2 < k_2 < 3$ in the computation (Farnocchia et al. 2013), and thus we adopt $k_2 = 2$. Consequently, the expected drift in the semimajor axis can be simplified as

$$
\left| (\bar{\dot{a}})_{\mathrm{Y,exp}} \right| \simeq \frac{P \left| (A_2)_{\mathrm{Y,Bennu}} \right| D_{\mathrm{Bennu}}}{\pi a^2 \left(1 - e^2\right) D_{\mathrm{N}}}. \tag{2.15}
$$

If the non-gravitational effect of the active asteroid is purely due to the Yarkovsky effect, the criterion $|\bar{\dot{a}}| \lesssim \left| (\bar{\dot{a}})_{\mathrm{Y,exp}} \right|$ must be satisfied, where $\bar{\dot{a}}$ is listed in Table 2.3. By comparison, we notice that (2201) Oljato, and (3200) Phaethon are the only two[5] potential candidates whose motions might be influenced by the Yarkovsky effect, and we proceed to calculate

[5]Active asteroid (62412) 2000 SY_{178} seemingly satisfies the criterion as well, but it is disqualified by the huge uncertainty in A_2 (see Table 2.1).

Table 2.4: Transverse Non-Gravitational Parameters Due to the Yarkovsky Effect

Object	$\left\lvert (A_2)_{\mathrm{Y,exp}} \right\rvert^{\dagger}$ (AU day^{-2})	$(A_2)_{\mathrm{Y}}{}^{\ddagger}$ (AU day^{-2})	Data arc	# obs*	# opp*	RMS ($''$)
2201	1.2×10^{-14}	$(+2.89 \pm 1.28) \times 10^{-14}$	1931–2015	824 (22)	25	0.51
3200	4.4×10^{-15}	$(-1.39 \pm 1.56) \times 10^{-15}$	1983–2016	3161 (60)	30	0.46

† Value of expected transverse non-gravitational parameter due to the Yarkovsky effect estimated from the one of (101955) Bennu through Equation (2.14).

‡ Transverse non-gravitational parameter due to the Yarkovsky effect computed from orbit determination.

* Total number of observations of all types (optical and radar) used in fit. Number of discarded data bracketed.

* Number of observed oppositions.

Notes. The same technique as used for obtaining the non-gravitational parameters in Table 2.1 is applied, with the modified momentum-transfer law $g(r_{\mathrm{h}}) = r_{\mathrm{h}}^{-2}$.

their $(A_2)_{\mathrm{Y}}$, by utilising the same procedures as described in Section 2.2. The results are summarized in Table 2.4. Unfortunately, neither of the active asteroids show statistically significant detections. We therefore conclude that no Yarkovsky effect is detected amongst the active asteroids.

It is noteworthy that we failed to reproduce $(A_2)_{\mathrm{Y}}$ of (3200) Phaethon reported by Chernetenko (2010) and Galushina et al. (2015) even though observations after 2015 were discarded as a means to use a similar shorter observing arc. A possible explanation is that they might have assigned too aggressive weights to some of the observations and thus the uncertainty decreases while the nominal $(A_2)_{\mathrm{Y}}$ may increase. Instead, our finding of $(A_2)_{\mathrm{Y}}$ of (3200) Phaethon is in good match with D. Farnocchia (2016, private communication).[6]

[6]See Hanuš et al. (2018) for the detected Yarkovsky effect of the asteroid.

2.5 Summary

We examined 18 active asteroids in search of evidence for non-gravitational accelerations caused by anisotropic mass-loss, with the following results:

1. Three active asteroids (313P/Gibbs, 324P/La Sagra and (3200) Phaethon), exhibit non-gravitational accelerations with at least one component having formal signal-to-noise ratio SNR > 3. We are confident in the non-gravitational detections of 313P/Gibbs and, especially, 324P/La Sagra, both kilometer-scale objects with orbital semi-major axes near 3 AU. However, the derived non-gravitational acceleration of (3200) Phaethon, although formally significant, is influenced by systematic uncertainties of measurement, and we do not regard it as real.

2. Upper limits to the mass-loss rates implied by our non-detections of non-gravitational acceleration are less sensitive than, but broadly consistent with, rates inferred independently from physical observations. However, the rate inferred for 324P/La Sagra ($\sim$36 kg s^{-1}) is an order of magnitude larger than values based on physical observations (0.2–4 kg s^{-1}). The reason for this disagreement is not known, but may relate to the poor approximation to impulsive mass loss given by the use of the non-gravitational force law by Marsden et al. (1973).

3. The momentum-transfer law devised by Marsden et al. (1973) assumes sublimation from an isothermal surface and is logically inconsistent with the existence of non-gravitational acceleration (Appendix 2.A). Anisothermal surface temperature distributions are physically more plausible and should replace the law by Marsden et al. (1973). Except in special cases, the law proposed here (Table 2.5) will give similar results for the derived non-gravitational parameters.

4. We find no evidence for radiation pressure acceleration or the Yarkovsky effect in our sample.

Acknowledgements

We thank the anonymous referee for helpful comments and suggestions. This work used the *Find_ Orb* code by Bill Gray, for whose assistance we are extremely grateful. We are indebted to Aldo Vitagliano, Davide Farnocchia, and Quan-Zhi Ye for insightful discussions. We also thank all observers who submitted astrometric data to the Minor Planet Center, except the ones who submitted really bad astrometry and thus tortured us. This work is funded by a grant from NASA to DJ.

2.A The Marsden Momentum Transfer Law

The momentum-transfer law by Marsden et al. (1973) has been widely used to calculate non-gravitational accelerations of comets. It assumes that sublimation proceeds at a rate appropriate for a uniform, isothermal, spherical nucleus in instantaneous equilibrium with sunlight. However, an isothermal, spherical nucleus would sublimate isotropically, producing no recoil force. Therefore, the law by Marsden et al. (1973) is logically inconsistent with the presence of non-gravitational acceleration. We briefly examine the significance of this inconsistency.

As limiting cases, we compare in Figure (2.1) the model by Marsden et al. (1973) (solid black line) with three different solutions to Equation (2.4). Our approximation to isothermal sublimation (labeled $\cos\zeta = 1/4$ and shown by a red dash-dot line in the figure) essentially reproduces that by Marsden et al. (1973). Models in which sunlight heats only the day-side of the nucleus ($\cos\zeta = 1/2$, dashed green line) and in which heat is deposited only at the sub-solar point ($\cos\zeta = 1$, dotted blue line) both show substantially higher specific sublimation rates at $r_{\rm h} \gtrsim 2.5$ AU as a result of the higher average temperatures. The revised non-gravitational parameters for these models are listed in Table 2.5.

To test the effect of the differences shown in Figure (2.1), we computed new orbits of selected short-period and Halley-type comets with nonzero non-gravitational effects[7] using astrometric data from the MPC Database Search with the parameters in Table 2.5. We found that, even when using the two most extreme scenarios (namely, the isothermal ($\cos\zeta = 1/4$) and subsolar ($\cos\zeta = 1$) models), the derived orbital solutions and time-average non-gravitational accelerations are unchanged, within the uncertainties. Specifically, the RMS of best fits computed using the different momentum transfer laws of Table 2.5 are basically the same. Physically, this is because the differences between the sublimation curves in Figure (2.1) are significant only at $r_{\rm h} \gtrsim 2.5$ AU, where the momentum flux driven by water-ice sublimation is already very low. Nevertheless, our suggestion is for future work to use

[7]This was checked through the JPL Small-Body Database Search Engine. Only comets with $>10\sigma$ detections on non-gravitational effects were selected.

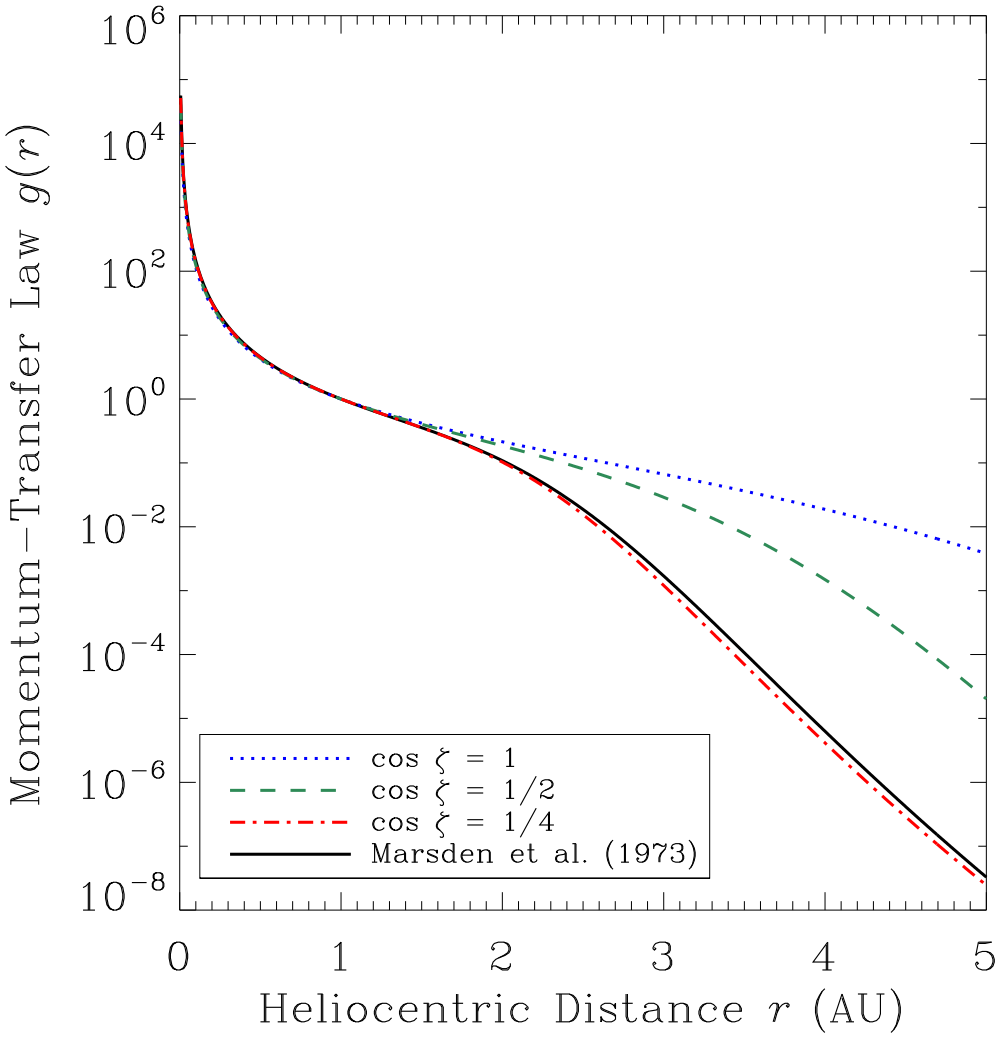

Figure 2.1: Comparison of our best fits in the formalism by Equation (2.2) for three different sublimation scenarios, i.e., $\cos\zeta = 1/4$ (isothermal sublimation), 1/2, and 1 (subsolar), and the best fit by Marsden et al. (1973). The actual normalised water-ice sublimation functions are indistinguishable from our best fits correspondingly, were they plotted in the figure, and therefore are omitted. Different fits are discriminated by line styles.

Table 2.5: Parameters in the Momentum-Transfer Law

Parameter	$\cos\zeta = 1/4$ (Isothermal)	$\cos\zeta = 1/2$ (Hemispherical)	$\cos\zeta = 1$ (Subsolar)	Unit
k_1	0.1258295	0.0337694	0.0003321	–
k_2	2.13294	2.08782	2.04680	–
k_3	5.30728	4.04051	3.06682	–
k_4	4.19724	11.4543	2752.35	–
r_0	2.67110	5.10588	50.4755	AU

Notes. Each least-squares fit was performed for heliocentric distance $r_\mathrm{h} \leq 5$ AU, beyond which the contribution from the water-ice sublimation is negligible. See Figure 2.1 for comparison.

the best-fit parameters given in Table 2.5 for $\cos\zeta = 1/2$. This case is physically the most plausible, since cometary nuclei are observed to sublimate primarily from the dayside (Keller et al. 2004), and it is also logically consistent with a net force acting on the nucleus.

Of course in reality, non-gravitational effects due to mass-loss activity are strongly dependent on, for instance, the shape, topography, spin, and thermal properties of individual nuclei, as well as the distribution of volatiles. It is impractical to devise a model which can universally satisfy all the cases of such complexity. Besides, little is known about the nuclei of the majority of comets. Therefore, adopting the aforementioned simplistic model is still appropriate and necessary for most cases.

2.B Derivation of Time-Average Values

Let us consider a continuous function of time t which is symmetric about axes of a body's elliptical orbit, denoted as $f(t)$. The elliptical orbit has semimajor axis a and eccentricity e. Now the task is to find its time-average value

$$\bar{f} = \frac{1}{P}\int_0^P f(t)\,\mathrm{d}t, \tag{2.16}$$

where P is the orbital period. Because $f(t)$ is symmetric about the axes of the ellipse, i.e., $f(P-t) = f(t)$, Equation (2.16) is therefore equivalent to

$$\bar{f} = \frac{2}{P}\int_0^{\frac{P}{2}} f(t)\,\mathrm{d}t. \tag{2.17}$$

It is often the case where f is explicitly a function of true anomaly θ, i.e., $f = f(\theta)$, and henceforth we need to find a way which connects θ and t. From orbital mechanics we know the following relationships:

$$t - t_0 = \frac{P}{2\pi}M, \tag{2.18}$$

$$M = E - \sin E, \tag{2.19}$$

$$E = \arccos\left(\frac{e+\cos\theta}{1+e\cos\theta}\right), \tag{2.20}$$

where M is the mean anomaly, and E is the eccentric anomaly. Differentiating both sides from Equation (2.18) to (2.20) yields

$$\mathrm{d}t = \frac{P}{2\pi}\mathrm{d}M, \tag{2.21}$$

$$\mathrm{d}M = (1-\cos E)\,\mathrm{d}E, \tag{2.22}$$

$$\mathrm{d}E = \frac{\sqrt{1-e^2}}{1+e\cos\theta}\mathrm{d}\theta. \tag{2.23}$$

We then apply the chain rule to Equation (2.17) and obtain

$$\begin{aligned}\bar{f} &= \frac{2}{P}\int_0^{\pi}\mathrm{d}\theta\frac{\mathrm{d}E}{\mathrm{d}\theta}\frac{\mathrm{d}M}{\mathrm{d}E}\frac{\mathrm{d}t}{\mathrm{d}M}f \\ &= \frac{(1-e^2)^{3/2}}{\pi}\int_0^{\pi}\mathrm{d}\theta\frac{f(\theta)}{(1+e\cos\theta)^2}.\end{aligned} \tag{2.24}$$

Under polar coordinates with one of the foci at the origin, which represents the Sun, and the other focus on the negative x-axis, the elliptical orbit is expressed by

$$r_{\mathrm{h}} = \frac{a\left(1-e^2\right)}{1+e\cos\theta}. \tag{2.25}$$

Combining Equations (2.24) with (2.25), we derive

$$\bar{f} = \frac{1}{\pi a^2\sqrt{1-e^2}}\int_0^{\pi} \mathrm{d}\theta f\left(\theta\right) r_{\mathrm{h}}^2. \tag{2.26}$$

In this study we need mean temperatures of the active asteroids, whose orbits are approximately elliptic, by ignoring perturbations from other bodies and non-gravitational effects. In accordance with Equation (2.4), we have $f = r_{\mathrm{h}}^{-2}$ in this scenario. Immediately, we obtain

$$\overline{\left(\frac{1}{r_{\mathrm{h}}^2}\right)} = \frac{1}{a^2\sqrt{1-e^2}}. \tag{2.27}$$

The equivalent mean heliocentric distance under this definition is thereby $\langle r_{\mathrm{h}}\rangle = a\sqrt[4]{1-e^2}$. Interestingly, the time-average heliocentric distance is $\bar{r_{\mathrm{h}}} = a\left(1+e^2/2\right)$, given by Equation (2.24) with $f = r_{\mathrm{h}}$.

REFERENCES

[1] Baer, J., Chesley, S. R., & Matson, R. D. 2011, AJ, 141, 143

[2] Bowell, E., Hapke, B., Domingue, D., et al. 1989, Asteroids II, eds. R. Binzel, T. Gehrels & M. Matthews, University of Arizona Press, Tucson, p. 524

[3] Chernetenko, Y. A. 2010, Protecting the Earth against Collisions with Asteroids and Comet Nuclei, Proceedings of the International Conference "Asteroid-Comet Hazard 2009", eds. A. M. Finkelstein, W. F. Huebner, & V. A. Shor (St. Petersburg: Nauka), p.289

[4] Chesley, S. R., Ostro, S. J., Vokrouhlický, D., et al. 2003, Science, 302, 1739

[5] Chesley, S. R., Kaluna, H., Kleyna, J., et al. 2010, Bulletin of the American Astronomical Society, 42, 950

[6] Chesley, S. R., Baer, J., & Monet, D. G. 2010, Icarus, 210, 158

[7] Chesley, S. R., Nolan, M. C., Farnocchia, D., et al. 2012, Asteroids, Comets, Meteors 2012, 1667, 6470

[8] Danby, J. M. A. 1992, Fundamentals of Celestial Mechanics (Richmond, VA, U.S.A.: Willman-Bell, Inc., 2003. 2nd ed., revised & enlarged)

[9] Farnocchia, D., Chesley, S. R., Vokrouhlický, D., et al. 2013, Icarus, 224, 1

[10] Farnocchia, D., Chesley, S. R., Chodas, P. W., et al. 2014, ApJ, 790, 114

[11] Fernández, J. A., Gallardo, T., & Brunini, A. 2002, Icarus, 159, 358

[12] Galushina, T. Y., Ryabova, G. O., & Skripnichenko, P. V. 2015, Planet. Space Sci., 118, 296

[13] Hanuš, J., Vokrouhlický, D., Delbo', M., et al. 2018, A&A, 620, L8

[14] Hsieh, H. H. 2014, Icarus, 243, 16

[15] Hsieh, H. H., & Jewitt, D. 2006, Science, 312, 561

[16] Hsieh, H. H., Yang, B., Haghighipour, N., et al. 2012, AJ, 143, 104

[17] Hsieh, H. H., & Haghighipour, N. 2016, Icarus, 277, 19

[18] Huebner, W. F., Benkhoff, J., Capria, M.-T., et al. 2006, Heat and Gas Diffusion in Comet Nuclei, by Walter F. Huebner, Johannes Benkhoff, Maria-Theresa Capria, Angioletta Coradini, Christina De Sanctis, Roberto Orosei, and Dina Prialnik. SR-004, June, 2006. ISBN 1608-280X. Published for The International Space Science Institute, Bern, Switzerland, by ESA Publications Division, Noordwijk, The Netherlands, 2006.,

[19] Hui, M.-T., & Jewitt, D. 2015, AJ, 149, 134

[20] Hui, M.-T., & Li, J. 2017, AJ, 153, 23

[21] Ishiguro, M., Hanayama, H., Hasegawa, S., et al. 2011, ApJ, 740, L11

[22] Ishiguro, M., Hanayama, H., Hasegawa, S., et al. 2011, ApJ, 741, L24

[23] Jewitt, D. 2012, AJ, 143, 66

[24] Jewitt, D., & Li, J. 2010, AJ, 140, 1519

[25] Jewitt, D., Li, J., & Agarwal, J. 2013, ApJ, 771, L36

[26] Jewitt, D., Hsieh, H., & Agarwal, J. 2015, Asteroids IV, eds. P. Michel, F. DeMeo, & W. Bottke, University of Arizona Space Science Series, 895 pp, p. 221

[27] Jewitt, D., Agarwal, J., Weaver, H., et al. 2016, AJ, 152, 77

[28] Keller, H. U., Britt, D., Buratti, B. J., & Thomas, N. 2004, Comets II, eds. M. C. Festou, H. U. Keller, & H. A. Weaver, University of Arizona Press, Tucson, 745 pp., p. 211

[29] Levison, H. F., Terrell, D., Wiegert, P. A., Dones, L., & Duncan, M. J. 2006, Icarus, 182, 161

[30] Li, J., & Jewitt, D. 2013, AJ, 145, 154

[31] Marsden, B. G., Sekanina, Z., & Yeomans, D. K. 1973, AJ, 78, 211

[32] Micheli, M., Tholen, D. J., & Elliott, G. T. 2014, ApJ, 788, L1

[33] Moreno, F., Lara, L. M., Licandro, J., et al. 2011, ApJ, 738, L16

[34] Nolan, M. C., Magri, C., Howell, E. S., et al. 2013, Icarus, 226, 629

[35] Nugent, C. R., Margot, J. L., Chesley, S. R., & Vokrouhlický, D. 2012, AJ, 144, 60

[36] Sekanina, Z., & Kracht, R. 2015, ApJ, 801, 135

[37] Tholen, D. J., Sheppard, S. S., & Trujillo, C. A. 2015, AAS/Division for Planetary Sciences Meeting Abstracts, 47, #414.03

[38] Vokrouhlický, D., Chesley, S. R., & Matson, R. D. 2008, AJ, 135, 2336

[39] Yeomans, D. K., Chodas, P. W., Sitarski, G., Szutowicz, S., & Królikowska, M. 2004, Comets II, eds. M. C. Festou, H. U. Keller, & H. A. Weaver, University of Arizona Press, Tucson, 745 pp., p.137

CHAPTER 3

Investigation on Physical Properties and Dynamics of Near-Sun Comets

Contents of this chapter have been assimilated or recompiled from the following published papers:

> Quan-Zhi Ye, Man-To Hui, Rainer Kracht, & Paul A. Wiegert (2014). *Where are the Mini Kreutz-family Comets?* The Astrophysical Journal, Volume 796, Issue 2, article id. 83, 8 pp.
>
> Man-To Hui, Quan-Zhi Ye, Matthew Knight, Karl Battams, & David Clark (2015). *Gone in a Blaze of Glory: the Demise of Comet C/2015 D1 (SOHO).* The Astrophysical Journal, Volume 813, Issue 1, article id. 73, 17 pp.

3.1 Overview

Near-Sun comets are the main members from the near-Sun family, which comprises of both comets and asteroids. These small bodies are thought to be in their end states with origin as main-belt asteroids or short-period comets, due to gravitational scattering by the major planets, or non-gravitational forces (Bailey et al. 1992; Farinella et al. 1994; Gladman et al. 1997; Greenstreet et al. 2012). The orbits are characterised with small perihelion distances ($q \lesssim q_{\mathrm{☿}} = 0.307$ AU, the perihelion distance of Mercury; Jones et al. 2018). Because they cross the orbits of the terrestrial planets, with which it is not rare to have close encounters, their dynamical lifetimes are short ($\lesssim$10 Myr; Gladman et al. 1997). Although evolution models of the solar system predict that the near-Sun objects are common (Farinella et al.

1994; Greenstreet et al. 2012), the observed number fails to satisfy the expected one, mainly because of the following two reasons:

1. It is generally challenging to conduct observations of the near-Sun objects, because their peaks in brightness usually coincide with the moments when they are near perihelion passages, which means that the solar elongation tends to be much smaller, compared to other types of small bodies in the solar system.

2. The proximity to the Sun makes the near-Sun objects more susceptible to catastrophic disintegration by thermal effects (Granvik et al. 2016).

Consequently, our knowledge about the near-Sun objects is poor. However, it is of great scientific importance to study them, particularly the cometary members. The reasons are as follows. Firstly, near-Sun comets offer great opportunity to study aging of small bodies in shorter timescales compared to other types of objects. Comets are believed to be pristine remnants since the formation of the solar system. As a comet approaches the Sun, the increasing insolation causes the temperature to rise, and intensifies sublimation of the near-surface volatile ices. Despite this activity, the skin depth, which is the distance that the thermal wave is able to propagate in the interior during a single perihelion passage, is typically only a few metres, thanks to the high porosity of the nucleus, such that pristine volatiles can still be preserved (Prialnik et al. 2004). For near-Sun comets, one will expect that the extremely high temperature in the near-Sun environments has facilitated the thermal wave to reach a greater depth after merely several perihelion returns. Therefore, near-Sun comets are likely well thermally evolved. Secondly, the susceptibility to disintegration of near-Sun comets provides us with precious chances to study the interior composition and structures of nuclei, which are otherwise black boxes. Such information is highly valuable, because it can suggest the origin and evolutionary paths of the comets, and even help constrain the evolution of the early solar system. Although cometary fragmentation events are common (a few percents per century; Chen & Jewitt 1994; Boehnhardt 2004), they are more often unseen until well after the events. The splitting tendency of the near-Sun comets let us catch sight of fragmentation events more easily, on a regular basis. Lastly, near-Sun comets are

free probes to study the corona and solar wind (Jones et al. 2018), at heliocentric distances that are infeasible for specific artificial spacecraft to reach.

Before the advent of space age, it was rare to discover and observe near-Sun comets. The first ever recognised near-Sun comet was C/1680 V1, which also bears a historical fame that its motion was used by Newton to verify Kepler's laws and his gravity theory in *Philosophiæ Naturalis Principia Mathematica* (c.f. Jones et al. 2018, and citations therein). It was not until the 19th century that a few great comets were discovered and were later recognised and classified by Kreutz as the same family members having similar sungrazing q (Kreutz 1888, 1891, 1901), which are now termed Kreutz group comets. They have a common progenitor which was perturbed into a sungrazing orbit and broke up near perihelion in the last millennia (Marsden 1967, 1989; Sekanina & Chodas 2002a, 2002b, 2004, 2007).

As the space age commenced, our understanding of the near-Sun comets began to soar. The first such advance was marked by successive discoveries of faint Kreutz comets by space-based coronagraphs *Solar Maximum Mission* (*SMM*) and *Solwind* during the period 1979–1989, which implied that this family members were substantially more populous than predicted based on the previous century of ground-based discoveries (Marsden 1989). Over the past two decades, the *Solar and Heliospheric Observatory* (*SOHO*) in a halo orbit around the Sun-Earth L_1 point has contributed a giant leap in the understanding of near-Sun comets thanks to the unprecedentedly high sensitivity and continuous monitor at the small solar elongation region of its two Large Angle and Spectrometric Coronagraph (LASCO) cameras – C2 and C3 onboard. So far *SOHO* is the most successful near-Sun comet discoverer. Not only has it discovered more than 3,000 near-Sun comets, the majority of which belong to the Kreutz family (Battams & Knight 2017; Jones et al. 2018), but also helped recognition of three sunskirting groups – Marsden, Kracht, and Meyer groups (Kracht et al. 2002; Marsden & Meyer 2002), none of which were known prior to the operation of *SOHO*. Starting from 2006, the twin *Solar Terrestrial Relationship Observatory* (*STEREO-A* and *-B*) spacecraft were launched and started operation, enabling parallactic observations of near-Sun comets, which greatly improves orbit determination. A remarkable milestone from *STEREO* observations is that near-Sun asteroid (3200) Phaethon was observed to exhibit mass-loss activity

for the very first time, and was monitored to continue behave so around perihelion, which is likely attributed to thermal fracture (Jewitt & Li 2010; Li & Jewitt 2013; Jewitt et al. 2013; Hui & Li 2017). Thereby, Phaethon is an active asteroid. However, the formation of the Geminid meteoroid stream, which is dynamically associated with (3200) Phaethon, has yet to be understood; the observed perihelion activity of the asteroid is far too small to sustain the Geminids (Jewitt & Li 2010; Li & Jewitt 2013; Hui & Li 2017).

In this chapter, we presented results from our ground-based survey for dwarf ($\lesssim$100 m across) Kreutz-group comets, and our analysis of a near-Sun comet – C/2015 D1 (*SOHO*) using ground-based and *SOHO* observations, aiming at a better understanding of physical properties of this family members.

3.2 Ground-based Survey

3.2.1 CFHT Survey

In 2012 September and October, we conducted an eight-night specific survey for Kreutz-group comets using the $\sim$1 deg^2 MegaCam attached to the 3.6-m Canada-France-Hawaii Telescope (CFHT) on Mauna Kea, Hawaii. To increase the likelihood of detection, we chose the g'-band filter, which would encompass typical cometary fluorescent emission signals such as CN, C_2 and C_3 lines, if any. Images were taken every five minutes approximately with an individual exposure time of 30 s.

Our search regions were constrained by trajectories of fictitious Kreutz-group comets that would reach perihelion between UT 2012 October 05 and December 05. Their orbital elements were randomly generated within the known range of the orbits of Kreutz-group comets discovered in 1996-2008 by *SOHO*. Although we are aware that by no means do their orbital elements follow a uniform distribution in the range, we believe that our choice is still valid, given that (1) the astrometry of the Kreutz-group comets observed by *SOHO* suffers from low resolution of its cameras, thus ambiguous orbital solutions, and (2) orbital distributions of the two subgroups of the Kreutz family are not clearly known. Any Kreutz-

Table 3.1: Details of the CFHT Survey

UT Date	R.A.	Decl.	Elongation	FWHM	Limiting $m_{g'}$
2012-09-19	[08:40, 08:48]	[$-10°$, $-7°$]	$\sim$46°	$\sim$1″.0	21.0
2012-09-20	[08:36, 08:44]	[$-10°$, $-7°$]	$\sim$48°	$\sim$1″.5	21.0
2012-09-22	[08:36, 08:44]	[$-11°$, $-8°$]	$\sim$49°	$\sim$1″.1	22.0
2012-10-16	[10:11, 10:17]	[$-20°$, $-14°$]	$\sim$47°	$\sim$2″.0	22.0
2012-10-17	[10:11, 10:17]	[$-22°$, $-16°$]	$\sim$48°	$\sim$1″.7	22.0
2012-10-18	[10:11, 10:17]	[$-22°$, $-16°$]	$\sim$49°	$\sim$1″.4	22.0
2012-10-20	[10:19, 10:25]	[$-22°$, $-16°$]	$\sim$49°	$\sim$1″.4	21.5
2012-10-21	[10:19, 10:25]	[$-23°$, $-17°$]	$\sim$50°	$\sim$1″.2	22.0

Notes. The brackets in the columns of R.A. and Decl. denote the ranges. The limiting magnitude corresponds to SNR = 1 detection of a fictitious Kreutz-group comet. Adapted from Ye et al. (2014).

group comets that were positioned within our search regions would be $\sim$1 AU from the Earth and roughly the same distance from the Sun on the inbound leg. Based on the arrival rate of the Kreutz-group comets detectable by C3 (brightness $\lesssim$8 mag) around the period of our survey, which is $\sim$10 per month (Knight et al. 2010), our coverage encompassed the most populated area of the comets whose comet-number density would be 0.04-0.08 deg^{-2}. Observing information of the CFHT survey is summarised in Table 3.1.

3.2.2 VST Survey

With basically the same strategy, we performed another specific survey for dwarf Kreutz-group comets in the morning sky in 2015 November, when the Earth was closest to their inbound leg ($\sim$0.7 AU), using the 2.6-m VLT Survey Telescope (VST) at Cerro Paranal, Chile. Images of $\sim$1 deg^2 field-of-view (FOV) were taken in Sloan-r' band by wide-field imager OmegaCAM. The individual integration time was 20 s, which was not too long before any potential Kreutz-group comets became unacceptably trailed ($\sim$3″ or $\sim$10 pixels

Table 3.2: Details of the VST Survey

UT Date	R.A.	Decl.	Airmass
2015-11-17	[10:47, 11:40]	[−40°, −38°]	[1.5, 1.9]
2015-11-18	[10:49, 11:42]	[−41°, −39°]	[1.7, 1.9]
2015-11-22	[11:05, 11:23]	[−45°, −43°]	[1.8, 1.9]
2015-11-23	[11:07, 12:10]	[−46°, −44°]	[1.9, 2.0]

Notes. Images from the first two nights were not very useful because of a mistaken observing mode, which gave only two images of different observing time covering common FOVs. The brackets in the columns denote the ranges. Seeing was particularly bad (star FWHM $\gtrsim 2''$). Limiting magnitudes corresponding to SNR = 1.5 detection varied from image to image, $m_{r'} \sim$ 19.5-20.5 for all the four nights.

in length) in the images. Summary of the search is given in Table 3.2.

3.2.3 Results

The obtained CFHT images were first calibrated with bias subtraction and flat-fielded, and then were searched by an automatic detection pipeline developed in Wiegert et al. (2007), Gilbert & Wiegert (2009, 2010), and August & Wiegert (2013) for objects having apparent motion expected for the Kreutz-group comets. We then visually verified each candidate and rejected false positives. We ended up with no detection of Kreutz-group comets in the CFHT data. The detection efficiency for each night (see Table 3.1) was determined by seeding fictitious Kreutz-group comets in the same sets of data, which were then revisited by the automatic detection routine.

Two of the Kreutz-group comets with the best quality orbit determination – *SOHO*-2388 and C/2012 U3 (*SETERO*) turned out to be within our CFHT coverage with a high level of confidence. To improve the detection limit, we coadded the CFHT images with

registration on the calculated apparent motions of the comets and background stars masked and searched for candidates with SNR > 3. However, neither was detected, suggesting their limiting apparent magnitudes as $m_{g'} = 23.7$ for C/2012 U3, and $m_{g'} = 24.0$ for *SOHO*-2388. In order to reach the brightness observed in *STEREO* images, both comets either brightened much more rapidly than expected by Knight et al. (2010), or their outburst began much earlier with a less steep brightening rate (see Ye et al. 2014 for detail).

For the VST survey, although the viewing geometry of the Kreutz-group comets within our search coverage was better than that in our CFHT survey (heliocentric distance $r_{\rm h} \approx 0.6$ AU), the obtained images were less deep than the CFHT ones, mainly because they suffered from awful seeing as well as moonlight interference. We employed the automatic detection pipeline to scan the images for objects with SNR ≥ 1.5 moving in apparent motion rates between $100''$-$1000''$ hr^{-1}, which completely covered all the possible on-sky motion rates of Kreutz-group comets within our search regions ($\sim$350$''$-600$''$ hr^{-1}). The candidates were then visually assessed. We ended up having no positive detection of any potential Kreutz-group comets.

Notably one of the brightest Kreutz-group comet *SOHO*-3069 was detected on UT 2015 December 06,[1] which peaked at $m_R = 1.8$ around UT 2015 December 08.1 on the way to perihelion. We measured the astrometry of the comet in *SOHO*/*STEREO* images and determined its orbit.[2] Given the solution, unfortunately, the comet was found to be missed by merely $\sim$3$'$-5$'$ from the edge of one of the search regions on 2015 November 17. The remaining *SOHO*-discovered Kreutz-group comets around late November to mid December were too faint.

The results from the two surveys are far from enough to constrain physical properties of the Kreutz-group comets. In the future, we plan to continue similar searches with available large telescopes equipped with wide-field CCDs.

[1] `https://sungrazer.nrl.navy.mil/index.php?p=conf_2015.txt`

[2] The measurements in C2 images were kindly provided by Karl Battams.

3.3 The Case of C/2015 D1 (*SOHO*)

Near-Sun comet C/2015 D1 (*SOHO*, hereafter 2015 D1) was discovered by W. Boonplod in *SOHO*'s LASCO images from UT 2015 February 18 (Battams & Knight 2015). It is the fourth such member in this century which was observable from the ground after C/2011 W3 (Lovejoy; Lovejoy & Williams 2011; Sekanina & Chodas 2012), C/2012 E2 (SWAN)[3], and C/2012 S1 (ISON) (Novski et al. 2012).[4] Our orbital solution (discussed in Section 3.3.2.3) to the LASCO astrometry confirms that 2015 D1 does not belong to the Kreutz family, or the Meyer, Marsden and Kracht groups (c.f. Sekanina & Chodas 2005 and citations therein). We searched for small bodies with similar orbits via the JPL Small-Body Database Search Engine, but found none. Its perihelion distance, $q = 6.06\ R_\odot$ ($1\ R_\odot = 0.00465$ AU), is substantially greater than those of the Kreutz group ($q \lesssim 2\ R_\odot$), and close to, but somewhat smaller than, the perihelion distances of the Meyer, Marsden and Kracht groups (mean value $\bar{q} \gtrsim 7.7\ R_\odot$). Knight & Walsh (2013) discriminates near-Sun comets subjected to tidal fragmentation events as sungrazing comets. Although 2015 D1 apparently disrupted, the disruption was unlikely tidally driven due to the relatively large heliocentric distance. In this manner, we address 2015 D1 as a sunskirting comet, rather than a sungrazing one.

Given the classification, 2015 D1 is a unique sunskirting comet in that it is the brightest and the first sunskirting comet which was observed from the ground over the past half century[5]. We present our photometric, morphological and orbital analysis of 2015 D1.

[3]Through private communications, we see that T. Lovejoy managed to obtain 3 astrometric positions from his images taken in strong dusk twilight on UT 2012 March 10.38, from Australia. However, his report remains largely unnoticed.

[4]We dismiss the case of C/2008 O1 (*SOHO*), which was serendipitously detected in images of a total solar eclipse, after a search based upon *SOHO* data (Pasachoff et al. 2009).

[5]Successful ground observations of the other sunskirting comet 322P/*SOHO* were made on UT 2015 May 22, later than observations of 2015 D1 (Knight et al. 2016).

3.3.1 Observations

3.3.1.1 *SOHO*

The *SOHO* spacecraft is located around the L1 point of the Sun-Earth system. The LASCO instrument onboard consists of three coronagraphs, C1, C2 and C3. Only the C2 and C3 cameras observed 2015 D1. The C2 and C3 coronagraphs, externally occulted, have annular fields of view (FOV) of 1.5–6.0 $R_\odot$ and 3.7–30 $R_\odot$, respectively (Brueckner et al. 1995). Each instrument is equipped with a filter wheel, a polarizer wheel, a shutter, and a 1024×1024 pixel CCD with a pixel scale of $11''.9$ pixel^{-1} for C2, and $56''.1$ pixel^{-1} for C3. The synoptic C2 data are taken through an orange filter with bandpass ∼5400–6400 Å, whereas the C3 observations are mainly made with a clear filter with bandpass ∼4000–8500 Å. Other filters are used much less frequently, generally once per day, and these images have half resolution (512×512). Each camera carries a polarizer wheel having polarizer positions of $-60°$, $0°$, and $+60°$, and takes polarization sequences 1–2 times per day.

2015 D1 was observed by C3 from UT 2015 February 18.0–21.8, mostly through the clear filter. The C2 camera also continuously monitored it around perihelion from UT 2015 February 19.6–19.9, all through the orange filter. Other available data include a few of C3 blue and orange filter images, and four triplets of polarized orange filter images. All the LASCO images were processed in a similar way as described in Knight et al. (2010) by use of SolarSoftWare (SSW) and SolarSoftWare DataBase (SSWDB)[6] in IDL.

The observational geometry of 2015 D1 from *SOHO* is illustrated by Figure 3.1.

3.3.1.2 Xingming Observatory

We conducted post-perihelion observations of 2015 D1 on UT 2015 March 4, 8, 9 and 15 via the 10.6-cm f/5.0 refractor attached with an Apogee U16M 4096×4096 CCD through a photometric standard V-band filter as part of the Comet Search Program (CSP) of Xingming Observatory. The images have a square FOV $4°.0 \times 4°.0$, and a pixel scale of $3''.53$ pixel^{-1}.

[6]SSW and SSWDB are both parts of the SolarSoft system, `http://www.lmsal.com/solarsoft/`.

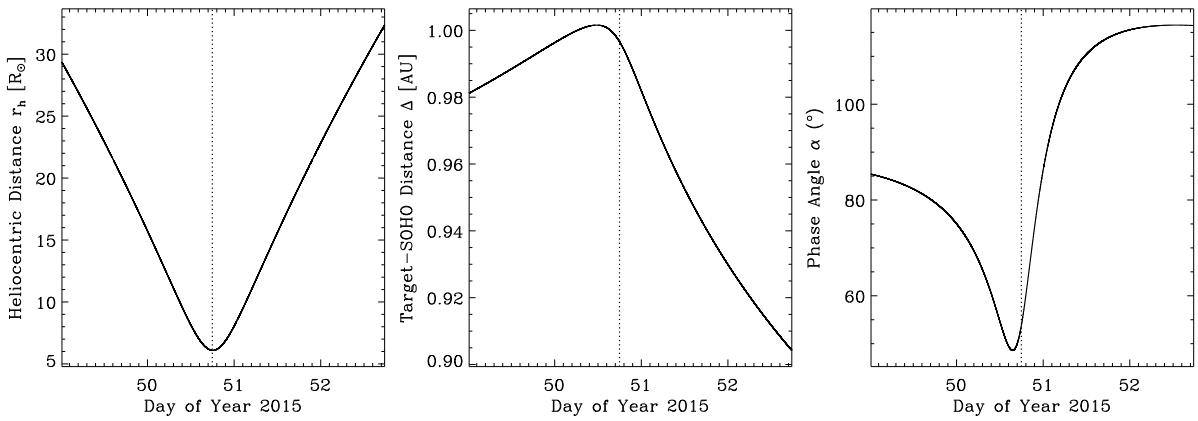

Figure 3.1: Observational geometry of 2015 D1 from *SOHO*'s perspective during its transit in *SOHO*'s FOV. The vertical dotted line in each panel marks the perihelion time $t_{\rm P}$ (TT 2015 February 19.75).

Exposures of data taken from the first two nights were 60 s and 120 s in duration, whereas data from the last two nights had exposures of 120 s only. The image quality varied from night to night, generally $\sim 9''$–$10''$ FWHM (Full Width Half Maximum). All the observation sessions were started from dusk, because of the small solar elongation. Images were first fully calibrated by subtracting bias and dark current, then were divided by flat-field frames, and finally were normalized by exposure times. The image sequence from each night was registered on field stars, and then was shifted following the motion of 2015 D1. Normalization of the sky background was then performed. Finally, the images were median co-added into a single frame. We are able to detect an enormous cigar-shaped nebulosity with its west tip within $\sim 5'$ of the predicted positions either given by JPL HORIZONS or our orbit solutions 'regardless of including non-gravitational parameters. It had a dimension of $\sim 1^\circ \times 0^\circ.2$, directed approximately east to west. The cloud appeared the most obvious on March 4, even discernible in individual frames, and the dimmest yet still sufficient for visual detection in the final stacked image from March 15.

3.3.1.3 Lowell Observatory

We attempted to recover 2015 D1 using Lowell Observatory's 4.3-m Discovery Channel Telescope (DCT) on UT 2015 March 5. We used the Large Monolithic Imager (LMI), which has a FOV $12'.3$ on a side and a 6.1K $\times$ 6.1K e2v CCD. Images were binned on chip 2×2, resulting in a pixel scale of $0''.24$ pixel^{-1}. We obtained three 30 s images using the broadband Cousins R filter. Images were trailed at the comet's rate of motion, and the pointing was determined by Lowell's ephemeris calculator from the orbital solution published by the Minor Planet Center (MPEC 2015-D73). LMI was not scheduled to be used on this night, so these were the only three images obtained. We removed the bias and applied a flat field correction using images from 2015 February 25, which was the closest night to our observations on which science data were obtained. Observing conditions were poor because this was the first night following a series of winter storms, so atmospheric seeing was significantly worse than normal. Due to the necessity of acquiring images as early as possible following twilight, the default focus values were used, so the instrumental point spread function was likely suboptimal.

On the same night we also imaged the comet's field with Lowell Observatory's 31-in (0.8-m) telescope. The 31-in has a 2K $\times$ 2K e2v CCD42-40 chip with a FOV $15'.7$ on a side and a pixel scale of $0''.46$. We obtained ten 30 s images with the Cousins R filter trailed at the comet's rate. The bias was removed and the images were flat-fielded in the standard manner.

Despite that 2015 D1 had a large 3σ position uncertainty of $\sim 4'$ during the observations, both of the FOVs are large enough to encompass the region. We visually searched both sets of images using several methods but did not find any evidence of the comet. We could detect field stars in DCT images to SDSS r magnitude of $\sim$20.0 (Ahn et al. 2012), and likely could have detected the comet to magnitude $\sim$21 despite the poor seeing since it would have been stationary while the stars were visibly trailed ($\sim 3''.5$ or $\sim$15 pixels). We could detect field stars to an SDSS r magnitude of $\sim$19.0 in the 31-in images. This is likely the limiting magnitude for any comet non-detection with the 31-in since the stars did not appear

significantly trailed due to the considerably worse seeing than on DCT.

Observation condition details from Xingming and Lowell Observatories are summarized in Table 3.3.

3.3.2 Results

3.3.2.1 Photometry

Although the ground-based observations provided much better resolution than did the LASCO C2/C3 cameras, it is impossible to perform photometric measurements with them because of the extreme fuzziness of the debris cloud of 2015 D1 as well as the tremendous area it occupied. We only conducted aperture photometry of the comet in C2/C3 images by using packages in the IDL Astronomy User's Library (Landsman 1993).

Apparent magnitudes were converted from the measured fluxes with zero-points of the LASCO images, which were calculated based upon trespassing field stars in LASCO data. Due to degradation effects of the LASCO detectors, the zero-points have changed slightly year by year. Only degradation influences upon C2 orange and C3 clear data have been examined exhaustively, as data for these filters is the most abundant. We cannot find out any detailed information about the changes in the zero-points of other filters. We adopted the temporal zero-point computed by Gardès et al. (2013) to calculate the C2 orange magnitude, and the zero-point by Lamy et al. (2013) to calculate the C3 clear magnitude. For other filters we used values given by Llebaria et al. (2006), Knight (2008) and citations therein, and further included an uncertainty of ± 0.05 mag in error estimates due to the unavailable temporal evolutions in the zero-points.

Because of the low spatial resolutions of the C2/C3 cameras, we used a fixed angular sized aperture, which allows direct comparison of our results to previous studies of near-Sun comets (Biesecker et al. 2002; Knight et al. 2010; Lamy et al. 2013). A circular aperture of radius 5 pixels ($1'.0$) was selected for full resolution 1024×1024 pixel C2 images and 3 pixels ($2'.8$) was selected for 1024×1024 pixel C3 images, to enclose the signal of 2015 D1, but at the same time to minimize contaminants from sky background as much as possible. Half

Table 3.3: Viewing Geometry of Ground Observations

Date (UT)	Tel[(1)]	$r_{\rm h}$[(2)]	Δ[(3)]	α[(4)]	ε[(5)]	θ[(6)]	$\theta_{-\odot}$[(7)]	$\theta_{-\mathbf{V}}$[(8)]	X[(9)]
2015-03-04 13:13-13:55	CSP	0.579	0.869	83.8	35.5	154.1	38.8	206.3	2.73-4.07
2015-03-05 02:20-02:26	L31	0.596	0.875	82.4	36.6	154.5	38.9	206.5	2.66-2.81
2015-03-05 02:48-02:51	DCT	0.596	0.876	82.3	36.6	154.5	38.9	206.5	3.59-3.67
2015-03-08 13:15-14:26	CSP	0.700	0.928	73.6	42.6	156.4	39.9	208.2	2.08-3.44
2015-03-09 13:37-14:41[†]	CSP	0.729	0.946	71.3	44.1	156.9	40.3	208.8	2.24-3.59
2015-03-15 13:30-15:29	CSP	0.893	1.075	59.8	51.0	159.0	43.7	212.6	1.72-3.37

(1) Telescope: CSP = Xingming Observatory's 0.11-m refractor; DCT = Lowell Observatory's 4.3-m Discovery Channel Telescope; L31 = Lowell Observatory's 31-in (0.8-m) reflector

(2) Heliocentric distance, in AU

(3) Cometocentric distance to the observatory, in AU

(4) Phase angle, in degrees

(5) Solar elongation, in degrees

(6) True anomaly, in degrees

(7) Position angle of the extended Sun-to-comet radius vector in the plane of sky, in degrees

(8) Position angle of the projected negative heliocentric velocity vector, in degrees

(9) Air mass, dimensionless

† Six images taken later than 14:24 UT were partially obstructed, hence discarded.

Notes. This table is compiled from JPL HORIZONS. We are aware that discrepancies between predicted positions increased over time. The worst case is for the CSP observation on 2015 March 15, where the JPL ephemeris differs from the one based upon EXORB by $\sim 0^\circ.8$.

resolution 512×512 pixel images had half sized apertures. The comet appeared overexposed in 14 C2 orange filtered images from UT 18:00–20:48, 2015 February 19, and hence we applied saturation corrections, developed by Knight et al. (2012). This likely still underestimates the total brightness slightly, but is much closer to the actual brightness. We estimate the uncertainties from the saturation correction at < 0.1 mag and are systematic, e.g., nearby points have nearly identical saturation correction uncertainties.

We converted apparent magnitudes m_V into heliocentric magnitudes H_V, by normalizing the distance between *SOHO* and 2015 D1 to $\Delta = 1$ AU, and correcting for the phase effect:

$$H_V\left(r_{\rm h}\right) = m_V\left(r_{\rm h}, \Delta, \alpha\right) - 5\log\Delta + 2.5\log\phi\left(\alpha\right), \tag{3.1}$$

where $r_{\rm h}$ is the heliocentric distance, α is the phase angle, and the phase function $\phi\left(\alpha\right)$ is given by Marcus (2007) as

$$\phi\left(\alpha\right) = \frac{\delta_{90}}{1+\delta_{90}}\left[k\left(\frac{1+g_{\rm f}^2}{1+g_{\rm f}^2+2g_{\rm f}\cos\alpha}\right)^{3/2} + \left(1-k\right)\left(\frac{1+g_{\rm b}^2}{1+g_{\rm b}^2+2g_{\rm b}\cos\alpha}\right)^{3/2} + \frac{1}{\delta_{90}}\right], \tag{3.2}$$

Here δ_{90} is the ratio of the dust-to-gas intensity observed at $\alpha = 90°$, with $\delta_{90} = 1$ for normal comets, $0 \leq k \leq 1$ is the partitioning coefficient between the forward- and back-scattering, and $g_{\rm f} > 0$ and $g_{\rm b} < 0$ are respectively the forward- and back-scattering asymmetry factors. Marcus (2007) suggested $k = 0.95$, $g_{\rm f} = 0.9$ and $g_{\rm b} = -0.6$ according to observations of six comets. The model has been applied widely in recent works regarding observations of near-Sun comets (e.g., Knight et al. 2010; Knight & Battams 2014). Although Li & Jewitt (2015) found slightly different parameters for C/2010 X1 (Elenin), it has minimal effects with corrections always < 0.3 mag to 2015 D1's data and does not meaningfully alter the light curve shape. Several of the comets examined by Marcus (2007) have perihelia considerably smaller than that of C/2010 X1 and thus the results are likely more comparable to 2015 D1. Therefore, we follow the suggested parameters by Marcus (2007).

We assign $\delta_{90} = 1.0$ for C3 clear filter, $\delta_{90} = 0.39$ for C2/C3 orange filters, and $\delta_{90} = 10$ for C3 blue filter, from analysis of 2015 D1's color (see Section 3.3.3.3 for details). Since the comet did not experienced strong forward- or back-scattering effects ($\alpha \sim$50–115°), its phase function is relatively flat, so the exact choice of δ_{90} always has corrections < 0.2 mag. The

general shape of 2015 D1's light curve would not have been affected by the phase function profoundly.

The resulting light curve of 2015 D1 is shown in Figure 3.2a. The comet steadily brightened from the beginning at $H_V \sim 9$, until UT 2015 February 19.4 (denoted as $\Delta t = t - t_{\rm P} \sim -8$ hrs, where t is observation epoch, and $t_{\rm P}$ is the perihelion time of the comet, UT 2015 February 19.75), when it apparently faded by ∼1 mag in ∼7 hrs, followed by a drastic surge in its brightness to $H_V \approx 1.5$ through the clear filter, in ∼5 hrs. Post-perihelion witnessed a decline in its brightness. The comet was then obstructed by the pylon of the coronagraph for 3.6 hrs. Starting from $\Delta t \sim +0.6$ day (UT 2015 February 20.3 or DOY ∼ 51.3) it dimmed smoothly on the way out of C3's FOV.

Figure 3.2b shows H_V as a function of $r_{\rm h}$. We can see that the post-perihelion brightness was consistently brighter than the pre-perihelion brightness at the same heliocentric distance, by $\gtrsim 1.5$ mag. The pre-perihelion brightening at $r_{\rm h} \gtrsim 13\ R_\odot$, $\propto r_{\rm h}^{-5.5}$, was steeper than the post-perihelion fading at the same range, $\propto r_{\rm h}^{-2.8}$. A turnover point in the inbound leg at $r_{\rm h} \sim 13\ R_\odot$ is noticed, where the brightening slowed down to $\propto r_{\rm h}^{-0.8}$. The second turnover point in the inbound leg occurred at $r_{\rm h} \sim 8\ R_\odot$, after which the comet faded despite continuing to approach the Sun. Then the flareup took place around perihelion at $r_{\rm h} \sim 6\ R_\odot$, and subsided at outbound $r_{\rm h} \approx 6.7\ R_\odot$. Similar light curves have been found amongst some of the Kreutz group comets (Knight et al. 2010). Starting from $r_{\rm h} \sim 13\ R_\odot$ in the outbound leg, the comet faded steadily toward the end of the LASCO observation. The two respectively inbound and outbound turnover points at $r_{\rm h} \sim 13\ R_\odot$ are very similar to those of Kreutz sungrazing comets, which are believed to be related to sublimation of olivines (Kimura et al. 2002).

As shown in Figure 3.3, the color of 2015 D1 was initially distinctly different from the color of the Sun, yet eventually evolved towards it, indicating that the coma became increasingly dusty. We think that this was due to depletion of sodium, which emitted strongly at the beginning of the LASCO observation, and faded out gradually. The comet had mean color indices Clear − Orange = +0.6, and Clear − Blue = −0.7 (see Section 3.3.3.3).

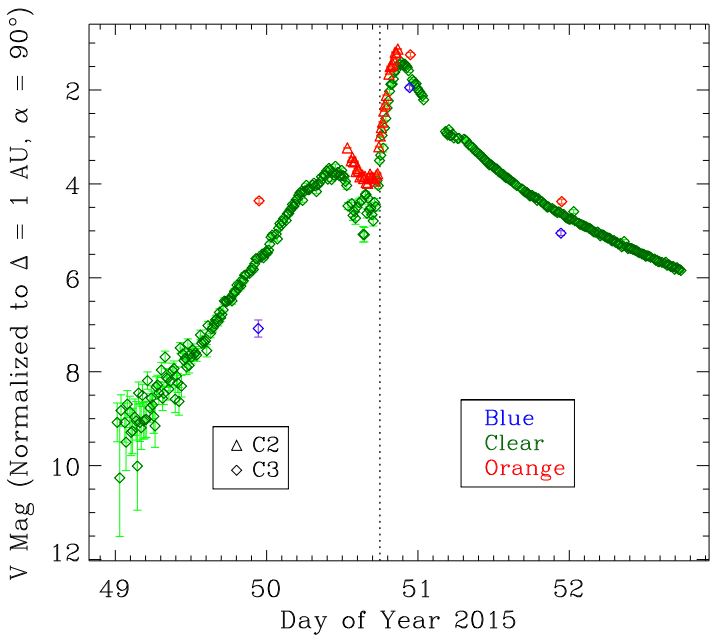

(a)

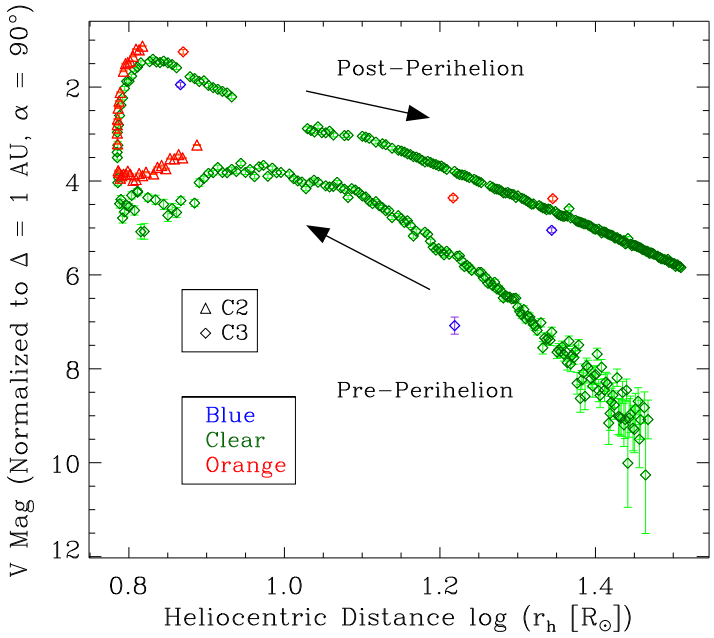

(b)

Figure 3.2: V band heliocentric magnitude of 2015 D1 observed by *SOHO*/LASCO as (a) a function of time and (b) a function of heliocentric distance. Point symbols correspond to telescopes and points are color coded according to filters, as shown in the legend. The upper panel labels perihelion by a vertical dotted line. The two arrows in the lower panel sketch the direction of the comet's evolution.

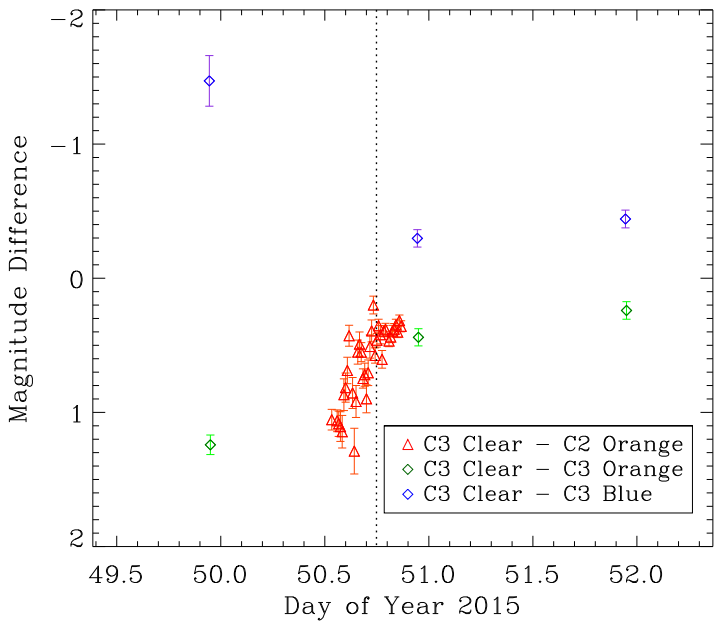

(a)

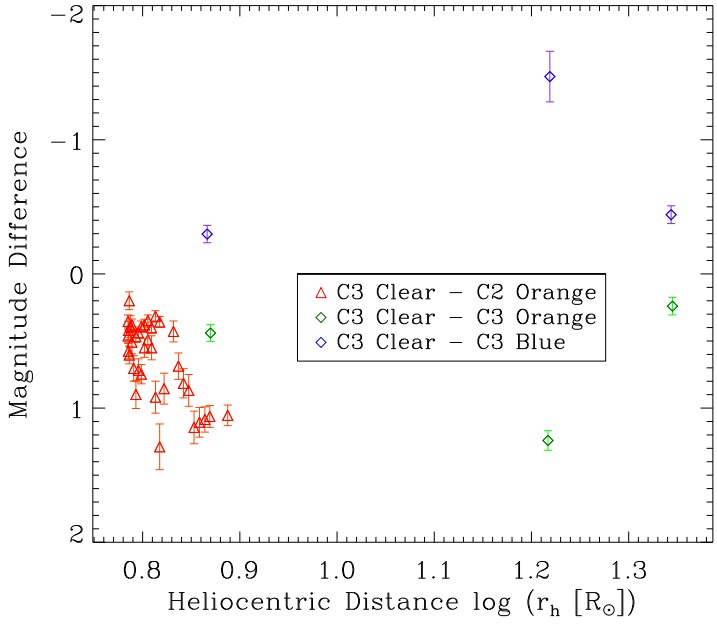

(b)

Figure 3.3: Color of 2015 D1 observed by *SOHO*/LASCO as (a) a function of time and (b) a function of heliocentric distance. The upper panel shows the perihelion moment by a vertical dotted line.

Four triplets of LASCO polarizer observations of 2015 D1 are available, however, they contain large uncertainties and the number of data points is too small, so the result will not be presented.

3.3.2.2 Morphology

Using *SOHO* and ground observations, we identified five stages in the evolution of 2015 D1:

1. From discovery to $\Delta t \sim -8$ hr (UT 2015 February 18.0–19.4): the comet, initially almost stellar, was trailed by a developing faint tail as it brightened. It was similar to comparably bright Kreutz sungrazing comets at similar heliocentric distances (see Figure 3.4a[7]).

2. From -8 hrs $\lesssim \Delta t \lesssim 0$ (UT 2015 February 19.4–19.7): the tail weakened and disappeared, whereby the comet became completely stellar (see Figure 3.4b).

3. Within $0 \lesssim \Delta t \lesssim +1$ day (UT 2015 February 19.7–20.8): the comet developed a new tail, which was much more prominent than the pre-perihelion tail, at the same time that it brightened by about $\sim$3 mag (Figure 3.2a). The optocentric region remained tight (see Figure 3.4c).

4. From $\Delta t \sim +1$ day until the departure from *SOHO*'s FOV (UT 2015 February 20.8–21.7): the comet maintained its tail, but the optocentric region appeared elongated (Figure 3.4d), reminiscent of some notable comet disintegration events such as C/1999 S4 (LINEAR; Weaver et al. 2001) and C/2012 S1 (ISON; Knight & Battams 2014).

5. A week or more after the perihelion passage: multiple ground-based observers reported a nebulous cigar-shape object near the nominal position of 2015 D1 (Mašek et al. 2015). From these images, we identified no clear central condensation or a nucleus. The object dissipated rapidly as time went by. To our knowledge, no successful observation has been reported after mid-March.

[7]Note that the time of Figure 3.4a taken is not within this stage. However, this is the best image which shows the existence of the pre-perihelion tail, although it started to weaken.

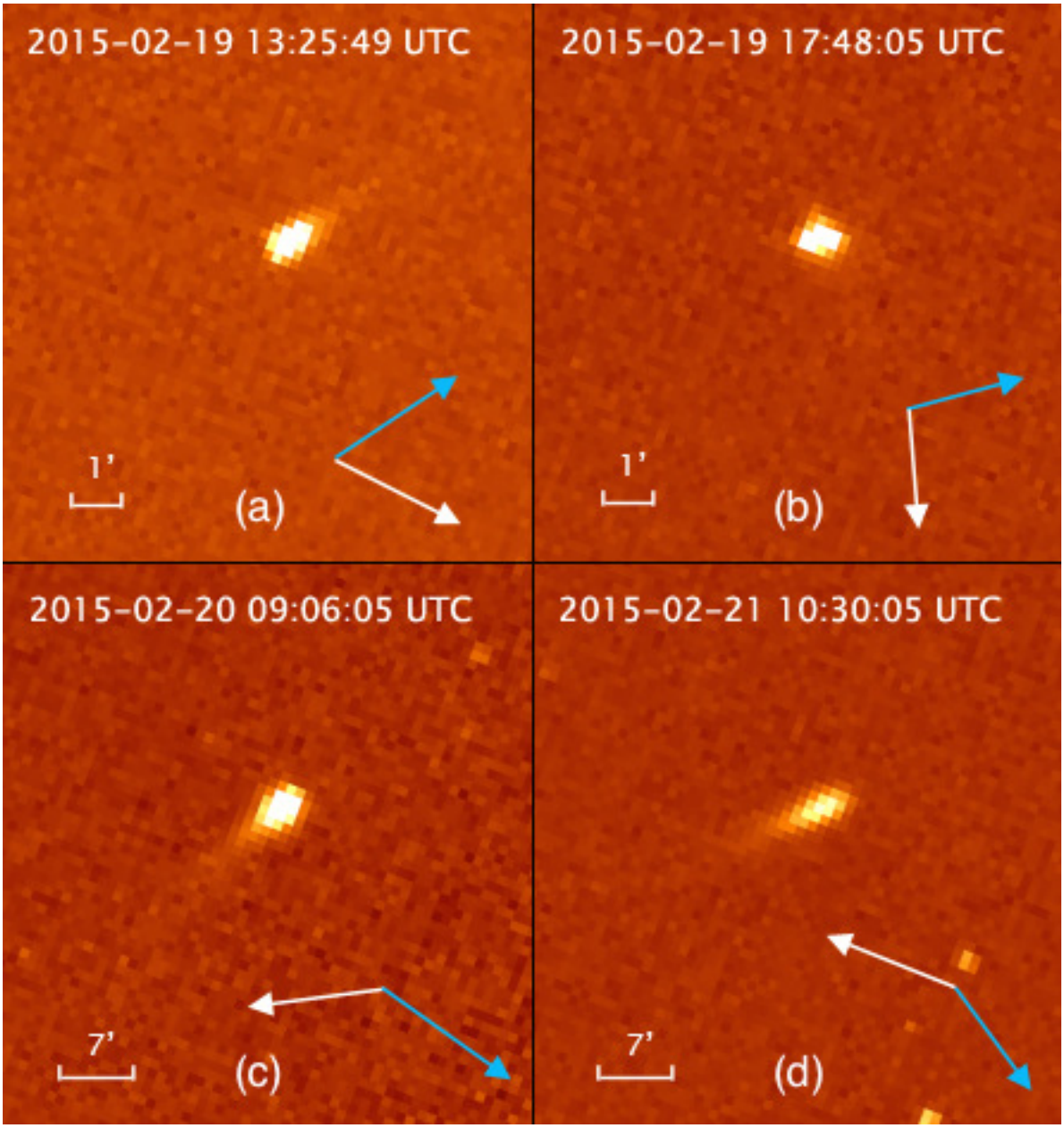

Figure 3.4: Morphological evolution of 2015 D1 observed by *SOHO*. The top two panels, (a) & (b), are LASCO C2 images and the bottom two, (c) & (d), are LASCO C3. In each panel, North is to the top and East to the left. The blue arrows point to the projected negative heliocentric velocity vector, and the white arrows point to the projected anti-solar direction.

We interpret the physical evolution of 2015 D1 as follows. During its pre-perihelion phase, the comet behaved like a typical comet, with ongoing activity producing a dust tail (Figure 3.4a). But close to perihelion, dust began to sublimate faster than it was replenished and the tail disappeared (Figure 3.4b). The rapid brightening around perihelion and the subsequent development of a new tail seemed to indicate a sudden surge in activity of the comet. Considering the signs of nucleus disintegration depicted in subsequent images, it is apparent that such dramatic change of morphology reflects a catastrophic event experienced by the nucleus. The low spatial resolutions of *SOHO* images hamper us from immediately looking into details of the disintegration, but it appears that the time from the flareup to the ultimate disruption of the nucleus took no more than 1 day (see Section 3.3.3.4). Generally speaking, the morphological evolution of 2015 D1 carries many similarities to that of Kreutz sungrazing comet C/2011 W3 (Lovejoy) (Sekanina & Chodas 2012).

3.3.2.3 Orbital Determination and Non-Gravitational Effect

We only used the *SOHO* astrometric data for orbit determination. 2015 D1 appeared too diffuse in ground-based observations, in spite of much better resolutions. Without a central condensation it is impossible to conduct astrometric measurements from these data.

SOHO astrometric measurements were recorded in custom software operated in IDL. The basic procedure was to manually select the optocenter of the comet and then allow the software to automatically calculate centroids on the 25 closest stars to the comet. This process occurred for every image in which the comet was visible. In the case of LASCO C2 there were not always 25 stars available, and thus as many as possible were recorded. LASCO C3 always has many more than 25 stars available. The limit of 25 stars has been selected as an optimum number based on computations of *SOHO*-discovered comets in the early part of the *SOHO* mission. All object locations were recorded at the sub-pixel level and passed to an implemented version of the Charon algorithm[8], which reduced the observations

[8] `http://www.projectpluto.com/charon.htm`.

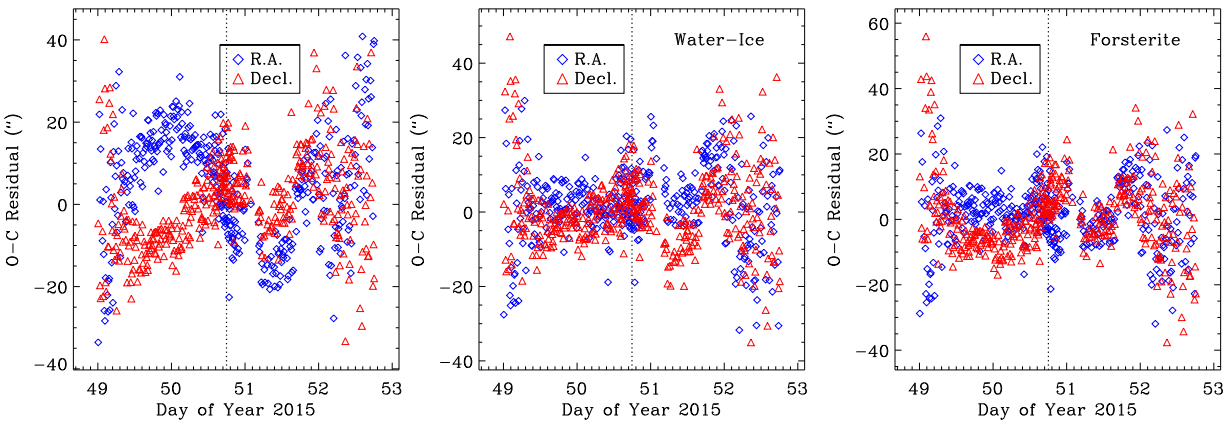

(a) (b) (c)

Figure 3.5: Plots of O−C residuals in right ascension and declination as functions of time in different orbit determinations. The left panel (a) shows residuals from the pure gravitational solution, the middle one (b) shows residuals from the non-gravitational solution based on an isothermal water-ice sublimation model, and the right one (c) are residuals from the non-gravitational solution with a forsterite sublimation model. A sinusoidal shape in the left panel is clearly seen. Although significant residuals still exist, the solution with a water-ice sublimation model overall gives the best RMS and removes the peculiar trends presented in the left panel. Each panel marks the perihelion of 2015 D1 by a vertical dotted line. Note that the three panels have different ordinate scales.

to a standard MPC format[9].

We used an orbit determination program EXORB[10] by A. Vitagliano to determine 2015 D1's orbit. Perturbations by all the eight planets, Pluto, and the three most massive asteroids, Ceres, Vesta and Pallas, are included in the computation using DE406 ephemerides, although they have basically no influence on solutions. Different weightings were assigned to the observations according to pixel scales. We filtered out 10 data points with residuals $\geq 50''$ as a cutoff. The remaining 412 observations all satisfy the residual threshold regardless of inclusion of non-gravitational effects.

[9] `http://www.minorplanetcenter.net/iau/info/ObsFormat.html`

[10] Part of the SOLEX package, available at `http://www.solexorb.it/`.

The arc covered by the *SOHO* observation was larger than any other *SOHO*-discovered comets so we treated its eccentricity e as one of the free parameters to be solved. We found that including the solving of non-gravitational parameters A_j ($j = 1, 2, 3$), which are defined in Marsden et al. (1973) from an isothermal water-ice sublimation model, significantly reduces the sinusoidal trends in astrometric residuals (the differences between the observed and calculated positions, a.k.a. O−C residuals, see Figure 3.5). The trends are irrelevant to the selection of the astrometric data, in that filtering further more different sets of measurements to stricter residual thresholds or the otherwise, or removing data points apparently close to the edge of unblocked regions where diffraction by the occulter and the pylon of LASCO might take place do not alter the trend whatsoever. Other factors including infrequent resets of SOHO's onboard spacecraft clock and potential position errors of the spacecraft have been fully ruled out. We thus conclude that the residuals are authentic.

We also found that solving the radial component A_1 alone reduces the root-mean-square (RMS) of the best fit most noticeably, from $\pm 13''.37$ to $\pm 10''.44$. We obtained $\delta A_2 > 1$ and $\delta A_3 = 0.31$, the relative errors of A_2 and A_3 respectively, significantly larger than $\delta A_1 = 0.09$. Taking into account the poor spatial resolutions of LASCO images, we solved $A_1 = (+1.209 \pm 0.118) \times 10^{-6}$ AU day^{-2} only and simply assigned $A_j = 0$ for $j \neq 1$. Similarly, JPL HORIZONS gives $A_1 = (+1.250 \pm 0.097) \times 10^{-6}$ AU day^{-2} with $A_j = 0$ for $j \neq 1$ assumed[11]. Different weightings and the number of observations filtered by JPL HORIZONS may account for the different values.

Also tested was the forsterite sublimation model by Sekanina & Kracht (2015). But we do not prefer that it was the mechanism responsible for the non-gravitational effect experienced by the comet, therefore, we did not apply it for the orbit determination (see Section 3.3.3.7 for details).

Our solutions to the orbital elements of 2015 D1 are listed in Table 3.4.

[11]Retrieved on 2015 March 24.

Table 3.4: Orbital Elements of C/2015 D1 (*SOHO*)

Reference: Heliocentric Ecliptic J2000.0

Element	Value without A_1	1σ Uncertainty	Value with A_1	1σ Uncertainty	Units
t_{P} (1)	2015 Feb 19.74859	5.3×10^{-5}	2015 Feb 19.74642	2.2×10^{-4}	TT
q (2)	0.0284511	3.1×10^{-6}	0.028219	2.3×10^{-5}	AU
e (3)	1.00099	2.1×10^{-4}	1.00142	2.1×10^{-4}	
i (4)	69.355	1.8×10^{-2}	69.582	2.9×10^{-2}	deg
Ω (5)	95.924	1.6×10^{-2}	95.897	1.7×10^{-2}	deg
ω (6)	235.194	9.4×10^{-3}	235.635	4.4×10^{-2}	deg
A_1 (7)	–	–	$+1.209 \times 10^{-6}$	1.18×10^{-7}	AU day^{-2}

(1) Time of perihelion passage in Terrestrial Time (TT)

(2) Perihelion distance

(3) Eccentricity

(4) Inclination

(5) Longitude of ascending node

(6) Argument of perihelion

(7) Water-ice sublimation model by Marsden et al. (1973). Only A_1 solved, with $A_2 = A_3 = 0$ assumed.

Notes. The RMSs of the orbital solutions without and with A_1 are $\pm 13''.37$ and $\pm 10''.44$, respectively. Both solutions have epochs on TT 2015 February 18.00483.

3.3.3 Discussion

3.3.3.1 Search for Potential Pre-discovery Data

We investigated whether serendipitous imaging of 2015 D1 may have occurred. We applied EXORB to perform multiple iterations of Monte Carlo runs, based upon the random exclusion of a stochastically varying fraction (between 30 – 70%) of the *SOHO* astrometric data, whereby 352, an arbitrary number, Monte Carlo clones of orbital elements of the comet were generated. Techniques documented in Clark (2010) were then applied to search for serendipitous pre-discovery imaging of the comet. Using the online Canadian Astronomy Data Centre Telescope Products (Gwyn et al. 2012) and the Minor Planet Center Sky Coverage Pointing Data dataset, over 600,000 archival images were considered from Canada-France-Hawaii Telescope (CFHT), Panoramic Survey Telescope and Rapid Response System (Pan-STARRS), Lincoln Near-Earth Asteroid Research (LINEAR), Spacewatch, Catalina, and Mount Lemmon, and approximately 50 smaller surveys, as well as visible and infrared images from spacecraft, including *Wide-field Infrared Survey Explorer* (*WISE*), and its asteroid-hunting portion, NEOWISE, *Hubble Space Telescope*'s Wide Field Planetary Camera 2 (WFPC2) and Wide Field Camera 3 (WFC3) catalogues. 1,000 probability clones were generated and distributed over a spatial volume consistent with observational errors. Unfortunately no recent serendipitous image of any of these clones was identified. The MPC Sky Coverage Pointing Data dataset list three images from Pan-STARRS dated 2014 April 09 and 10 encompassing the position of 2015 D1, however the comet would have been too dim to be detected at these early dates, when $r_{\rm h} \gtrsim 5$ AU.

3.3.3.2 Pre-Perihelion Dip in Light Curve

The *SOHO* observations showed a dip in the light curve starting ∼8 hrs before perihelion (Figure 3.2a). As sodium emission probably contributes significantly to the total brightness at small $r_{\rm h}$, one may question whether the dip was caused by the Swings effect (Swings 1941), i.e., temporal variation in intensity of cometary emission lines coincident with Fraunhofer lines due to Doppler shift. Assuming the entire gas emission was dominated by sodium, we

use the following equation

$$H_{V,\mathrm{gas}} = H_V + 2.5 \log \left[(1 + \delta_{90}) \, \mathfrak{G} \left(\dot{r}_{\mathrm{h}} \right) \right] , \tag{3.3}$$

where $\mathfrak{G}$ is the normalized g-factor for sodium due to the Swings effect as a function of heliocentric radial speed $\dot{r}_{\mathrm{h}}$, to examine if the dip would be largely removed. We extracted a g-factor from Figure 2 in Watanabe et al. (2003) and normalized it to large $\dot{r}_{\mathrm{h}}$. The normalized g-factor has $\mathfrak{G} = 1$ for $\dot{r}_{\mathrm{h}} \gtrsim 80$ km s^{-1} and $\mathfrak{G} = 0.05$ at perihelion.

We find that not only does Equation (3.3) fail to remove the dip in the light curve, but also artificially creates a sharp brightening spike at perihelion. Despite the scatter in the data around the bottom of the dip, the maximum dimming ∼1 hr prior to the perihelion can still be recognized. It is extremely unlikely that perihelion is off by the ∼1 hr that would be necessary to reconcile it with the Swings effect since this would be more than two orders of magnitude larger than the 1σ uncertainty in perihelion (see Table 3.4). Moreover, were it due to the Swings effect, the dip should occur much more abruptly such that a much sharper valley would be formed. More evidence which can help exclude the possibility of the Swings effect is that it would shrink the clear − orange magnitude difference centering about the dip, which was not seen whatsoever. Therefore the Swings effect is unlikely to be relevant to the formation of the dip.

Likewise, we do not feel that instrumental vignetting can account for the observed dip. Admittedly, the minimum of the dip observed by LASCO C3 took place almost exactly when the vignetting is locally highest so any inappropriate vignetting correction may cause some effects. However, the C2 vignetting is small and relatively constant during the time of the cometary light curve dip. LASCO's vignetting functions are well-established as part of the instrument's calibrations, and accordingly we see no impact on our measurements or results that may arise from this correction. We therefore reject the possibility of the LASCO vignetting as the reason for the dip; intrinsic activity of 2015 D1 is more likely to be the cause.

We notice that the onset of the dip occurred at $r_{\mathrm{h}} \sim 8\ R_{\odot}$, following a mild turnover at $r_{\mathrm{h}} \sim 13\ R_{\odot}$, consistent with the light curves of Kreutz sungrazing comets. It is thus

possibly analogous to the turnover in pre-perihelion brightness of the Kreutz sungrazing comets (Biesecker et al. 2002; Knight et al. 2010), which is believed to be correlated with the onset of sublimation of olivines (Kimura et al. 2002). The disappearance of the tail around perihelion also lends strong support to this idea.

3.3.3.3 Color

We investigate the color of 2015 D1 based upon filter magnitude differences. Clear magnitudes were determined at the time of orange/blue images by least squares interpolation between the nearest clear measurements. The clear magnitude errors were estimated from the neighboring clear magnitude errors and were combined with the orange/blue magnitude errors using standard error propagation techniques to give a total magnitude uncertainty on the color. Figure 3.3 shows magnitude differences as functions of time and heliocentric distances. The non-zero clear − blue and clear − orange magnitude differences, particularly pre-perihelion, suggest that the color of 2015 D1 was distinctly different from the color of the Sun. However, the color was generally approaching to the solar color gradually as time evolved, despite some scatter around perihelion.

We first examine whether the color can be attributed to thermal emission. We approximate dust grains as greybodies. Hence the effective temperature T_{eff} is given by

$$T_{\mathrm{eff}} = C_{\mathrm{S}} \left[(1 - A_{\mathrm{p}}) \frac{S_{\odot}}{4\epsilon\sigma_{\mathrm{SB}} r_{\mathrm{h}}^2} \right]^{\frac{1}{4}} \tag{3.4}$$

in which C_{S} is superheat, $A_{\mathrm{p}} = 0.04$ is a nominal albedo for cometary nucleii (Lamy et al. 2004), and $S_{\odot} = 1361$ W m^{-2} is the solar constant (Kopp & Lean 2011), ϵ is the effective emissivity, assumed to be unity, and $\sigma_{\mathrm{SB}} = 5.6704 \times 10^{-8}$ W m^{-2} K^{-4} is the Stefan-Boltzmann constant. The influence from thermal radiation is evaluated by

$$\frac{F_{\mathrm{th}}}{F_{\mathrm{sc}}} = \frac{r_{\mathrm{h}}^2 \int \mathfrak{T} B_{\lambda} \left(T_{\mathrm{eff}}\right) \mathrm{d}\lambda}{\int \mathfrak{T} A_{\mathrm{p}} \phi \left(\alpha\right) F_{\odot,\lambda} \mathrm{d}\lambda}, \tag{3.5}$$

where F_{th} is the thermal emission flux, F_{sc} is the flux due to scattering sunlight, $F_{\odot,\lambda}$ is the solar irradiance spectrum observed at 1 AU, B_{λ} is the thermal emission flux from Planck's law, $\mathfrak{T}$ is the effective transmissivity of a given filtered optical system, and λ is wavelength.

We calculate $\mathfrak{T}$ for C2/C3 orange, C3 clear, and C3 blue filters based upon the information provided on the LASCO calibration page[12]. The 1985 Wehrli solar spectrum[13] is used in this estimate. Unfortunately there are no available data which can constrain $C_{\rm S}$; it is a function entangled with $T_{\rm eff}$ and dust grain size (Gehrz & Ney 1992). For simplicity, we assume $C_{\rm S} \equiv 1.2$, which is approximately the average of superheat values of all types of comets listed in Gehrz & Ney (1992).

We compute $F_{\rm th}/F_{\rm sc}$ observed by LASCO blue, clear and orange filters. The simulation results are illustrated in Figure 3.6, from which we can see that influence from thermal radiation emission was very limited for all LASCO filters at $r_{\rm h} \gtrsim 10\ R_{\odot}$. Around perihelion, while C3 clear data would be affected by thermal radiation the most significantly, other filters would still receive negligible thermal radiation. However, since dust grains experience sublimation at small $r_{\rm h}$, the actual equilibrium temperature would therefore be lower than what Equation (3.4) gives (c.f. Kimura et al. 2002). Hence, we think that the effect due to thermal radiation emission can be ignored.

Intuitively, were the color of 2015 D1 due to thermal radiation entirely, it is expected that the comet would appear redder at smaller $r_{\rm h}$, which is not observed. Furthermore, as indicated in Figure 3.6, the comet should always appear the brightest in C3 clear images, mediocre in C2/C3 orange, and the faintest in C3 blue data, obviously contradictory to the LASCO observation (Figure 3.3). We can therefore conclude that thermal radiation emission is not responsible for the observed color of the comet.

We next investigate how sodium emission will influence the color of 2015 D1, since this effect is prominent when a comet nears the Sun. Similar to the method described in Knight et al. (2010), we add a synthetic rectangular sodium flux $F_{\rm Na}$ with varying intensity to the solar spectrum centered at Na D-line $\lambda = 5985$ Å with a fixed width $\Delta\lambda_{\rm Na} = 10$ Å. Since $\Delta\lambda_{\rm Na}$ is very small, $\overline{\mathfrak{T}}_{\rm Na}$, the mean effective transmission around the Na D-line within $\Delta\lambda_{\rm Na}$, can be utilized for simplification, such that the modeling magnitude difference between filter

[12] http://lasco-www.nrl.navy.mil/index.php?p=content/level_1/lascocal_index

[13] http://rredc.nrel.gov/solar/spectra/am0/wehrli1985.new.html

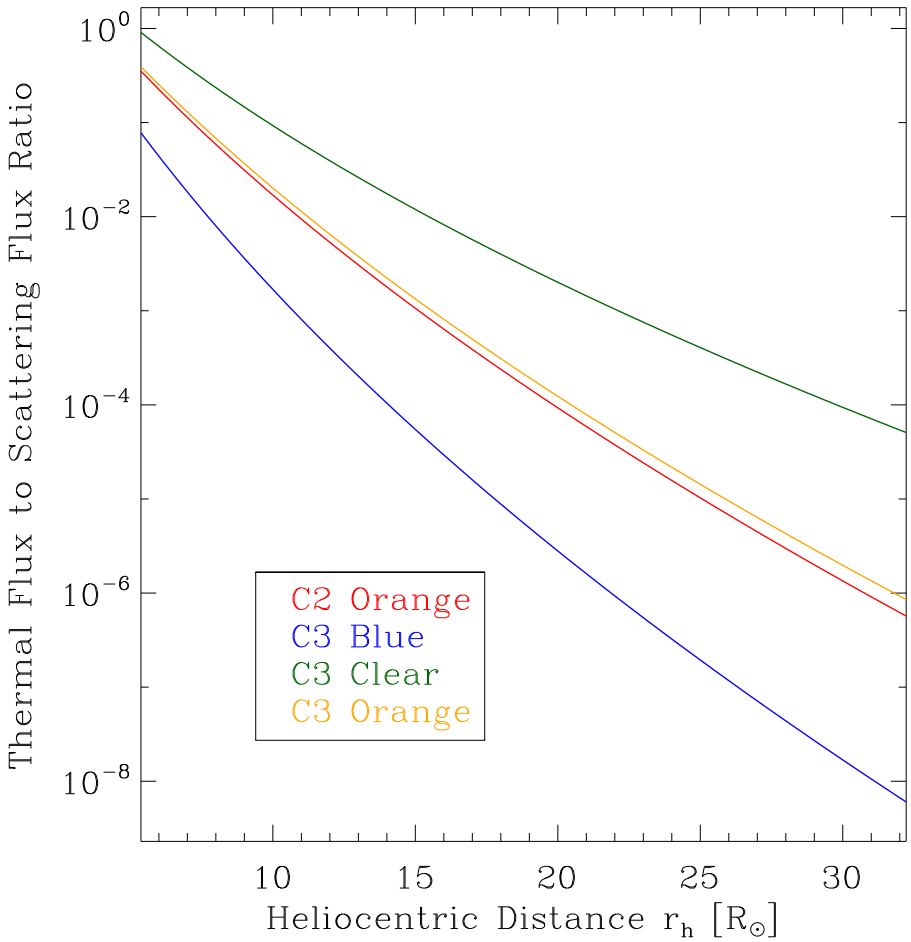

Figure 3.6: Assessment of influences from thermal radiation approached by examining the ratios of thermal emission flux to solar continuum flux $F_{\rm th}/F_{\rm sc}$ as a function of heliocentric distance $r_{\rm h}$, observed in different *SOHO*/LASCO bandpasses. The closer to the Sun, the more influential thermal radiation is.

i and j now becomes

$$\Delta m_{i,j} = -2.5 \log \left[\left(\frac{F_{\rm Na} \overline{\mathfrak{T}}_{{\rm Na},i} \Delta\lambda_{\rm Na} + \int \mathfrak{T}_i F_{\odot,\lambda} {\rm d}\lambda}{F_{\rm Na} \overline{\mathfrak{T}}_{{\rm Na},j} \Delta\lambda_{\rm Na} + \int \mathfrak{T}_j F_{\odot,\lambda} {\rm d}\lambda} \right) \left(\frac{\int \mathfrak{T}_j F_{\odot,\lambda} {\rm d}\lambda}{\int \mathfrak{T}_i F_{\odot,\lambda} {\rm d}\lambda} \right) \right], \tag{3.6}$$

whereby we obtain the results shown in Figure 3.7. Although only the flux due to the solar continuum and the flux due to the sodium emission are taken into consideration, the modeled magnitude differences can be matched by varying the intensity of the sodium emission. For instance, an intensity of sodium emission ∼100 times stronger than the solar continuum at 5985 Å corresponds to an apparent magnitude ∼0.4 mag brighter in the C2/C3 orange filters and ∼0.3 mag fainter in the C3 blue relative to the C3 clear filter, which was exactly the color of 2015 D1 around UT 2015 February 19.9 (DOY = 50.9). We thus think that the sodium emission was a plausible mechanism to account for the color of the comet observed in LASCO cameras.

The magnitude difference between the clear and orange filters decreased as the comet approached perihelion, indicating depletion of sodium emission and the coma becoming increasingly more dusty, i.e. δ_{90} increasing. Since the corrections from δ_{90} are generally comparable to the uncertainties in the magnitude data, it is not meaningful to apply a temporally varying $\delta_{90}(t)$ to correct for the phase function. Thus we take the mean magnitude differences to derive $\langle \delta_{90} \rangle$ for clear, orange and blue filters with Figure 3.7b respectively. For C3 blue filter we have $\delta_{90} = 88$, however, several typical cometary emission lines, e.g., C_2, CN, etc., would be transmittable through the bandpass and likely lower this value considerably. Thus a conservative $\delta_{90} = 10$ is used.

3.3.3.4 Ejection of Dust Grains

To understand the morphology of the comet as well as the properties of the remaining debris cloud, we employed a Monte Carlo dust model similar to the one used in Ye & Hui (2014) to generate synthetic images of the comet. During initial tests we noted the unique challenges for the case of 2015 D1. Firstly, the low spatial resolution of LASCO C3 images prevents us from obtaining information about the surface brightness profile of the cometary tail. Particularly, the pre-perihelion tail stretched ≤ 4 pixels (i.e. $\lesssim 4'$) in these images,

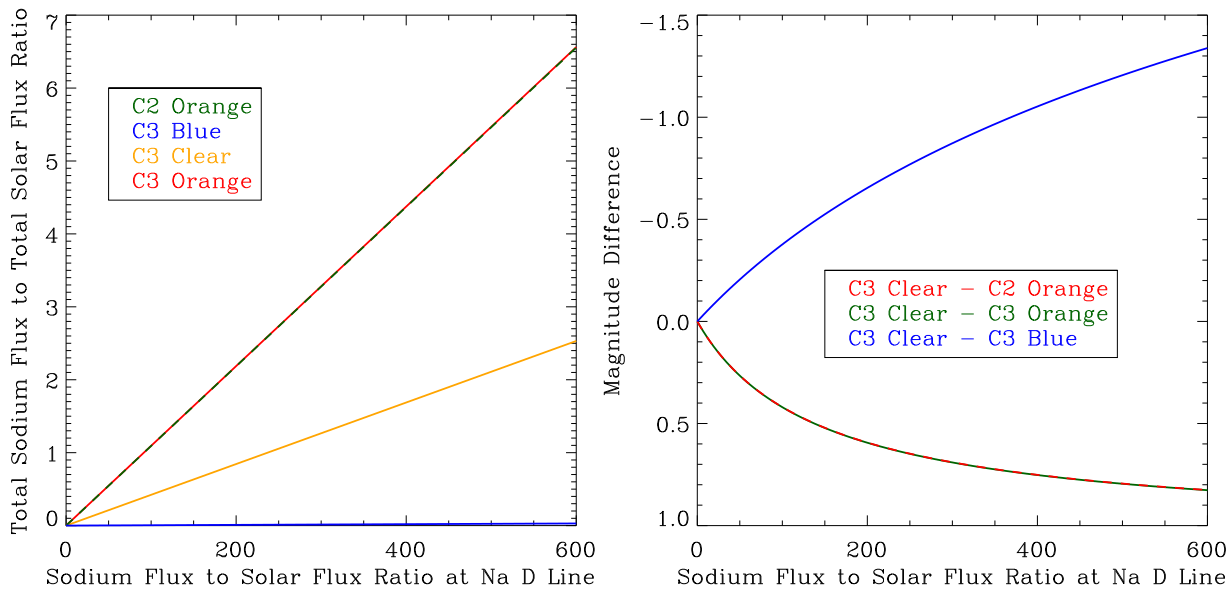

(a) (b)

Figure 3.7: Modeled influences from sodium emission observed in different *SOHO*/LASCO bandpasses. Details are discussed in Section 3.3.3.3. Note that C2 orange and C3 orange show no obvious differences and therefore overlap each other.

too small for model comparison. By the time the comet appeared in LASCO C2, the tail had begun dimming already. Secondly, for ground-based observations, the combined effect from the nebulous nature of the remnant, the lack of a central condensation as a reference point, and the large uncertainty of the comet's position ($\sim 1'$ or $\sim$100 pixels in images from Xingming) make it very difficult to directly assess the goodness of the model. Therefore, we only focus on matching the general shape of the tail/remnant starting from around perihelion. Nevertheless, thanks to the small heliocentric distances at which the dust grains were released, the often-significant divergences between different sets of parameters made it relatively easy to identify implausible solutions.

The dynamics of cometary dust grains are determined by the β parameter, the ratio between the solar radiation force and the gravitational force exerted by the Sun, and the initial ejection velocity. The ratio β, dust grain radius $\mathfrak{a}$ and bulk density of dust ρ_{d} are

related by

$$\beta = \frac{\mathcal{C}}{\rho_{\rm d}\mathfrak{a}}, \tag{3.7}$$

where $\mathcal{C} = 5.95 \times 10^{-4}$ kg m^{-2} is a proportionality constant. After trials with various parameter valuations, we found that the post-perihelion shape of the tail/remnant was predominantly controlled by the generation of small dust particles. Hence, in the following, we use the dust ejection model by Crifo & Rodionov (1997) and the upper limit of dust size $\mathfrak{a}_{\rm max} \sim 1$ cm. Assuming a typical bulk density $\rho_{\rm d} = 0.4$ g cm^{-3} (e.g., Richardson et al. 2007), we have $\beta_{\rm min} \sim 1.5 \times 10^{-4}$.

An immediate question is the duration of dust ejection: did the nucleus split instantaneously (such that the dust ejection ceased shortly after the comet's flareup), or did the disintegration process last for some period of time? We thus consider three scenarios:

1. All dust grains were impulsively ejected at the start of the flareup at $\Delta t \sim -1$ hr (impulsive ejection);

2. The dust grains were ejected from the start of the flareup to the peak brightness, i.e. $-1 \lesssim \Delta t \lesssim +3$ hrs (short semi-impulsive ejection); and

3. The dust grains were ejected from the start of the flareup to the time when signs of nucleus disintegration were seen in *SOHO* images, i.e. $-1 \lesssim \Delta t \lesssim +1$ day (long semi-impulsive ejection).

The simulated particles, isotropically released, were generated using both sets of the orbital elements in Table 3.4 during initial tests. A modified MERCURY6 package (Chambers 1999) was used to integrate all particles to observation epochs using the Bulirsch-Stoer integrator (Bulirsch 1972; Stoer 1972). Radiation forces are included in the code. Also included are gravitational perturbations from the eight major planets, although these cast no visible influence on modeling 2015 D1. We then calculated the positions of simulated particles with respect to *SOHO* or the Earth at epochs of interest to produce the shapes of the dust ensembles.

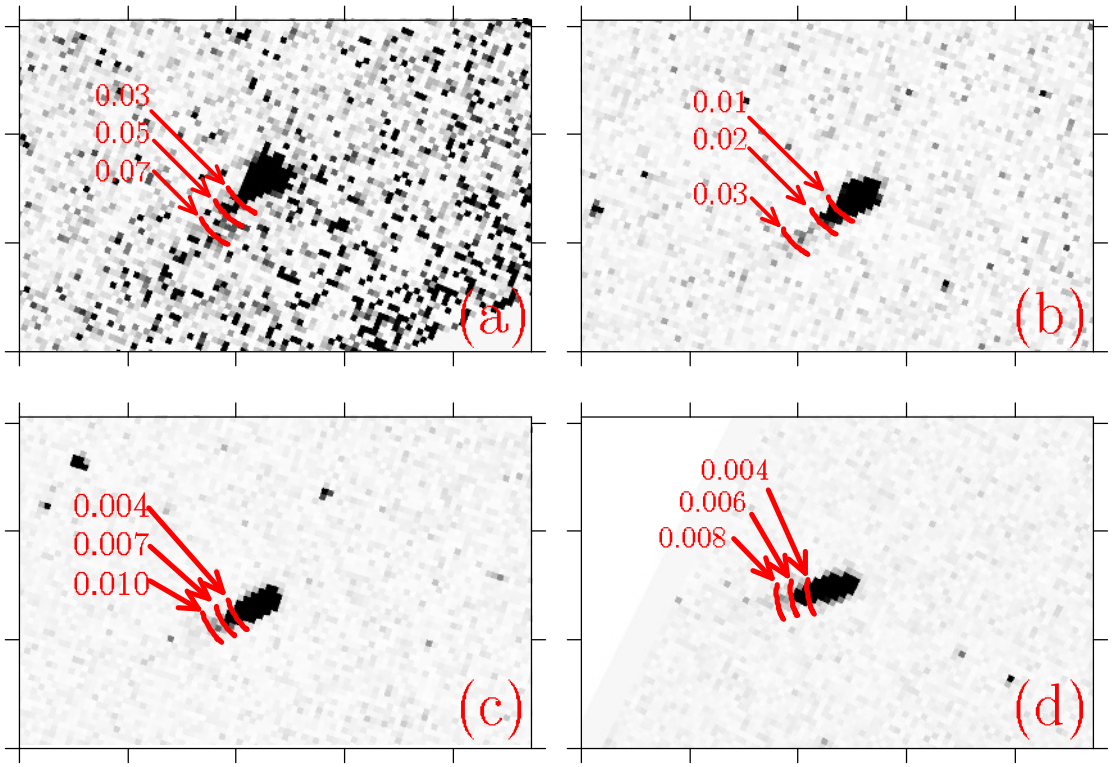

Figure 3.8: Termini of dust grains at different $\beta_{\max}$ in four selected *SOHO* images: (a) UT 2015 February 20 07:18; (b) February 20 18:06; (c) February 21 5:42; and (d) February 21 15:18. The dust models shown here were generated using the impulsive ejection model. The difference between impulsive ejection and short/long semi-impulsive ejection is not distinguishable in *SOHO* images. Ticks are plotted in the interval of $10'$, and β values are indicated on the plots. The images are oriented such that north is up and east is left.

During tests, by visual inspection, no distinction between the modeled shapes from different sets of orbital solutions was detected. We think that different orbital solutions affect little the morphological analysis, and therefore applied the solution without A_1. We tested $\beta_{\max}$ from 5×10^{-4} to 0.5 using a logarithmically varying interval (i.e., steps of 10^{-4} for $\beta_{\max} \sim 10^{-4}$, steps of 10^{-3} for $\beta_{\max} \sim 10^{-3}$, etc.). We selected eight *SOHO* images from UT 2015 February 19 20:06 to February 21 15:18, each separated by about 6 hrs (except the first two images, from UT February 19 20:06 and February 20 07:18 respectively, are separated by 11 hrs, as the comet was obstructed by the pylon of the coronagraph), and Xingming images from March 4, 8 and 15 (observations from March 9 were dismissed due to a bright background star) for model matching. For *SOHO* data, the synthetic images are essentially a set of segments due to the low resolution of *SOHO*. The goodness of the model is therefore assessed by comparing the distance traveled by different sizes of dust to the observed length of the tail (Figure 3.8). For Xingming data (Figure 3.9), the shape of the remnant seems reproducible; however, we notice that the modeled debris cloud is constantly $\sim 3'$ southeast of the actual observed cloud, a phenomenon we attribute to imperfect orbit determination. Note that this was present no matter which orbital solution (our own, JPL, MPC) was used. The positions of the simulated particles were therefore translated $\sim 3'$ in the northwest direction to align the synthetic images to the observations (Figure 3.9).

The ejection duration is constrained by Xingming data, indicating a quasi-impulsive ejection of the dust within 0.1 day (see Figure 3.9) and endorsing the idea that the destruction occurred immediately after the flareup. This is consistent with the analysis by Sekanina (2015). The *SOHO* images, suffering from low spatial resolutions, failed to allow a clear separation of different ejection durations, although the length of the tail provides a reliable constraint to the lower size limit of the optical dust. An increasing trend of $\mathfrak{a}_{\min}$ is clearly noticeable (Figure 3.10). The freshest dust grains had $\mathfrak{a}_{\min} \sim 10\ \mu$m; it increased at a rate of $\dot{\mathfrak{a}}_{\min} \sim 10^{-1}$ mm day^{-1}, and stabilized at $\sim$0.5 mm. This may be explained by observational bias: the smallest dust grains in the debris cloud quickly dispersed and thus dimmed beyond the observation threshold, and the debris cloud was expanding due to solar radiation pressure without replenishment of dust particles. Conversely, larger dust grains expanded more slowly

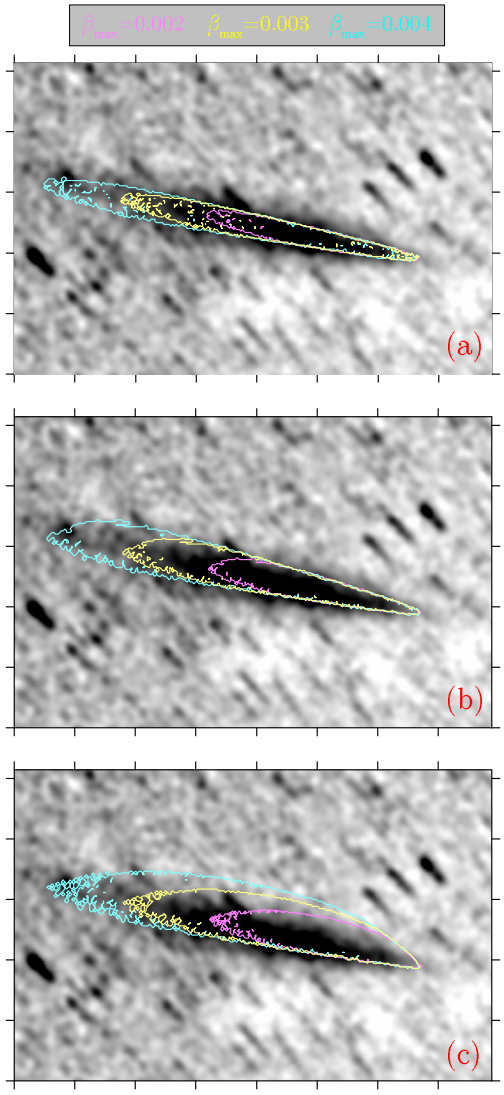

Figure 3.9: Xingming image on 2015 March 4 overlaid with the best dust models (contours) of (a) impulsive ejection ($\Delta t \sim -1$ hr); (b) short semi-impulsive ejection ($-1 \lesssim \Delta t \lesssim +3$ hrs); and (c) long semi-impulsive ejection ($-1 \lesssim \Delta t \lesssim +1$ day). The results for March 8 and 15 are largely identical. Dust models are translated $\sim 3'$ northwest to counter the offset presumably introduced by an imperfect ephemeris. The model agrees with the observation for the cases of impulsive and short semi-impulsive ejections (i.e. ejection duration < 0.1 day). Ticks are plotted in the interval of $10'$. The images are oriented so that north is up and east is left.

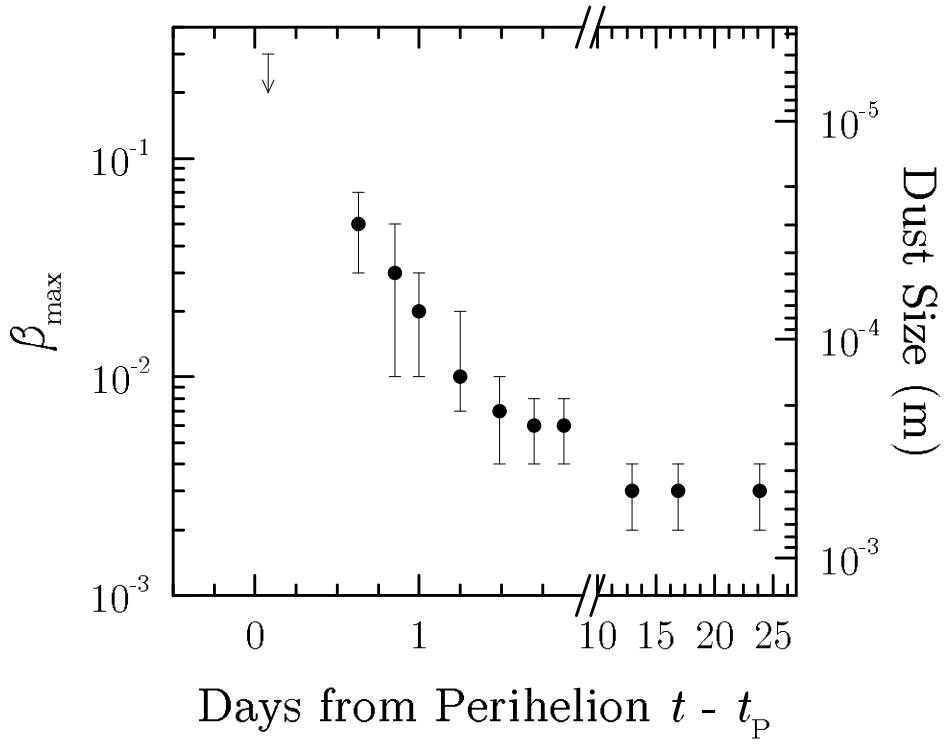

Figure 3.10: The temporal decrease of $\beta_{\max}$ as seen in *SOHO* and Xingming data.

and remained observable for a longer period of time.

3.3.3.5 Size Estimate

Nucleus Size from Photometry We can estimate the nucleus size of 2015 D1 from the *SOHO* photometric data. The heliocentric magnitude of the comet due to the dust grains which reflect sunlight can be extracted, similar to Equation (3.3), by the formula

$$H_{V,\rm dust} = H_V + 2.5 \log \left(1 + \frac{1}{\delta_{90}}\right). \tag{3.8}$$

Then the effective cross-section $C_{\rm e}$ of the comet can be calculated as

$$C_{\rm e} = \frac{\pi r_{\rm h}^2}{A_{\rm p}} 10^{-0.4\left(H_{V,\rm dust} - m_{\odot,V}\right)}. \tag{3.9}$$

Here, $m_{\odot,V} = -26.74$ is the apparent V band magnitude of the Sun. We still use $A_{\rm p} = 0.04$ for the dust grains. Figure 3.11 shows $C_{\rm e}$ as a function of time. We assume that the optically

thin coma is made of spherical dust grains whose radii range from $\mathfrak{a}_{\rm min}$ to $\mathfrak{a}_{\rm max}$, and that they obey a power-law size distribution, $\mathrm{d}N \propto a^{-\gamma}\mathrm{d}a$, with a constant γ. Then the effective nucleus radius $R_{\rm N}$ can be solved by

$$R_{\rm N} = \left[\frac{1}{\pi}\left(\frac{3-\gamma}{4-\gamma}\right)\left(\frac{\mathfrak{a}_{\rm max}^{4-\gamma} - \mathfrak{a}_{\rm min}^{4-\gamma}}{\mathfrak{a}_{\rm max}^{3-\gamma} - \mathfrak{a}_{\rm min}^{3-\gamma}}\right) C_{\rm e}\right]^{1/3}. \tag{3.10}$$

From the morphological analysis in Section 3.3.3.4 we have 10 μm $\lesssim \mathfrak{a} \lesssim$ 1 cm around perihelion. We can constrain γ from the uniform decline in $C_{\rm e}$ starting from $\Delta t \sim 0.6$ day (DOY $\sim$ 51.3) until the end of the LASCO observation by assuming that the decline was completely attributed to faster dispersions of smaller dust grains accelerated by solar radiation forces. The relationship between $C_{\rm e}$ and the dust size distribution is

$$C_{\rm e}\left(t\right) = \mathfrak{C}\left[\mathfrak{a}_{\rm min}^{3-\gamma}\left(t\right) - \mathfrak{a}_{\rm max}^{3-\gamma}\right], \tag{3.11}$$

where $\mathfrak{C}$ is an unknown constant that does not affect the calculation. We know $\mathfrak{a}_{\rm min}\left(t\right)$ in the same interval of time from Figure 3.10. A best fit to Equation (3.11) by MPFIT (Markwardt 2009) yields $\gamma = 3.16$. It is relatively insensitive to $\mathfrak{a}_{\rm max}$ and $C_{\rm e}$. For instance, changing $\mathfrak{a}_{\rm max}$ from 5 mm to $\sim$100 m varies γ from 3.10 to 3.30. We are confident that distributions with $\gamma = 3.2 \pm 0.1$ encompass the likely range of parameter uncertainties. In comparison, distributions with $3.5 \leq \gamma \leq 4.1$ have been found for a large number of comets (e.g., Sitko et al. 2011), but $\gamma = 3.2 \pm 0.1$ is not uncommon (Fulle 2004).

Around perihelion, Equation (3.10) yields $R_{\rm N} \approx 0.11 \pm 0.01$ km. Taking into account different assumptions about the albedo ($\pm$0.017; Lamy et al. 2004) yields $R_{\rm N} \approx 0.11^{+0.04}_{-0.02}$ km, which likely encompasses the original nucleus size.

Nucleus Size from Non-Gravitational Effect Whipple (1950) shows that the nucleus mass $M_{\rm N}$ can be inferred from the non-gravitational acceleration as a result of momentum conservation. The composite non-gravitational parameter, $A = \sqrt{A_1^2 + A_2^2 + A_3^2}$, is connected to the non-gravitational acceleration by $\mathcal{A}\left(r_{\rm h}\right) = Ag\left(r_{\rm h}\right)$, where $g\left(r_{\rm h}\right)$ is the dimensionless empirical non-gravitational momentum transfer law from an isothermal water-ice sublimation model (Marsden et al. 1973), which we exploited in determining A_1. However, the actual mechanism the nucleus of 2015 D1 suffered might well be too complicated

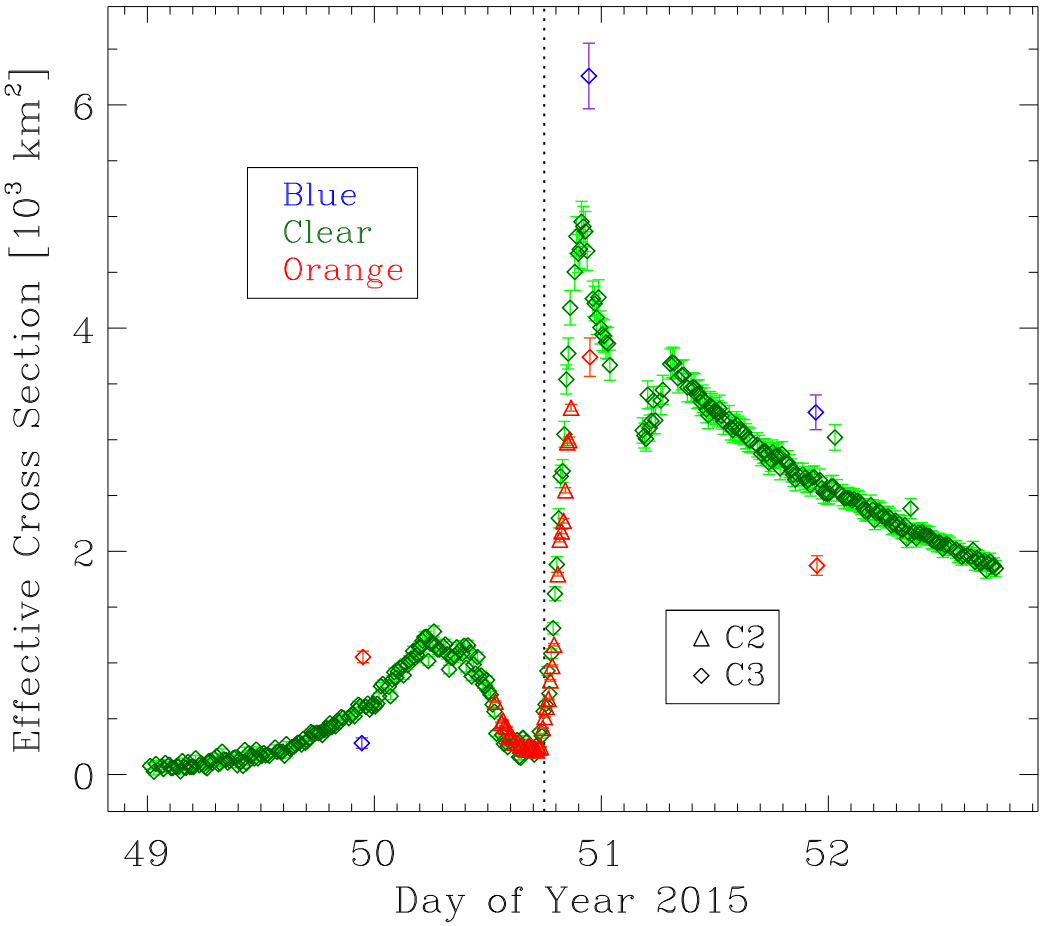

Figure 3.11: Temporal variation of effective cross-section area of 2015 D1 against time from the LASCO observation. The vertical dotted line labels the perihelion moment. Point symbols correspond to telescopes and points are color coded according to filters.

to be described by any simple models. Additionally, evidence suggests that sublimation of olivines (e.g., forsterite) has taken place around perihelion. But the contribution to the non-gravitational effect is believed to be very limited (see Section 3.3.3.7). Given the high uncertainties in the astrometric data, we still apply the empirical law $g\left(r_{\mathrm{h}}\right)$ from the water-ice sublimation model.

We thus have

$$M_{\mathrm{N}}=\kappa \frac{Q \mathscr{U} m_{\mathrm{H}} v}{\mathcal{A}}, \tag{3.12}$$

where $Q\left(r_{\mathrm{h}}\right)$ is the production rate of the dominant mass loss material, i.e. water-ice, having molecular mass $\mathscr{U}\left(\mathrm{H}_2\mathrm{O}\right)=18$, $m_{\mathrm{H}}=1.67 \times 10^{-27}$ kg is the hydrogen-atom mass, and κ is the dimensionless collimation efficiency, with $\kappa=0$ for isotropic emission and $\kappa=1$ for perfect-collimated ejection, and v is the outflow speed of gas as a function r_{h}, which is ill-defined when r_{h} is small. Applying relationships such as those given by Delsemme (1982) and Biver et al. (1997) to a near-Sun scenario is probably inappropriate. Instead, we approximate v as thermal speed

$$v_{\mathrm{th}}\left(r_{\mathrm{h}}\right)=\left[\left(\frac{3 k_{\mathrm{B}}}{\mathscr{U} m_{\mathrm{H}}}\right)^{4} \frac{\left(1-A_{\mathrm{p}}\right) S_{\odot}}{4 \epsilon \sigma_{\mathrm{SB}} r_{\mathrm{h}}^{2}}\right]^{1/8}, \tag{3.13}$$

where $k_{\mathrm{B}}=1.3806 \times 10^{-23}$ J K^{-1} is the Boltzmann constant. Assuming $A_{\mathrm{p}}=0.04$ and $\epsilon=1$, for water-ice sublimation, Equation (3.13) is simplified to $v_{\mathrm{th}}\left(r_{\mathrm{h}}\right)=0.62\ r_{\mathrm{h}}^{-0.25}$ km s^{-1}, where r_{h} is expressed in AU.

By no means can κ be constrained from the observations, and we somewhat arbitrarily adopt $\kappa=0.5$. There is no constraint on the gas production rate of 2015 D1 either, therefore the empirical law for long-period comets by Sosa & Fernández (2011) is applied. We use the magnitude only due to gas emission calculated by Equation (3.3) with $\mathfrak{G} \equiv 1$. Hence Equation (3.12) yields a mean nucleus mass $\langle M_{\mathrm{N}}\rangle \approx(5.1 \pm 3.3) \times 10^{8}$ kg, much smaller than the masses of long-period comets studied by Sosa & Fernández (2011), by four orders of magnitude. Assuming $\rho_{\mathrm{d}}=0.4$ g cm^{-3}, we have its effective nucleus radius $R_{\mathrm{N}}=\sqrt[3]{3 M_{\mathrm{N}} /\left(4 \pi \rho_{\mathrm{d}}\right)} \approx 67 \pm 15$ m.

However, in Section 3.3.3.5 the nucleus size is estimated to be $0.11_{-0.02}^{+0.04}$ km in radius. Given the same ρ_{d}, this yields $M_{\mathrm{N}} \approx(1.3\text{–}5.5) \times 10^{9}$ kg, an order of magnitude larger than

the mass derived from the non-gravitational effect. We consider the following reasons.

1. The estimated size from photometry includes all the constituents within the aperture, which occupies a spatial sphere of $\sim 1.2 \times 10^5$ km in radius around 2015 D1's optocenter around perihelion, not the nucleus alone. Larger dust grains released earlier would stay in the aperture much longer than the entire passage in LASCO C3's FOV. Therefore photometric data give a decent estimate about the initial size, whereas the size estimate from the non-gravitational effect tends to give the size around perihelion. We thus expect the size estimated from photometry to be significantly larger than the one from the non-gravitational effect.

2. The non-gravitational effect might come from a different mechanism other than from the isothermal water-ice sublimation model. As mentioned earlier, A_1 in the orbital solution fails to remove an obvious leap in the astrometric residuals in declination around perihelion (Figure 3.5). Together with the photometric data and morphological analysis, this broadly agrees that something catastrophic happened to the comet around perihelion. So one might expect that the non-gravitational acceleration emerged predominantly around perihelion, and a smooth and continuous model might have deviated from the fact.

3. The empirical law of gas production rate by Sosa & Fernández (2011) has never been examined at small $r_{\rm h}$ and therefore it may be inappropriate to apply to 2015 D1 directly. Alternatively, 2015 D1's actual production rate might deviate from the empirical law, even though it might still hold at small $r_{\rm h}$ for other near-Sun comets.

Given the substantial uncertainties associated with the behaviors of near-Sun comets, we think that both methods give acceptably consistent size estimates. We are confident that the nucleus mass of 2015 D1 was $\sim 10^8$–10^9 kg before disintegration, e.g., much smaller than most comets studied by Earth-based observers near $r_{\rm h} \sim 1$ AU. Note that we only used the clear images because they had less potential sodium contamination than the orange images, and were acquired far more frequently than the blue images.

3.3.3.6 Constraints on Post-Perihelion Remnant

Using the more restrictive Lowell non-detection from the slightly smaller DCT FOV, we can also estimate the upper limit of an inactive outbound nucleus of 2015 D1 as follows. Assuming the comet has solar color, the SDSS r magnitude converts to V magnitude by $m_r = m_V - 0.16$ (Smith et al. 2002), yielding an upper limit of $m_V < 20.16$. We then derive its effective cross-section with Equation (3.9) and use $R_\mathrm{N} = \sqrt{C_\mathrm{e}/\pi}$ to determine an upper limit to the remaining nucleus size as $R_\mathrm{N} \lesssim 0.6$ km. It is necessary to point out that we here apply the IAU H-G photometric system phase function by Bowell et al. (1989) for a bare nucleus to $\alpha = 0°$ with the slope parameter G = 0.15.

A radius of $R_\mathrm{N} \lesssim 0.6$ km is not particularly restrictive, considering that we have previously shown from both photometry and non-gravitational forces that the pre-perihelion nucleus size was $R_\mathrm{N} \lesssim 0.1$ km. Different assumptions about the albedo, the phase correction (e.g., Lagerkvist & Magnusson (1990) shows that the slope parameter can be off from G = 0.15 by $\sim\pm0.1$), or the limiting magnitude (we estimated the comet could have been $\sim$1 mag fainter than the faintest stars due to trailing), still result in $R_\mathrm{N} \lesssim 0.28$ km in the most restrictive case.

We next consider the upper limit on an active nucleus radius during post-perihelion observations. First we estimate the upper limit to water production rate Q based on our limiting magnitude following the empirical correlation found by Sosa & Fernández (2011), whereby we have $Q < 3.3\times10^{25}$ molecules s^{-1}. We next estimate the surface area necessary to produce this production rate at $r_\mathrm{h} = 0.596$ AU using the methodology of Cowan & A'Hearn (1979) and translate this into an effective radius assuming the comet is active over a surface area corresponding to the effective cross section. This yields $R_\mathrm{N} \approx 24$ m or 50 m for the subsolar or isothermal cases, respectively. Given the significant assumptions that go into this estimate, it is probable that any remaining active nucleus was less than 100 m in radius.

3.3.3.7 Mass Loss

We can investigate the mass loss of 2015 D1 from either photometry or the non-gravitational effect. Here we first examine the nucleus mass loss from photometry by transforming Equation (3.10) into

$$\dot{M}_{\mathrm{N}}(t) = \frac{4}{3}\rho_{\mathrm{d}}\left(\frac{3-\gamma}{4-\gamma}\right)\left(\frac{\mathfrak{a}_{\max}^{4-\gamma}-\mathfrak{a}_{\min}^{4-\gamma}}{\mathfrak{a}_{\max}^{3-\gamma}-\mathfrak{a}_{\min}^{3-\gamma}}\right)\dot{C}_{\mathrm{e}}(t)\,. \tag{3.14}$$

To obtain $\dot{C}_{\mathrm{e}}$, first, smoothing with 10 neighboring data points is performed to the derived C_{e} (shown in Figure 3.11). During tests we found that if too few neighboring data points are used, artifacts will be formed from the scattered data around the downhill portion of the pre-perihelion dip. On the other hand, there is no significant improvement if more neighboring data points are included. Next, we take the difference between each time step. With Equation (3.14), we then obtain a mass loss rate at each time, as shown in Figure 3.12.

While optical depth effects would delay the apparent time of mass loss, this should set a reasonable time boundary. We can see that the most rapid mass loss rate occurred around perihelion, with $\dot{M}_{\mathrm{N}} \sim 10^5$ kg s^{-1}. This is consistent with Section 3.3.3.4 that the post-perihelion tail was formed during this period in a quasi-impulsive manner. It is noteworthy that negative mass loss rates do not necessarily reflect genuine variation; they can be better explained by particles continuously drifting out of the photometric aperture or sublimating without adequate resupply from the nucleus. We obtain the total mass loss around perihelion to be $\sim 10^9$ kg, the same order of magnitude as the original nucleus mass estimated previously.

We can also investigate the mass loss according to the non-gravitational effect. Equation (3.12) can be transformed into an ordinary differential equation

$$M_{\mathrm{N}}(t) = -\kappa\frac{\dot{M}_{\mathrm{N}}(t)\,v(t)}{\mathcal{A}(t)}, \tag{3.15}$$

where $\dot{M}_{\mathrm{N}} = \mathscr{U}Qm_{\mathrm{H}}$. The variables are separable and integrable. We can then solve the ratio of mass loss to the initial nucleus mass, $\mathcal{E}_{\mathrm{M}}$, during an observation interval from t_0 to t_{obs}, by

$$\mathcal{E}_{\mathrm{M}} = 1 - \exp\left[-\frac{A}{\kappa}\int_{t_0}^{t_{\mathrm{obs}}}\frac{g(r_{\mathrm{h}}(t))}{v(r_{\mathrm{h}}(t))}\mathrm{d}t\right]. \tag{3.16}$$

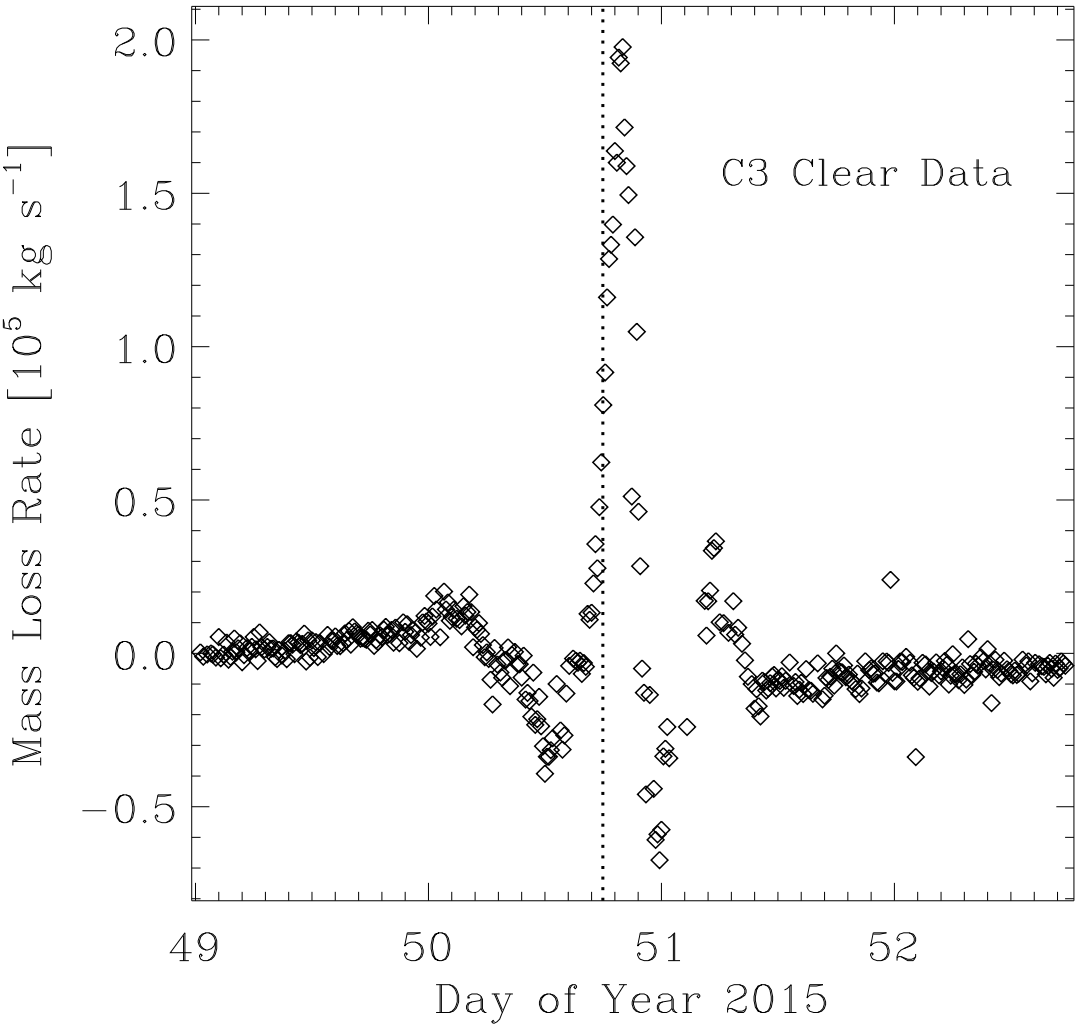

Figure 3.12: Mass loss rate calculated from photometric data. Only C3 clear data are used because of the adequate number. The perihelion moment is marked by a vertical dotted line in the middle of the graphic. Negative values in the plot should not be regarded as the authentic mass loss rate of the nucleus, but that the mass loss rate decreased due to particles drifting out of the photometric aperture.

Here we choose t_0 to be the time when the first LASCO observation of 2015 D1 was made, and t varies from the beginning to the end of LASCO observation. We find that if the empirical water-ice sublimation model is correct, 93.2% of the nucleus mass would have been lost by perihelion, and 99.6% would have been eroded by the time 2015 D1 exited LASCO C3's FOV. While we agree that mass erosion is predominantly important to 2015 D1, judging from the photometric and morphological analysis, we suspect that this overestimates the mass loss by perihelion.

We then investigate the mass loss due to sublimation of forsterite and follow the same procedures described by Sekanina & Kracht (2015) to calculate $A_{1,\mathrm{for}}$ ($A_{j,\mathrm{for}} = 0$ assumed for $j \neq 1$). The sodium model is skipped as we believe that the sodium amount is very small and therefore a significant mass loss due to sublimation of sodium is highly unlikely. During tests we found that the sodium sublimation model gives results very similar to those by water-ice sublimation.

We obtain $A_{1,\mathrm{for}} = (3.990 \pm 0.362) \times 10^{-33}$ AU day^{-2}. Comparisons between different models are shown in Figure 3.13, from which we can see that sublimation of forsterite would lead to the comet experiencing rocketing mass erosion once it reached a very small heliocentric distance of $r_\mathrm{h} \lesssim 8\ R_\odot$. By perihelion, an overwhelmingly large section of the initial mass, 89.0%, would be eroded, and the comet would devastatingly lose 99.3% of the mass by the end of the LASCO observation.

However, the forsterite model exaggerates the sinusoidal envelope of the residuals in declination pre-perihelion (Figure 3.5c) and slightly worsens the residuals, RMS = $\pm 11''.60$, in comparison to the water-ice model. Most importantly, we find that sublimation of forsterite alone fails to support the enormous mass loss experienced by 2015 D1 around perihelion. To verify this, we apply equations and parameters in Kimura et al. (2002) to estimate $\dot{M}_\mathrm{N}$ due to sublimation of forsterite around perihelion. We obtain the unit area mass loss rate as 5.7×10^{-7} kg s^{-1} m^{-2}, which is then multiplied by the surface area of the nucleus, yielding $\dot{M}_\mathrm{N} \sim 7 \times 10^{-2}$ kg s^{-1}. Although a porous nucleus would increase the surface area, resulting in a larger $\dot{M}_\mathrm{N}$, yet it is still far too small compared to the mass loss of 2015 D1 around perihelion. In comparison, given an isothermal nucleus, the mass production rate of water-ice

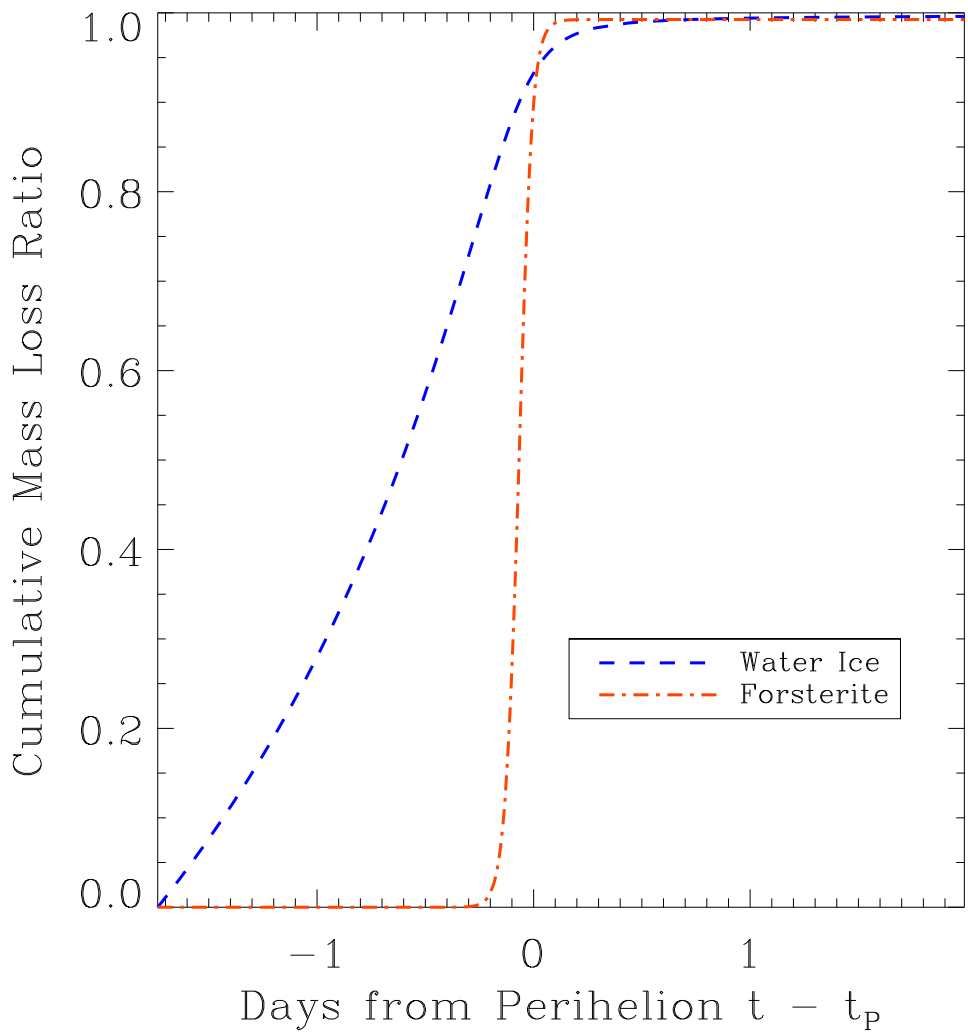

Figure 3.13: Modeled cumulative mass loss ratios from two different non-gravitational momentum transfer laws, i.e. water-ice and forsterite sublimation. The models are labeled on the plot and detailed discussions are in Section 3.3.3.7.

around perihelion is $\sim$0.2 kg s^{-1} m^{-2}. In order to support the observed peak mass loss rate, this would require a surface area of $\sim$1 km^2, equivalent to a $\sim$0.3 km radius sphere. This is order-of-magnitude consistent with our estimate of the nucleus size before disintegration. Thus, the lack of other better models makes the isothermal water-ice sublimation model the best choice for approximation.

3.3.3.8 Mechanism of the Disintegration

We briefly investigate the breakup of 2015 D1 since it is the only sunskirting comet for which there is strong observational evidence for fragmentation while it was being observed. We first consider the possibility that breakup was caused by tidal disruption due to its proximity to the Sun. For a non-spinning fluid body, the Roche radius of the Sun is $\sim$3.7 $R_\odot$ for a bulk density of $\rho_\mathrm{d} = 0.4$ g cm^{-3}, whereas 2015 D1 started to fragment at $r_\mathrm{h} \geq 6.06\ R_\odot$. A comet experiencing tidal disruption at a distance $\sim$1.6 times larger than the Roche radius seems farfetched, although we cannot fully rule out the possibility because of unknown factors such as the nucleus density and the way the nucleus spins can affect the actual Roche radius (Asphaug & Benz 1996; Richardson et al. 1998).

We next consider effects from thermal fracture. The timescale of heat conduction from the surface to the interior of a spherical rocky body is roughly $\tau_\mathrm{H} \sim R_\mathrm{N}^2/\kappa_\mathrm{eff}$ where $\kappa_\mathrm{eff} \sim 10^{-6}$ m^2 s^{-1} is the effective thermal diffusivity typical for rocks. For 2015 D1, we have $\tau_\mathrm{H} \sim 10^2$ yr.

The core temperature of 2015 D1 can be estimated from conservation of energy

$$T_\mathrm{C} = \left[\frac{(1 - A_\mathrm{p})\, S_\odot}{4\epsilon\sigma_\mathrm{SB}\,(t_\mathrm{P} - t_0)} \int_{t_0}^{t_P} \frac{\mathrm{d}t}{r_\mathrm{h}^2\,(t)} \right]^{1/4}. \tag{3.17}$$

We choose $t_\mathrm{P} - t_0 = 100$ yr, and thereby obtain $T_\mathrm{C} \approx 90$ K for the nucleus core. On the contrary around perihelion, with much of its nucleus surface devoid of volatiles assumed and sublimation of forsterite taken into account, the equilibrium surface temperature was $\sim$1640 K; a huge temperature gradient of $\Delta T \approx 1550$ K from the nucleus surface to the interior would be formed. To estimate the established thermal stress we set a nominal thermal expansion coefficient, $\alpha_\mathrm{V} \sim 10^{-5}$–$10^{-6}$ K^{-1}, typical for common rocks, and a Young's

modulus $Y \sim 10^9$–10^{11} Pa (e.g., Jewitt & Li 2010; Sekanina & Chodas 2012, and citations therein). An overwhelmingly huge thermal stress, $\sigma_{\rm th} = \alpha_{\rm V} Y \Delta T \sim 10^6$–$10^9$ Pa would be generated inside its interior, which is an order of magnitude or more larger than typical tensile strengths of cometary nuclei (c.f. Prialnik et al. 2004 and citations therein). Thermal fracture and cracking were very likely to occur, whereby preexisting subsurface volatiles were exposed, disastrously intensifying the outgassing activity.

Recently, Steckloff et al. (2015) argued that differential stress within the nucleus interior due to dynamic sublimation pressure may have been responsible for the breakup of sungrazing comet C/2012 S1 (ISON). This mechanism might be plausible for C/2012 S1 (ISON) due to the fact that its nucleus had withstood strong outgassing activity for a long period of time ($\gtrsim 1$ yr) before disintegration, however, there is no evidence that 2015 D1 was similarly active. Thus, we favor thermal fracture for 2015 D1, since sublimation stress is likely orders of magnitude smaller than the thermal stress built up within the interior.

Yet it is still unclear whether the explosion of outgassing directly crumbled the nucleus. Even if not, the fate of the nucleus was destined not to survive. Torques exerted by large mass loss from the nucleus can lead to rotational instability. Observations suggest that rotational breakup is a very common fate for comets in the solar system (e.g., Jewitt et al. 1997). Concentrating around the perihelion passage, we justify this hypothesis by

$$\Delta R_{\rm N} \approx \frac{4\pi R_{\rm N}^2}{15 \kappa_{\rm T} P_{\rm rot} v_{\rm th}}. \tag{3.18}$$

which is derived in Li & Jewitt (2015). Here $\kappa_{\rm T} \sim 10^{-4}$–$10^{-2}$ is a dimensionless coefficient of the torque (Belton et al. 2011; Drahus et al. 2011), and $P_{\rm rot}$ is the rotation period of the nucleus. We assume a rotation period $P_{\rm rot} \sim 10^5$ s, which is typical for cometary nuclei (Samarasinha et al. 2004). The thermal speed around the perihelion is $v_{\rm th} \sim 1$ km s^{-1}. By substituting other numbers we obtain $\Delta R_{\rm N} \sim 0.01$–$1$ m. Combined with Equation (3.10), we find that around perihelion, it would take the nucleus an extremely short time, $\Delta t = \Delta R_{\rm N}/\dot{R}_{\rm N} \sim 1$–$100$ s, to achieve such a change in the nucleus radius, which means that within such a short period of time, mass shedding due to outgassing would change the angular momentum by a significant factor. We hence see rotational instability as a plausible

mechanism for a final blow to the nucleus by disintegrating it, provided that it survived the outgassing explosion. This agrees with Samarasinha & Mueller (2013) that rotational disruption is likely the most common cause for splitting of sub-kilometer sized near-Sun comets. Note that rotational disruption is not significant at large heliocentric distances because the outgassing activity is limited.

3.4 Summary

We made efforts to study near-Sun comets by searching for Kreutz-group comets using ground-based observatories, as well as by investigating sunskirting comet C/2015 D1 (*SOHO*) in good detail. Key conclusions can be summarised as follows:

1. Our specific CFHT and VST Kreutz surveys in 2012 and 2015, respectively, ended up with no detections of any Kreutz-group comets. We thereby suggest that either the Kreutz-group comets brighten much more rapidly than expected by Knight et al. (2010), or their outburst occur much earlier with a moderate brightening rate.

2. 2015 D1 obviously experienced a non-gravitational effect. Solving A_1 in the orbital solution improves O−C residuals significantly and helps remove the sinusoidal trends. We find $A_1 = (1.209 \pm 0.118) \times 10^{-6}$ AU day^{-2}, based upon the isothermal water-ice sublimation model. The non-gravitational acceleration was unlikely due to forsterite sublimation as there is insufficient sublimation to drive the observed mass loss around perihelion.

3. Photometric data the non-gravitational effect consistently suggest the pre-disintegration nucleus mass of 2015 D1 as $M_{\rm N} \sim 10^8$–10^9 kg, and the nucleus size as $R_{\rm N} \sim 50$–150 m in radius, with $\rho_{\rm d} = 0.4$ g cm^{-3} assumed.

4. The mass loss of 2015 D1 was predominantly concentrated around its perihelion passage, with the most rapid loss as large as $\dot{M}_{\rm N} \sim 10^5$ kg s^{-1}. A significant portion of the mass was shed during this time interval, comparable to the original nucleus mass.

5. Morphological simulation of 2015 D1's post-perihelion tail indicates that it was formed around $\Delta t \sim -1$ hr (UT 2015 February 19.7, or DOY ~50.7) within 0.1 day, in a quasi-impulsive manner, when the comet suffered from the most rapid mass loss. The remnant of the debris cloud was morphologically dominated by smaller dust particles. The freshest dust grain sizes were $\mathfrak{a} \gtrsim 10$ μm, with $\rho_{\rm d} = 0.4$ g cm^{-3} assumed. An increasing trend in $\mathfrak{a}_{\rm min}$ was noticed, which is likely due to the smaller dust grains being dispersed more quickly without further replenishment of dust and hence dimming gradually beyond the detection threshold. We thus derive a power law index $\gamma = 3.2 \pm 0.1$ for the dust size distribution.

6. We suggest that 2015 D1's flareup in brightness was likely triggered by excess thermal stress built up within the nucleus interior causing an explosive release of material and exposing subsurface volatiles. The outgassing explosion may have crumbled the nucleus. Even if not, subsequent rotational instability of the nucleus could easily lead to its disintegration. It would only take the nucleus a very short period of time, Δt ~1–100 s, to change its angular momentum by a large factor.

7. The huge dip in the light curve starting from ~8 hrs prior to perihelion is not due to the Swings effect. Mild turnover points at $r_{\rm h} \sim 13$ $R_\odot$ and the more obvious one at $r_{\rm h} \sim 8$ $R_\odot$ suggest that sublimation of olivines is likely responsible, which is directly supported by the disappearance of the pre-perihelion tail around the same time. The subsequent rapid brightening resulted from disintegration of its nucleus, which drastically increased the effective cross-section area.

8. 2015 D1 had a color distinctly different from the color of the Sun, in particular pre-perihelion, but gradually evolved to the solar color. Sodium content and not thermal emission was the most likely the cause of the color. Depletion of sodium emission led to a final color similar to that of the Sun, which implies that the nucleus exhausted its volatiles and the coma turned dusty.

9. Ground-based observations of 2015 D1 from Xingming and Lowell revealed no detectable central condensation in the debris cloud 13–24 days after perihelion. The

post-perihelion non-detection from Lowell Observatory restricts any remaining active nucleus size to be $R_{\rm N} \lesssim 0.1$ km.

Acknowledgments

We thank Aldo Vitagliano for providing us with his modified version of EXORB and thus enabling investigation of non-gravitational effects based upon different models; David Jewitt and Jing Li for reading the manuscript and providing comments; Rainer Kracht and Gaeul Song for discussions; Kevin Schenk for providing detailed technical information of *SOHO*; and the *SOHO* operation team for making their data publicly available. We thank Xing Gao for scheduling observations and acquiring the CSP images, Teznie Pugh for obtaining the DCT images, Alberto Bolatto for providing DCT calibration images, and Ed Anderson for obtain the Lowell 31-in images. This research has made use of the VizieR catalogue access tool, CDS, Strasbourg, France, facilities of the Canadian Astronomy Data Centre operated by the National Research Council of Canada with the support of the Canadian Space Agency, SSW/SSWDB, IDL Astronomy User's Library and Bill Gray's Charon. The original description of the VizieR service was published in A&AS 143, 23. M.-T.H. was supported by a NASA grant to David Jewitt. M.M.K. was supported by NASA Planetary Astronomy grant NNX14AG81G. K.B. was supported by the NASA-funded Sungrazer Project.

REFERENCES

[1] Ahn, C. P., Alexandroff, R., Allende Prieto, C., et al. 2012, ApJS, 203, 21

[2] Asphaug, E., & Benz, W. 1996, Icarus, 121, 225

[3] August, T. M., & Wiegert, P. A. 2013, AJ, 145, 152

[4] Bailey, M. E., Chambers, J. E., & Hahn, G. 1992, A&A, 257, 315

[5] Battams, K., & Knight, M. 2015, Central Bureau Electronic Telegrams, 4067, 1

[6] Battams, K., & Knight, M. M. 2017, Philosophical Transactions of the Royal Society of London Series A, 375, 20160257

[7] Belton, M. J. S., Meech, K. J., Chesley, S., et al. 2011, Icarus, 213, 345

[8] Biesecker, D. A., Lamy, P., St. Cyr, O. C., Llebaria, A., & Howard, R. A. 2002, Icarus, 157, 323

[9] Biver, N., Bockelée-Morvan, D., Colom, P., et al. 1997, Earth Moon and Planets, 78, 5

[10] Boehnhardt, H. 2004, Comets II, 301

[11] Bowell, E., Hapke, B., Domingue, D., et al. 1989, Asteroids II, 524

[12] Brueckner, G. E., Howard, R. A., Koomen, M. J., et al. 1995, Sol. Phys., 162, 357

[13] Bulirsch, R. 1972, BAAS, 4, 418

[14] Chambers, J. E. 1999, MNRAS, 304, 793

[15] Chen, J., & Jewitt, D. 1994, Icarus, 108, 265

[16] Clark, D. L. 2010, Searching for Fireball Pre-detections in Sky Survey Images, unpublished Master's Thesis, University of Western Ontario

[17] Cowan, J. J., & A'Hearn, M. F. 1979, Moon and Planets, 21, 155

[18] Crifo, J. F., & Rodionov, A. V. 1997, Icarus, 127, 319

[19] Delsemme, A. H. 1982, IAU Colloq. 61: Comet Discoveries, Statistics, and Observational Selection, 85

[20] Drahus, M., Jewitt, D., Guilbert-Lepoutre, A., et al. 2011, ApJ, 734, L4

[21] Farinella, P., Froeschlé, C., Froeschlé, C., et al. 1994, Nature, 371, 314

[22] Fulle, M. 2004, in Comets II, ed. M. Festou, H. U. Keller, & H. A. Weaver (Tucson, AZ: Univ. Arizona Press), 565

[23] Gardès, B., Lamy, P., & Llebaria, A. 2013, Sol. Phys., 283, 667

[24] Gehrz, R. D., & Ney, E. P. 1992, Icarus, 100, 162

[25] Gilbert, A. M., & Wiegert, P. A. 2009, Icarus, 201, 714

[26] Gilbert, A. M., & Wiegert, P. A. 2010, Icarus, 210, 998

[27] Gladman, B. J., Migliorini, F., Morbidelli, A., et al. 1997, Science, 277, 197

[28] Granvik, M., Morbidelli, A., Jedicke, R., et al. 2016, Nature, 530, 303

[29] Greenstreet, S., Ngo, H., & Gladman, B. 2012, Icarus, 217, 355

[30] Grynko, Y., Jockers, K., & Schwenn, R. 2004, A&A, 427, 755

[31] Gwyn, S. D. J., Hill, N., & Kavelaars, J. J. 2012, PASP, 124, 579

[32] Hui, M.-T., & Li, J. 2017, AJ, 153, 23

[33] Jewitt, D., Li, J., & Agarwal, J. 2013, ApJ, 771, L36

[34] Jewitt, D. 1997, Earth Moon and Planets, 79, 35

[35] Jewitt, D., & Li, J. 2010, AJ, 140, 1519

[36] Jones, G. H., Knight, M. M., Battams, K., et al. 2018, Space Science Reviews, 214, #20

[37] Kimura, H., Mann, I., Biesecker, D. A., & Jessberger, E. K. 2002, Icarus, 159, 529

[38] Knight, M. M., A'Hearn, M. F., Biesecker, D. A., et al. 2010, AJ, 139, 926

[39] Knight, M. M., Kelley, M. S., Weaver, H. A., et al. 2012, AAS/Division for Planetary Sciences Meeting Abstracts, 44, #514.02

[40] Knight, M. M., Fitzsimmons, A., Kelley, M. S. P., & Snodgrass, C. 2016, ApJ, 823, L6

[41] Knight, M. M. 2008, Studies of *SOHO* Comets, Ph.D. Thesis, University of Maryland, College Park

[42] Knight, M. M., & Walsh, K. J. 2013, ApJ, 776, LL5

[43] Knight, M. M., & Battams, K. 2014, ApJ, 782, LL37

[44] Kopp, G., & Lean, J. L. 2011, Geophys. Res. Lett., 38, L01706

[45] Kracht, R., Hoenig, S., Hammer, D., & Marsden, B. G. 2002, Minor Planet Electronic Circulars, 2002-E18

[46] Kreutz, H. C. F. 1888, Kiel, Druck von C. Schaidt, C. F. Mohr nachfl., 1888.

[47] Kreutz, H. 1891, Publication der Koeniglichen Sternwarte in Kiel, 6.

[48] Kreutz, H. 1901, Astronomische Abhandlungen als Erganzungshefte zu den Astronomische Nachrichten, 1, 1

[49] Lagerkvist, C.-I., & Magnusson, P. 1990, A&A Suppl., 86, 119

[50] Lamy, P. L., Toth, I., Fernandez, Y. R., & Weaver, H. A. 2004, Comets II, 223

[51] Lamy, P., Faury, G., Llebaria, A., et al. 2013, Icarus, 226, 1350

[52] Landsman, W. B. 1993, Astronomical Data Analysis Software and Systems II, 52, 246

[53] Li, J., & Jewitt, D. 2013, AJ, 145, 154

[54] Li, J., & Jewitt, D. 2015, AJ, 149, 133

[55] Llebaria, A., Lamy, P., & Danjard, J.-F. 2006, Icarus, 182, 281

[56] Lovejoy, T., & Williams, G. V. 2011, Central Bureau Electronic Telegrams, 2930, 1

[57] Marcus, J. N. 2007, International Comet Quarterly, 29, 39

[58] Markwardt, C. B. 2009, Astronomical Data Analysis Software and Systems XVIII, 411, 251

[59] Marsden, B. G., Sekanina, Z., & Yeomans, D. K. 1973, AJ, 78, 211

[60] Marsden, B. G. 1967, AJ, 72, 1170

[61] Marsden, B. G. 1989, AJ, 98, 2306

[62] Marsden, B. G., & Meyer, M. 2002, IAU Circ., 7832, 1

[63] Mašek, M., Jurysek, J., Černý, J., et al. 2015, Central Bureau Electronic Telegrams, 4073, 1

[64] Novski, V., Novichonok, A., Burhonov, O., et al. 2012, Central Bureau Electronic Telegrams, 3238, 1

[65] Pasachoff, J. M., Rušin, V., Druckmüller, M., et al. 2009, ApJ, 702, 1297

[66] Prialnik, D., Benkhoff, J., & Podolak, M. 2004, Comets II, 359

[67] Richardson, D. C., Bottke, W. F., & Love, S. G. 1998, Icarus, 134, 47

[68] Richardson, J. E., Melosh, H. J., Lisse, C. M., & Carcich, B. 2007, Icarus, 190, 357

[69] Samarasinha, N. H., Mueller, B. E. A., Belton, M. J. S., & Jorda, L. 2004, Comets II, 281

[70] Samarasinha, N. H., & Mueller, B. E. A. 2013, ApJ, 775, L10

[71] Sekanina, Z., & Chodas, P. W. 2002, ApJ, 581, 760

[72] Sekanina, Z., & Chodas, P. W. 2002, ApJ, 581, 1389

[73] Sekanina, Z., & Chodas, P. W. 2004, ApJ, 607, 620

[74] Sekanina, Z., & Chodas, P. W. 2005, ApJS, 161, 551

[75] Sekanina, Z., & Chodas, P. W. 2007, ApJ, 663, 657

[76] Sekanina, Z., & Chodas, P. W. 2012, ApJ, 757, 127

[77] Sekanina, Z. 2015, Central Bureau Electronic Telegrams, 4074, 1

[78] Sekanina, Z., & Kracht, R. 2015, ApJ, 801, 135

[79] Sitko, M. L., Lisse, C. M., Kelley, M. S., et al. 2011, AJ, 142, 80

[80] Smith, J. A., Tucker, D. L., Kent, S., et al. 2002, AJ, 123, 2121

[81] Sosa, A., & Fernández, J. A. 2011, MNRAS, 416, 767

[82] Steckloff, J. K., Johnson, B. C., Bowling, T., et al. 2015, Icarus, 258, 430

[83] Stoer, J. 1972, BAAS, 4, 422

[84] Swings, P. 1941, Lick Observatory Bulletin, 19, 131

[85] Watanabe, J.-i., Kawakita, H., Furusho, R., & Fujii, M. 2003, ApJ, 585, L159

[86] Weaver, H. A., Sekanina, Z., Toth, I., et al. 2001, Science, 292, 1329

[87] Wiegert, P., Balam, D., Moss, A., et al. 2007, AJ, 133, 1609

[88] Whipple, F. L. 1950, ApJ, 111, 375

[89] Ye, Q.-Z., Hui, M.-T., Kracht, R., & Wiegert, P. A. 2014, ApJ, 796, 83

[90] Ye, Q.-Z., & Hui, M.-T. 2014, ApJ, 787, 115

CHAPTER 4

Sizing Up Comets by a Nucleus-Extraction Technique

This chapter has been reformatted from the following submitted paper:

> Man-To Hui & Jian-Yang Li (2018). *Is the Cometary Nucleus Extraction Technique Reliable?* Publications of the Astronomical Society of the Pacific, 130, 104501.

4.1 Overview

Comets are conceived to be amongst the most primitive objects in the solar system as they are generally less thermally evolved. They offer opportunities of scientific importance to help understand the formation and early history of the solar system. One of the aspects we ought to know is the size distribution of the cometary nuclei because it gives insight to their evolution. The size distribution is usually described by a simple power law as

$$\mathrm{d}N \propto R_{\mathrm{N}}^{-\Gamma}\mathrm{d}R_{\mathrm{N}}, \tag{4.1}$$

where R_{N} is the radius of a cometary nucleus, Γ is the slope index, which is usually assumed to be a constant, and $\mathrm{d}N$ is the number of cometary nuclei having radii ranging from R_{N} to $R_{\mathrm{N}} + \mathrm{d}R_{\mathrm{N}}$. The slope index Γ is particularly important, because it is associated with evolutionary paths. For instance, Johansen et al. (2015) show that $\Gamma = 3.0$ will be expected if the comets formed by accretion of chondrules in the outer protoplanetary disc, in contrast to $\Gamma = 3.5$ for a collisional evolutionary path (Dohnanyi 1969). However, in cases where the collisional fragments have material strength correlated with size, the slope index varies in different size intervals (O'Brien & Greenberg 2003). If the comets were evolved from accretion of binaries in a dynamically cold disc, the slope index is not a constant either, but

changes from $\Gamma \sim 2$ ($10 \lesssim R_{\rm N} \lesssim 30$ km), to $\sim$5.8 ($2 \lesssim R_{\rm N} \lesssim 10$ km), and then to $\sim$2.5 ($0.1 \lesssim R_{\rm N} \lesssim 2$ km), discovered by Lamy et al. (2004) and Schlichting et al. (2013).

Revealing the size statistics for cometary nuclei is ambiguous compared to asteroids due to presence of comae. One of the methods is to observe comets at large heliocentric distances (e.g., $r_{\rm h} \gtrsim 5$ AU). However, the geometric conditions inevitably lead to faint nucleus signals, and any ongoing weak activity can easily skew estimates of nucleus sizes as well. Another way was first developed by Lamy & Toth (1995) and improved subsequently (e.g., Lamy et al. 1998), which is the cometary nucleus-extraction technique. It removes contribution from the coma with some empirical models which are fitted from the observation, and measured the leftover signal from the coma-model-subtracted images.

This technique has been widely used since it appeared in the literature (e.g., Lisse et al. 1999; Lamy et al. 2007; Fernández et al. 2013; Bauer et al. 2015). In a few cases it did reveal nucleus sizes in excellent agreement with measurements in situ by spacecraft (19P/Borrelley, Lamy et al. 1998; 81P/Wild 2, Fernández et al. 1999; 9P/Tempel 1, Fernández et al. 2003; and 103P/Hartley 2, Lisse et al. 2009). However, in other cases it can also fail terribly (e.g., *Hubble Space Telescope* (*HST*) observations of comet C/2013 A1 (Siding Spring), J.-Y. Li, private communication; Bauer et al. 2017). Therefore, it is inevitable to question the reliability of this technique. In this paper, we endeavoured to investigate this point, and present our results.

4.2 Method

The basic idea of the nucleus-extraction technique is that the signal from a coma and a nucleus are separable, and that the coma profile can be fitted by some simplistic model, which can be mathematically expressed as

$$F_{\rm m}\left(\rho,\theta\right) = k_{\rm N}\mathcal{P} + \left[k_{\rm C}\left(\theta\right)\rho^{-\gamma(\theta)}\right] * \mathcal{P}. \tag{4.2}$$

Here $F_{\rm m}$ is the modelled flux of the comet as a function of the projected distance on the sky plane from the coma optocenter ρ and the azimuthal angle θ, the symbol $*$ is the convolution

operator, and $\mathcal{P}$ is the point-spread function (PSF) of the used optical system. In reality, shapes of PSFs can vary as a function of pixel coordinates of an image. In our experiment, PSFs remain constant across the field-of-view. We started with Gaussian PSFs.

The first term in the right-hand side of Equation (4.2) represents the contribution from the nucleus flux, viz., the PSF scaled by a factor k_{N}. Signal from the coma is represented by the second term, which is assumed to be a power-law distribution in this work. The scaling factor k_{C} and the slope index γ are both free parameters to be fitted from observations from a certain portion (annulus of inner and outer radii ρ_1 and ρ_2, respectively) of the coma, ideally without contamination from the nucleus signal. A crucial assumption of the method is that the portion of near-nucleus coma can be extrapolated from the coma-fitting region, regardless of what specific function is adopted to fit the coma. The coma-model image, which was constructed on a finer pixel grid with subsampling factor $\mathcal{S}$, is shifted by $|\Delta x| < 1$ and $|\Delta y| < 1$ in the subpixel grid, meaning that a total number $(2\mathcal{S}+1)^2$ of coma-model images were produced. Each coma-model image was then rebinned back to the original resolution, and subsequently subtracted from the observed image. The resulting images are termed leftover images, where we measured the remaining flux presumably from the nucleus, by means of aperture photometry, whose centroid was also shifted in the subsampled pixel grid. The scaling factor for the nucleus signal k_{N} is then the ratio between the remaining flux and the flux of a normalised PSF measured in the same photometry configuration. We then constructed scaled-PSF images whose centers were determined by the subpixel coordinates of the photometry centroid, which were subsequently subtracted from the nucleus images, leaving us residual images. The goodness of fit was then calculated from summation of the residual counts weighted by flux uncertainty over the central region:

$$\chi^2\left(x_{\mathrm{C}}, y_{\mathrm{C}}, k_{\mathrm{N}}, x_{\mathrm{N}}, y_{\mathrm{N}}\right) = \sum_{x,y} \frac{\left(F_{\mathrm{m}} - F_{\mathrm{o}}\right)^2}{\sigma_{F_{\mathrm{o}}}^2}, \tag{4.3}$$

where x_{C} and y_{C} are pixel coordinates of the coma peak, x_{N} and y_{N} are for the nucleus, and $\sigma_{F_{\mathrm{o}}}$ is the flux uncertainty at pixel coordinates (x, y), which is computed from

$$\sigma_{F_{\mathrm{o}}}\left(x, y\right) = \frac{1}{t_{\mathrm{exp}}}\sqrt{\frac{1}{\mathcal{G}}\left[F_{\mathrm{o}}\left(x, y\right) t_{\mathrm{exp}} + \frac{\sigma_{\mathrm{RN}}^2}{\mathcal{G}}\right] + \mathfrak{f}^2 F_{\mathrm{o}}^2\left(x, y\right) t_{\mathrm{exp}}^2}. \tag{4.4}$$

Here, $\mathcal{G}$ and $\sigma_{\rm RN}$ are respectively the gain and readout noise of the observing CCD, $t_{\rm exp}$ is the exposure time, and $\mathfrak{f}$ represents the flat-field noise in a unit of the source signal. Our way to obtain $k_{\rm N}$ is reliable if the leftover profile is similar to that of a scaled PSF; no further aperture correction is needed.

In this work, we opted to create a series of synthetic symmetric power-law comae with different coma-slope indices, and then added synthetic nuclei of different brightness to the synthetic images at the optocenter of comae. Noise was added to the images by arbitrarily adopting $\mathcal{G} = 1.56$ e$^-$/DN, $\sigma_{\rm RN} = 3.08$ e$^-$, $\mathfrak{f} = 0.01$, and $t_{\rm exp} = 285$ s in Equation (4.4).[1] Our synthetic coma is circularly symmetric, i.e., no dependence upon θ. A singularity exists at the optocenter of the coma ($\rho = 0$). Our solution was to compute a multiplicity coefficient μ under the polar coordinates, which is a function of the coma-slope index as

$$\mu\left(\gamma\right) = 2\frac{\iint_{\mathfrak{S}_0} \rho^{1-\gamma(\theta)} \mathrm{d}\theta \mathrm{d}\rho}{\iint_{\mathfrak{S}_1} \rho^{1-\gamma(\theta)} \mathrm{d}\theta \mathrm{d}\rho}, \tag{4.5}$$

where region $\mathfrak{S}_0$ is defined by radii ranging from $0 \leq \rho \leq 1$ pixel and azimuths from θ to $\mathrm{d}\theta$, and $\mathfrak{S}_1$ has $1 \leq \rho \leq 2$ pixels and the same azimuthal limit as $\mathfrak{S}_0$. The meaning of μ is simply the ratio between the mean pixel count at the peak of the coma and that at the adjacent pixel. In cases where the coma slope index is nearly a constant, and satisfies $\gamma < 2$, Equation (4.5) can be simplified to be

$$\mu\left(\gamma\right) = \frac{3}{2^{2-\gamma} - 1}. \tag{4.6}$$

We plot μ versus γ in Figure 4.1. For the best-fit coma models, the replacement of the singularity was done in the same manner, yet the central pixel of the coma is assigned by a mean value:

$$F_{\rm C}\left(\rho = 0\right) = \frac{\int_0^{2\pi} \mu\left(\gamma\right) k_{\rm C}\left(\theta\right) \mathrm{d}\theta}{2\pi}, \tag{4.7}$$

since when constructing best-fit coma models, we assumed nothing about the symmetry of the coma. Therefore the obtained $k_{\rm C}$ and γ could vary azimuthally.

The nucleus-extraction technique was then applied on these synthetic images, whereby we obtained a set of values of the nucleus signal. We then compared the original nucleus

[1] These used values are typical for, e.g., *HST* observations.

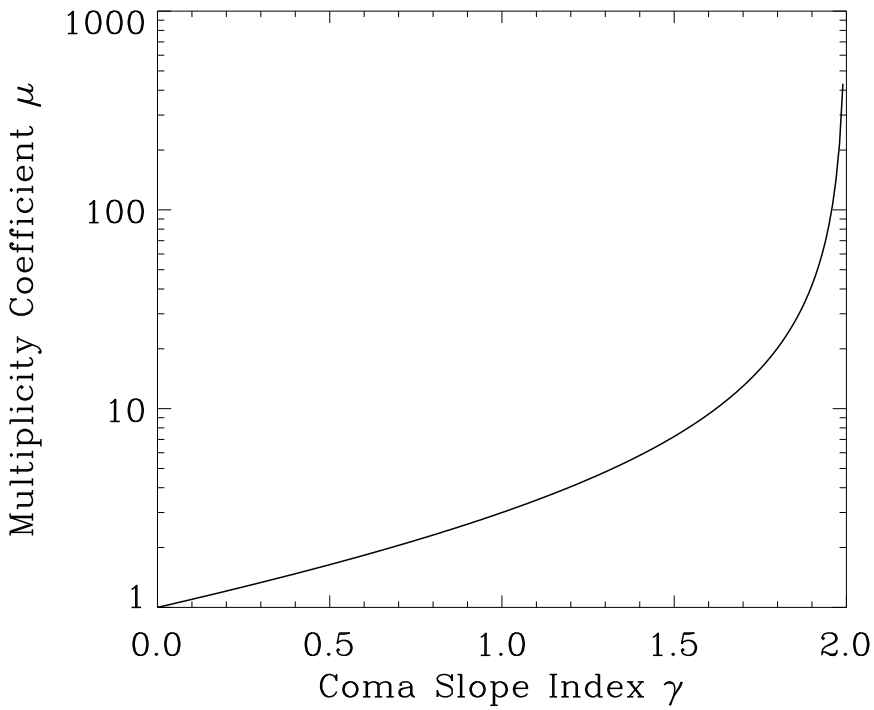

Figure 4.1: The multiplicity coefficient μ, which is defined as the ratio between the mean pixel count at $\rho = 0$ from the peak of coma and that at the adjacent neighbouring pixel in the polar coordinates system, as a function of the coma slope index γ. According to observations of comets, typical coma slope indices remain within $1.0 \lesssim \gamma \lesssim 1.5$.

signal and the nucleus signal extracted from the synthetic images, and evaluated the successfulness of the technique. With this approach, we quantitatively assessed how good/bad this technique is and under what conditions we can reliably extract the nucleus photometry. We arbitrarily picked $k_{\rm C} = 5$ DN s^{-1}, and used $\rho_1 = 10$ pixels and $\rho_2 = 90$ pixels to fit the comae (see Section 4.3.4).

4.3 Results

Our results revealed an obvious systematic bias in the nucleus-extraction technique, strongly depending on how bright the nucleus is with respect to the surrounding coma. The fainter the nucleus is, compared to the surrounding coma, the more biased the technique becomes. For this reason, hereafter we express nucleus signal in terms of parameter η, the ratio between the nucleus flux and the total flux, enclosed by a circular aperture of radius $\rho_{\rm aper} = 15$ pixels, which is arbitrarily chosen. Other factors that influence the bias include the PSF, the subsampling factor, the steepness of the coma surface brightness profile, and the coma-fitting region. In this work, the bias $\mathcal{B}$ is computed through the following equation

$$\mathcal{B} = \frac{k_{\rm N}^{\rm (m)} - k_{\rm N}^{\rm (o)}}{k_{\rm N}^{\rm (o)}} \times 100\%, \tag{4.8}$$

where the superscripts (m) and (o) denote the calculated and the real values, respectively. If $\mathcal{B} < 0$, the technique underestimates values for the nucleus signal.

4.3.1 PSF

We studied the effect from PSFs by choosing a narrow (FWHM = 1.0 pixel), a moderate (3.0 pixels) and a wide (5.0 pixels) ones. For the wide-PSF case, we changed the inner radius to 20 pixels, otherwise the fitted region will be noticeably contaminated by the nucleus signal, leading to serious oversubtraction of the central region. The result is shown in Figure 4.2, where we can see that for the narrow-PSF case, the systematic bias is less significant than the others. So we infer that the bias becomes worse as FWHM of PSF increases. This correlation is within our expectation, because, convolution with wider PSFs essentially blurs

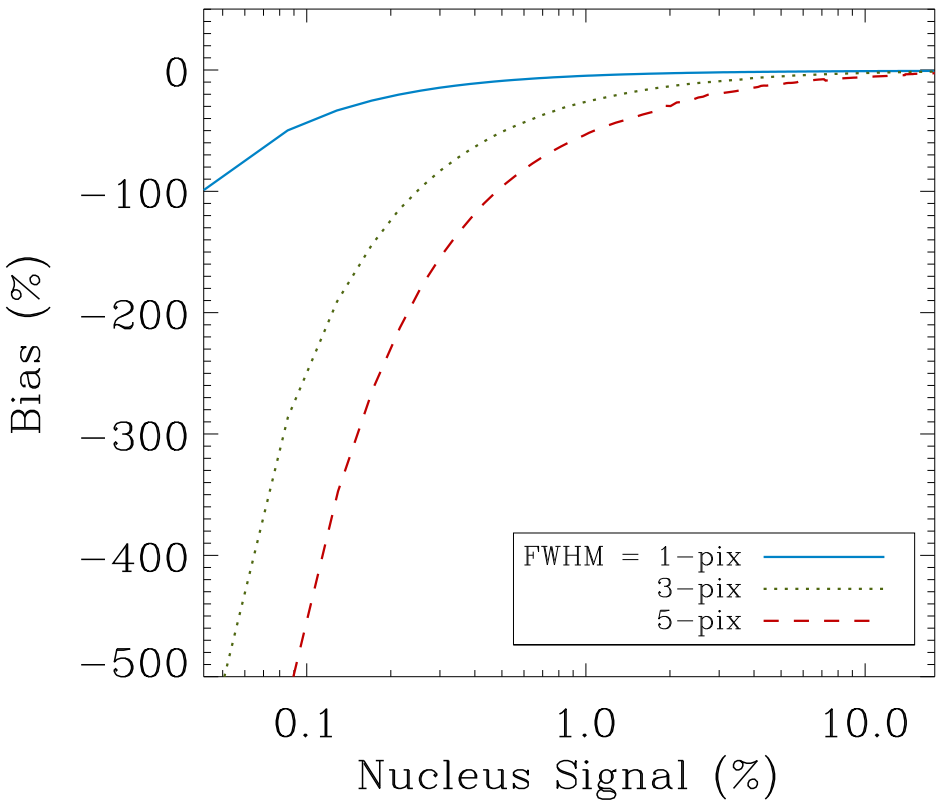

Figure 4.2: The systematic bias as a function of nucleus signal in terms of the ratio between the nucleus flux and the total flux enclosed by a 15-pixel radius aperture, and the FWHM of PSFs. The smaller is the FWHM of PSF, the less is the bias, which asymptotically approaches zero as the fraction of nucleus signal increases. Note that the inner radius of the coma-fitting region for FWHM = 5 pixels is changed from $\rho_1 = 10$ pixels to 20 pixels to avoid signal contamination from the synthetic nucleus. The outer radius is $\rho_2 = 90$ pixels.

features more, and thus leads to loss of original information. The indication is that in reality, good seeing and sharp imaging are two of the requirements for ground-based telescopes to perform observations seeking for nucleus sizes.

4.3.2 Subsampling Factor

Researchers have been using a variety of different subsampling factors in literatures. For example, Lisse et al. (1999) used a subsampling factor of $\mathcal{S} = 5$, Lamy et al. (1998) used 8, and Li et al. (2017) used 10, etc. However, as shown in Figure 4.3, in which we tested odd subsampling factors from 1 (no subsampling) to 9 with a Gaussian PSF of FWHM = 3 pixels, the technique is found to have an obvious systematic bias as a function of the subsampling factor. At a first glimpse, surprisingly, the bias trend for $\mathcal{S} = 9$ is worse than that for $\mathcal{S} = 3$. We think that the origin of this problem is closely related to the arrangement of the pixel value at $\rho = 0$, which is a singularity in Equation (4.2). In our computation, we replaced the singularity using Equation (4.6). If we instead perform substitution of the singularity with the mean of the closest neighbouring pixel values, the bias trends for small $\mathcal{S}$ are impacted, but the influence dwindles as $\mathcal{S}$ increases. If the singularity is replaced by some larger number than given by Equation (4.6), the order of the bias trends can be completely reversed. This is to say, the bias trend for $\mathcal{S} = 1$ becomes the worst by having the most negative values, whereas the one for $\mathcal{S} = 9$ not only becomes the best of all, but also remains largely unchanged from the one with the singularity replaced by Equation (4.6). Therefore, we recommend using large $\mathcal{S}$ so as to minimise effects from the way that the singularity at $\rho = 0$ is handled. However, inevitably this costs more computation time as $\mathcal{S}$ increases.

The original purpose for subsampling is to find out the subpixel locations of coma and nucleus centers, because, in reality, they do not necessarily overlap in images, as a result from inhomogeneous activity. So, we specifically investigated this issue, by creating circularly symmetric coma models, but with non-overlapping nucleus and coma centers. We tested three different scenarios:

1. Nucleus shifted only, where the location of the nucleus center is shifted arbitrarily from

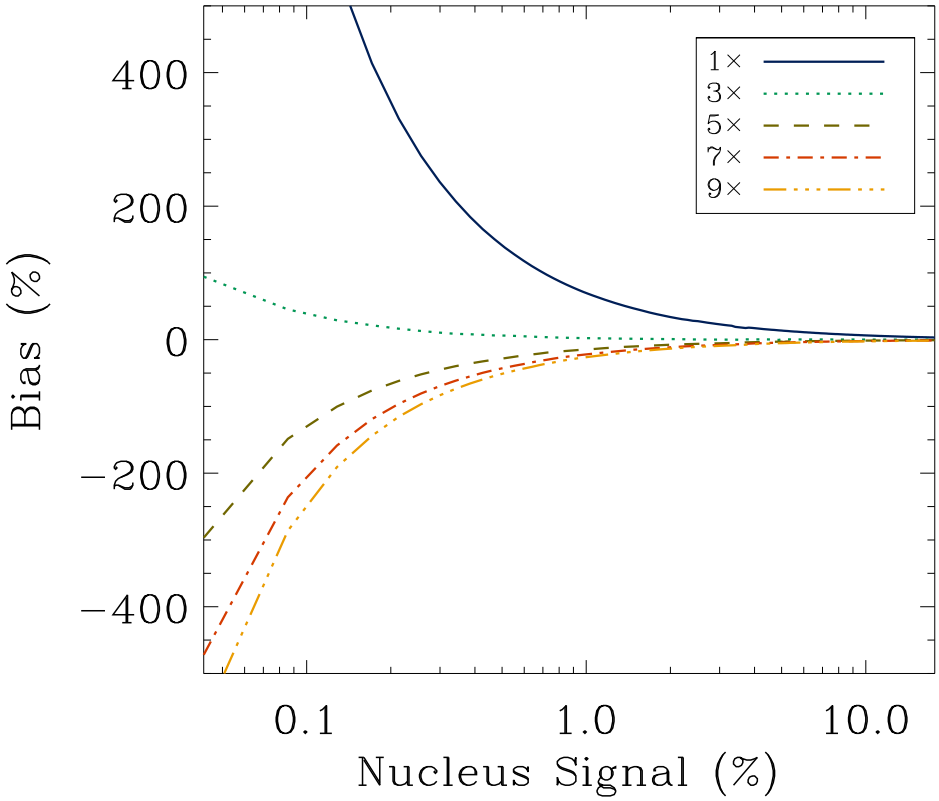

Figure 4.3: The systematic bias for $\rho_1 = 10$ pixels and $\rho_2 = 90$ pixels as a function of the nucleus signal and the subsampling factor for the case where the coma and nucleus are both located at the same pixel center. Note that only those with odd numbers of $\mathcal{S}$ are plotted, because the central pixel of images has the peak of coma and is the symmetric point. Nevertheless, the purpose is to demonstrate that as $\mathcal{S}$ becomes larger, the change between neighbouring bias trends shrinks. Although in this plot, the bias with $\mathcal{S} = 3$ appears to be the least, yet, once a different scheme is adopted to replace the singularity, it will be altered wildly. By contrast, the one with $\mathcal{S} = 9$ is not changed visually. Therefore, we suggest that a large subsampling factor should be used.

the coma center by some subpixel displacement, whereas the center of coma remains at a pixel center.

2. Coma shifted only, where the coma center is shifted by some subpixel displacement whereas the location of the nucleus center is situated at a pixel center.

3. Both coma and nucleus shifted, by different amounts of subpixel displacements.

We relaxed the search region for nucleus centers to $|\Delta x| \leq 3$ and $|\Delta y| \leq 3$, because otherwise there are cases where the obtained centers occur at the boundary of the original search region described in Section 4.2. All the three scenarios were found to have broadly similar results. The bias trend for the largest subsampling factor we tested, i.e., $\mathcal{S} = 9$, is found to be the least affected, as the global shape is similar to the one in Figure 4.3. The major difference that there are kinks present in Figure 4.4 due to the sudden jumps of the best-fitted coma and nucleus center values in the subpixel grid. The kinks are even more prominent for smaller values of $\mathcal{S}$, which is in line with the fact that asymmetric patterns in leftover and residual images are more severe as $\mathcal{S}$ decreases. Therefore, larger $\mathcal{S}$ ought to be adopted.

We also found that, under no circumstances could we recover the a priori location offsets of the nucleus and coma centers from the pixel center. The reason is that, when we constructed the coma model from the best-fit parameters, the origin has already been set to the peak pixel center of the whole comet, which comprises of both the nucleus and the coma. The best-fit parameters for the coma then clearly become sinusoidal (see Figure 4.5), which are already deviated from the a priori parameters. Therefore, we conclude that, the subsampling operation fails to unravel the actual displacement information. The original purpose of subsampling cannot be fulfilled, unless for each subpixel shifted locations of the coma center, the best-fit coma model is recalculated, which is extremely time consuming and possibly unnecessary, since the bias trends for large $\mathcal{S}$ are similar to symmetric cases except for the existence of kinks. This suggests that the extraction technique is able to yield reasonably good nucleus-size estimates for comae of typical slopes, merely off by no more than a few

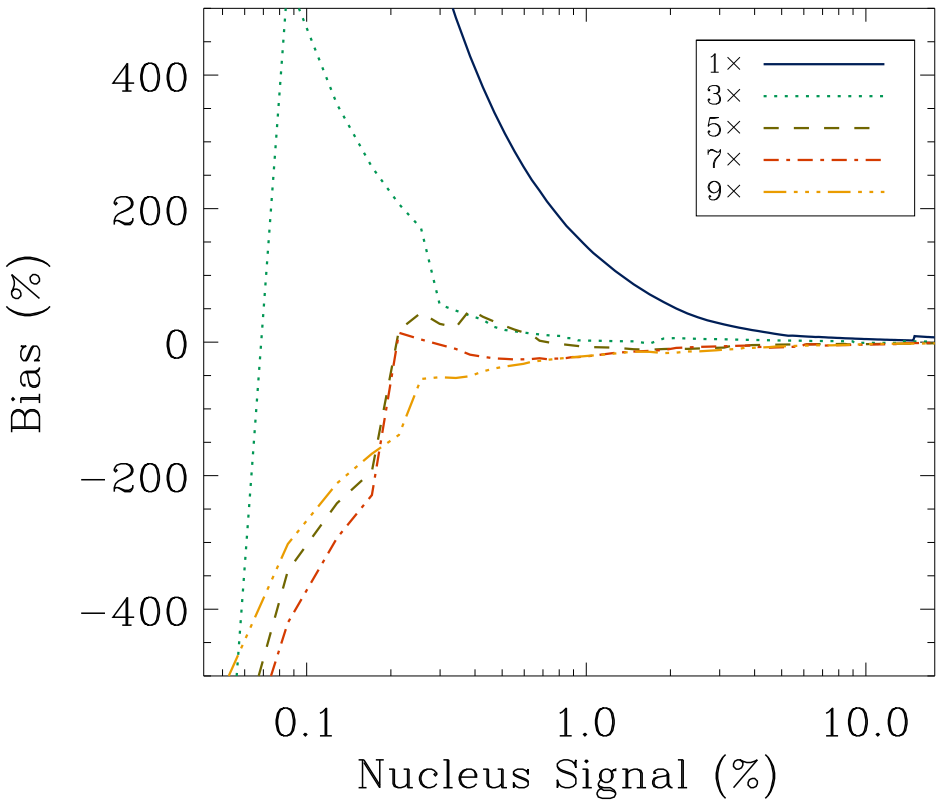

Figure 4.4: The same plot as Figure 4.3, but with a symmetric steady-state coma with its center offset by $(\Delta x, \Delta y) = (-0.389, +0.452)$ and the nucleus shifted by $(+0.247, +0.113)$, both from a common pixel center. When the nucleus signal has $\eta \gtrsim 1.0\%$, the shapes of the bias trends are broadly the same as in Figure 4.3. However, when $\eta \lesssim 1.0\%$, kinks due to sudden leaps in best-fit nucleus and coma centers are clearly present. Amongst the subsampling factors we tested, $\mathcal{S} = 9$ has the smallest kinks, in agreement with its leftover and residual images having the least asymmetric patterns.

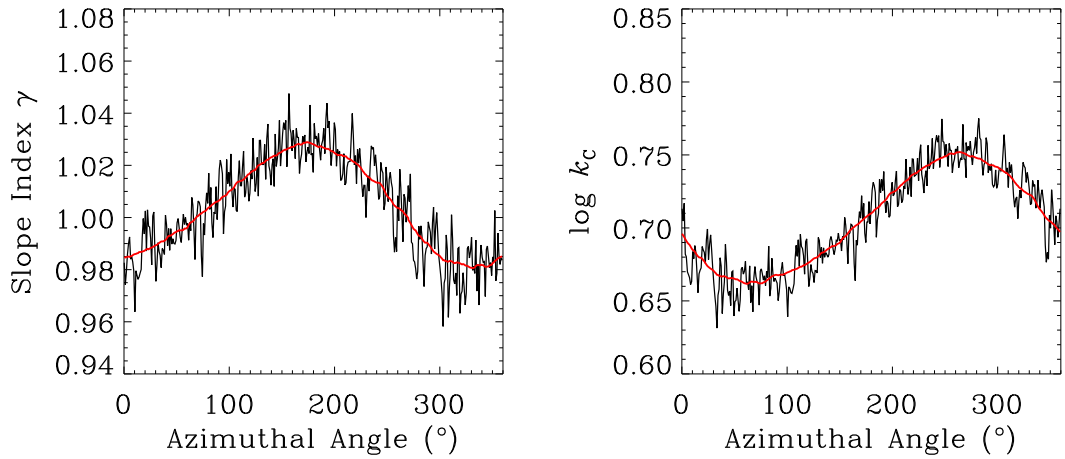

Figure 4.5: The best-fit parameters of the slope index γ (left) and the scaling factor $k_{\rm C}$ (right, in logarithmic space) from an example of a circularly symmetric coma, which has a priori $\gamma = 1.0$ and $k_{\rm C} = 5.0$ DN s^{-1}, but has the nucleus arbitrarily shifted by $(\Delta x, \Delta y) = (+0.253, +0.617)$ from the pixel centre, which is also the coma center. The red line in each panel is the smoothed value of the corresponding parameter.

percent, if one uses large values of $\mathcal{S}$ (e.g., $\mathcal{S} \gtrsim 7$) when the nucleus is not too faint with respect to the surrounding coma (e.g., $\eta \gtrsim 10\%$).

4.3.3 Slope of Coma Surface Brightness

We present the systematic bias of the nucleus-extraction technique with the Gaussian PSF of FWHM = 3 pixels as a function of the steepness of the coma surface brightness in Figure 4.6. The slope index γ varying between 0.9 (which is slightly less steep than the one in a steady-state coma, i.e., $\gamma = 1.0$) and 1.5 (corresponding to a coma under the influence of the solar radiation pressure; Jewitt & Meech 1987), in a step of 0.1, has been tested. We fixed $\mathcal{S} = 9$. Our result is that the magnitude of systematic bias shrinks as the coma becomes less steep. The reason is that the convolution with the PSF generally has more influence upon coma surface profiles of larger values of γ. For a hypothetic coma which is completely flat across the whole image, i.e., $\gamma = 0$, convolution will not change its profile at all, so such a

coma model can be accurately constructed from the observed profile without any loss, which is unfortunately not the case for comae of steeper γ. Given the coma-fitting region, as γ increases, the technique tends to overestimate the slope index more significantly, resulting in oversubtraction of the coma.

4.3.4 Coma-Fitting Region

The bias of the nucleus-extraction technique comes into being whenever the coma profile cannot be perfectly reproduced. If the modelled coma is forced to be constructed using a priori values of parameters k_{C} and γ, the bias will no longer exist above the noise level. We found that how the coma-fitting region is selected strongly affects the bias trend. We thus decided to qualitatively investigate what this relationship is by varying the inner and outer radii of the annulus within which the coma profile is fitted.

We found that the trends for comae of different γ and Gaussian PSFs of different FWHM are the same. When ρ_1 is small, the signal around the central region of the coma is overestimated, thereby leading to an underestimated nucleus signal. As ρ_1 increases, the technique then begins to systematically overestimate the nucleus signal. When the annulus is too narrow, e.g., $2\rho_1 \gtrsim \rho_2$, the constructed coma models are no longer good approximation to the synthetic ones by being strongly asymmetric, due to the existence of noise. Before the annulus becomes too narrow, increasing ρ_1 whilst decreasing ρ_2 can reduce the systematic bias.

The behaviours can be understood from Figure 4.7, which shows the pre-/post-convolution radial profiles of a steady state coma with the Gaussian PSF having FWHM = 3.0 pixels in the logarithmic space. It is visually obvious that the slope of the post-convolution profile is steeper than the pre-convolution one when $2 \lesssim \rho \lesssim 10$ pixels. So if this portion of the coma is fitted, the modelled coma will then have a steeper best-fit γ, which gets even steeper after convolution with the PSF. This is the reason why smaller ρ_1 leads to oversubtraction of the central region. In addition to this, nucleus signal extended by PSF convolution worsens the deviation, leading to even worse oversubtraction. Starting from $\rho \sim 20$ pixels (not shown

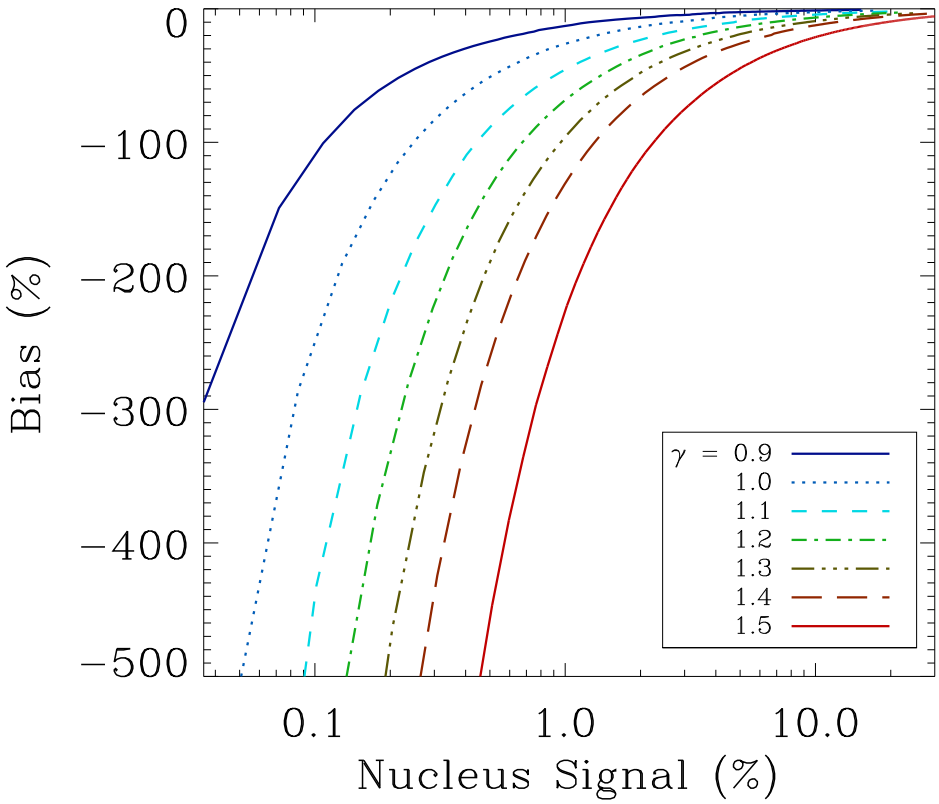

Figure 4.6: The systematic bias for $\rho_1 = 10$ pixels and $\rho_2 = 90$ pixels as a function of the nucleus signal and the slope index of the coma γ. As we can see, steeper slopes result in larger bias. Hypothetically, a coma with $\gamma = 0$ should have a zero bias trend regardless of the nucleus signal percentage, because the convolution operation strictly does not change the slope at all.

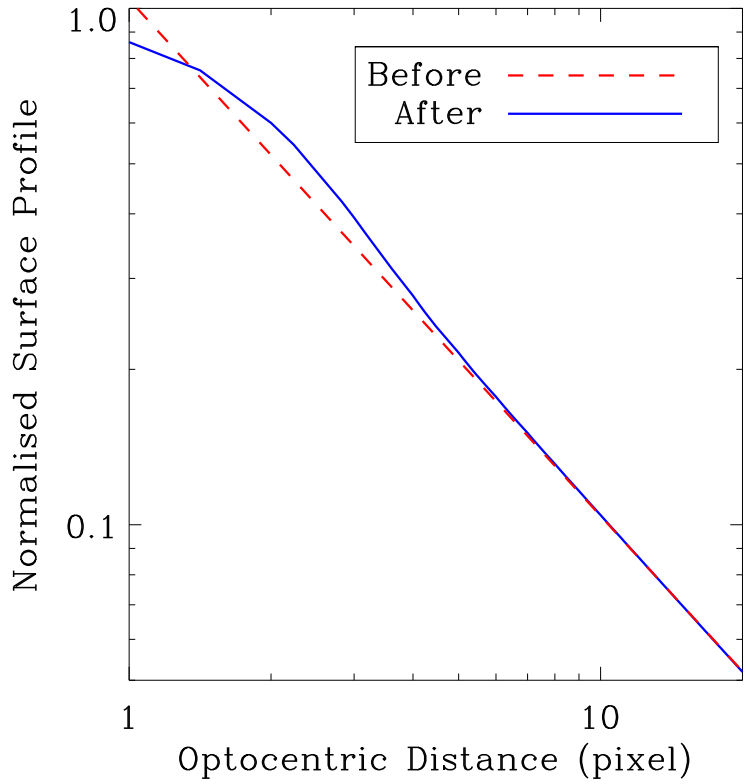

Figure 4.7: Comparison between the radial profiles of the ρ^{-1} coma (red dashed line) before and after convolution with Gaussian PSF of FWHM = 3 pixels (blue solid line), as an example. The profiles are normalised by the peak value of the post-convolution one. No nucleus is added to the model. Within $1.2 \lesssim \rho \lesssim 13$ pixels, the post-convolution profile is brighter than the pre-convolution one. For $\rho \gtrsim 13$ pixels, the post-convolution profile is always fainter than the pre-convolution one, but the difference shrinks as ρ increases.

in Figure 4.7, because the difference is extremely tiny), the slope of the post-convolution profile becomes less steep than the pre-convolution slope, and the two curves converge in an asymptotic manner. Thus, if this portion of the coma is used to construct the coma model, the central region will be underestimated. Ideally, the larger are ρ_1 and ρ_2, the better will be the best-fit coma model. However, seldom can this be realised in reality, because the signal of this portion of coma may well have insufficient SNR or can be blended with background sources. Also, comets tend to have changes in activity as functions of time, resulting in non-extrapolatable radial profiles. So in these cases the obtained coma model may be even worse than the one constructed from the portion where distortions by convolution with PSF are present.

Obviously these behaviours are highly dependent on the PSF, and also sensitive to the coma profile. So we cannot think of a simple way which can be applicable to all scenarios in reality to debias results from the nucleus-extraction technique. We did attempt to search for best-fit parameters for the synthetic comae after applying deconvolution to the synthetic comet images. However, it did not necessarily provide us with less biased results, because the noise was amplified after the operation. Neither did we determine how good the SNR should be for this procedure to work due to entangling complication factors. What we found is that for comets with typical SNR comparable to those observed by the *HST* (e.g., 19P, Lamy et al. 1998; C/2017 K2, Jewitt et al. 2017), deconvolution does not bring in observable improvement whatsoever, but may even deteriorate the bias. We thus conjecture that this systematic bias is probably uncorrectable. Generally speaking, we strongly recommend that, in order to obtain a reliable nucleus value, high resolution imaging about the coma with SNR as high as possible is a must. Otherwise we will expect an enormous bias stemming from the technique.

4.4 Tests with *HST* Observations

The *HST* plays a unique role in measuring cometary nucleus sizes with the nucleus-extraction technique that we discussed here. It has three advantages over almost all ground-based

telescopes to apply this technique:

1. The high spatial resolution attenuates the coma signal relative to the nucleus signal in the central region.

2. The high resolution also shortens the physical distance of inner coma to be extrapolated from the coma model.

3. It has the extremely stable PSFs resulted from being in space, allowing for accurate fitting to the nucleus.

The *HST* has been providing high-spatial resolution images of comets since its operation, e.g., 19P (Lamy et al. 1998), 252P (Li et al. 2017), C/2012 S1 (Lamy et al. 2014), C/2017 K2 (Jewitt et al. 2017), etc. A number of nucleus sizes or constraints have been obtained through the telescope. We thus feel the necessity to adopt the PSF of cameras WFPC2 and WFC3 onboard the *HST*, examine the bias trends from the nucleus-extraction technique, and also assess quality of extracted nucleus values from some of these observations.

We performed completely the same procedures as we did for the Gaussian case on synthetic comet models with the WFPC2/WFC3 PSFs. The bias trends (see Figures 4.8 and 4.9) are generally similar to those presented in Figures 4.3 and 4.6, given that a larger inner radius of the coma-fitting region ($\rho_1 = 15$ pixels for both cameras) was used. We found that the change of the bias trends with regard to the coma-fitting region differs from that in the Gaussian case. The radial profile of post-convolution image has a steeper slope starting from $\rho \lesssim 20$ pixels, wherein it is also slightly brighter. Thus, with the used ρ_1 and ρ_2, the technique systematically oversubtracts the central region (Figures 4.8 and 4.9). Otherwise, choosing smaller radii of the coma-fitting region (e.g., $\rho_1 = 7$ pixels, $\rho_2 = 30$ pixels) leads to undersubtraction of the coma in the central region, because the slope of the post-convolution radial profile therein is shallower. Our argument that a high subsampling factor value shall be exploited mainly to avoid influence from inaccuracy of the singularity replacement is reinforced (see Figures 4.8a & 4.9a).

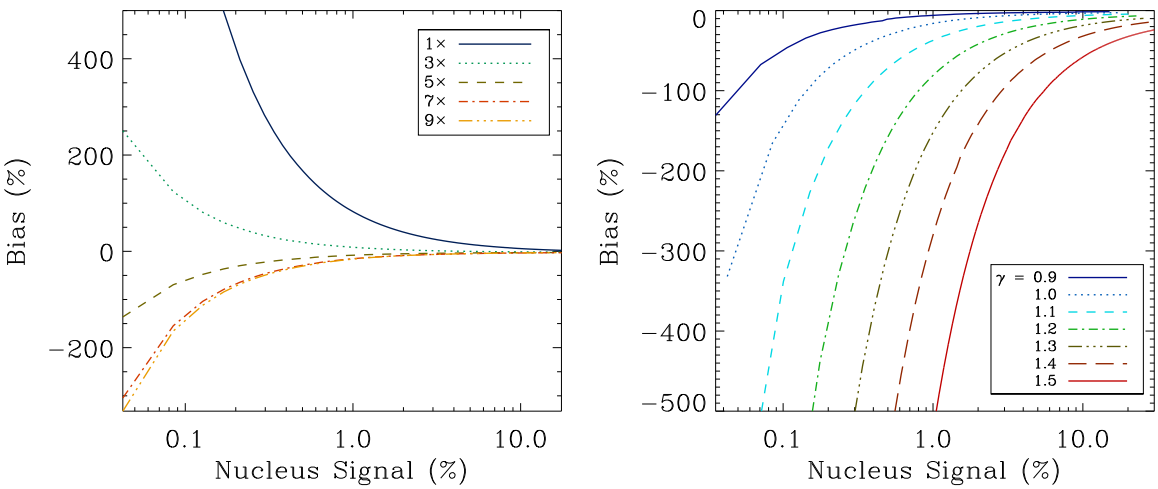

(a) (b)

Figure 4.8: The systematic bias trend with the *HST*/WFPC2 PSF as functions of the nucleus signal versus the subsampling factor (a) and the slope index of the coma (b). The coma-fitting region has $\rho_1 = 15$ pixels and $\rho_2 = 90$ pixels from the peak of the comet profile.

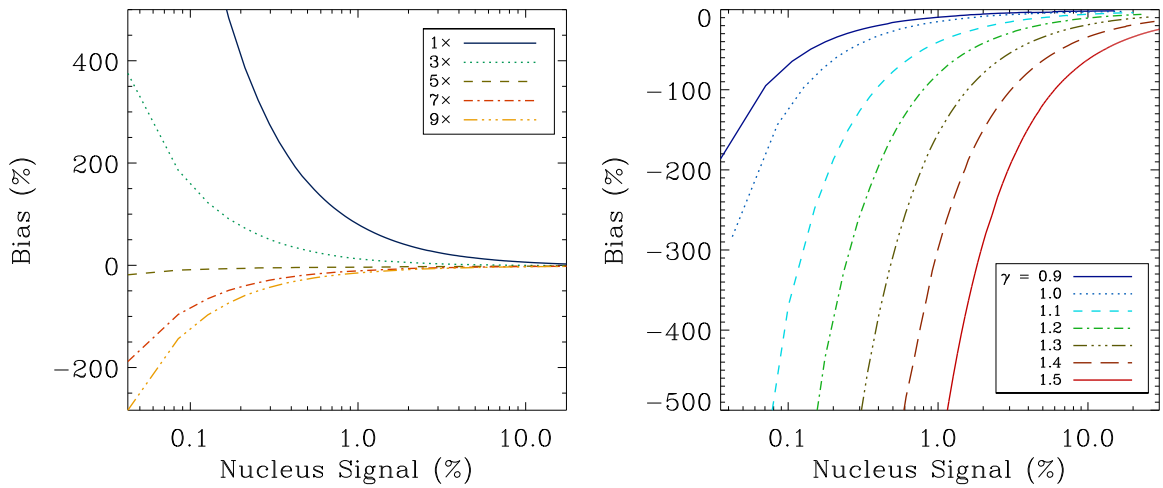

(a) (b)

Figure 4.9: Same as Figure 4.8 but with the *HST*/WFC3 PSF. We again chose $\rho_1 = 15$ pixels and $\rho_2 = 90$ pixels from the peak of the comet profile to fit the coma. General trends are basically similar to those in Figure 4.8 with the *HST*/WFPC2 PSF.

We then proceeded to assess the quality of the obtained nucleus values from several *HST* observations by the nucleus-extraction technique, where the nucleus sizes are known or constrained. Three comets of different activity levels are selected as representatives: 19P (weakly active), C/2013 A1 (active), and C/1995 O1 (hyperactive). Archival *HST* data were retrieved via the *HST* Moving Target Pipeline[2].

4.4.1 Weakly Active Comet: the Case of 19P/Borrelley

The size and shape of the nucleus of this comet obtained by Lamy et al. (1998) are found to be in remarkable consistence with in situ measurements by the spacecraft Deep Space 1 (see Lamy et al. 2004 and references therein). We applied the nucleus-extraction technique on one of the F675W-filtered *HST*/WFPC2 images from UT 1994 November 28.41. Descriptions of the observation are detailed in Lamy et al. (1998). Cosmic rays were removed by the LA Cosmic package (van Dokkum 2001) prior to applying the nucleus-extraction technique.

[2] `https://archive.stsci.edu/prepds/mt/`

Table 4.1: Results of Nucleus Extraction for 19P/Borrelley

Inner Radius ρ_1 (pixel)	Outer Radius ρ_2 (pixel)	Apparent V Magnitude	Effective Radius $R_{\rm N}$ (km)
7	30	17.28 ± 0.05	1.99 ± 0.28
	50	17.30 ± 0.05	1.97 ± 0.28
	70	17.32 ± 0.05	1.95 ± 0.28
	90	17.39 ± 0.05	1.89 ± 0.27
8	30	17.30 ± 0.05	1.97 ± 0.28
	50	17.32 ± 0.05	1.95 ± 0.28
	70	17.35 ± 0.05	1.92 ± 0.27
	90	17.40 ± 0.05	1.88 ± 0.27
9	30	17.31 ± 0.05	1.96 ± 0.28
	50	17.33 ± 0.05	1.94 ± 0.27
	70	17.37 ± 0.05	1.91 ± 0.27
	90	17.41 ± 0.05	1.87 ± 0.26
10	30	17.29 ± 0.05	1.97 ± 0.28
	50	17.34 ± 0.05	1.93 ± 0.27
	70	17.38 ± 0.05	1.90 ± 0.27
	90	17.43 ± 0.05	1.86 ± 0.26

Notes. Detailed information about the observations can be found in Lamy et al. (1998), who obtained $V = 17.38 \pm 0.04$ with $\rho_1 = 7$ and $\rho_2 = 30$ pixels. A general trend is that as the inner and outer radii grow, the flux from the extracted nucleus decreases. When the inner radius is too big, e.g., $\rho_1 = 15$ pixels, conspicuous artifact is seen in leftover images because the extrapolation of the coma profile is no longer a good approximation. The uncertainties in the apparent magnitudes are computed based on error propagation by combining values yielded by Equation (4.4), errors described in Holtzman et al. (1995), and an assumed error of its color $\sigma_{V-R} = 0.03$, which is the standard deviation of the colors of Jupiter-family cometary nuclei. Uncertainty values in $R_{\rm N}$ are propagated from the errors in the apparent magnitudes and an additional error from the geometric albedo. In comparison, the mean radius in situ measured by the Deep Space 1 is 2.17 ± 0.03 km (Buratti et al. 2004).

The sky background value was computed from near-edge regions sufficiently far from the coma and then subtracted from the observed image. We varied the inner and outer radii to find best-fit parameters for the portion of coma in good SNR. The subsampling factor was fixed to be $\mathcal{S} = 9$. Table 4.1 summarizes the apparent V-band magnitudes of the nucleus of 19P with different coma-fitting region parameters, converted from the extracted fluxes by following the recipes by Holtzman et al. (1995). Estimates of the equivalent circle radius were computed by adopting a R-band geometric albedo of 0.072 ± 0.020, which was scaled to a V-band one with a mean color of Jupiter-family cometary nuclei ($V - R = 0.50 \pm 0.03$; Lamy & Toth 2009; Jewitt 2015), a phase slope of 0.043 mag deg^{-1}, and additionally an opposition surge of 0.3 mag (Li et al. 2007). The trend of extracted values of nucleus signal versus the varying coma-fitting region is in excellent agreement with the results from our synthetic tests, i.e., less oversubtraction as ρ_1 and ρ_2 move inward to the peak of coma. By comparison, Lamy et al. (1998) obtained $R_{\rm N} = 2.12$ km for the nucleus with $\rho_1 = 7$ and $\rho_2 = 30$ pixels, which turns out to be consistent with ours (see Table 4.1), although they exploited an optimisation approach to obtain the scaling factor $k_{\rm N}$ whilst we did not, and they adopted $\mathcal{S} = 8$, a less steep phase slope, and a lower geometric albedo.

Nevertheless, our obtained nucleus size is consistent with the actual value (2.17 ± 0.03 km, cube root of triaxial dimensions by Buratti et al. 2004). During the observation, the nucleus had $\eta \sim 10\%$ within $\rho_{\rm aper} = 15$ pixels, which marginally falls in the regime where the value obtained from the nucleus-extraction technique is less biased. In conclusion, we can see that, in cases where the comet is only weakly active, the nucleus-extraction technique is capable of rendering a reasonable estimate of the nucleus size.

4.4.2 Active Comet: the Case of C/2013 A1 (Siding Spring)

We applied the nucleus-extraction technique on an *HST*/WFC3 image of the comet taken in UT 2014 March 11.11 through the F606W filter, after cosmic rays were cleaned by the LA Cosmic package. Detailed information of the observation can be seen in Li et al. (2014). Our result is that, for coma-fitting regions with large ρ_1 and ρ_2 (e.g., $\rho_1 = 10$ and $\rho_2 = 70$

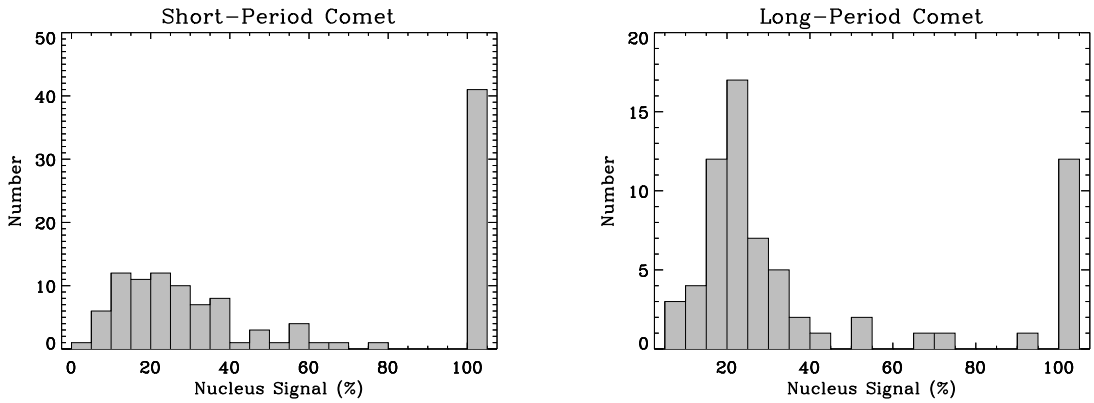

(a) (b)

Figure 4.10: Nucleus-signal statistics of the NEOWISE/WISE comet observations that have measured nucleus sizes (J. Bauer, private communication). Note that a nontrivial number of comets showed no coma in the observations, which are corresponding to the isolated peaks at $\eta = 100\%$ in the two histograms.

pixels), we obtained an oversubtracted central region of the coma, wherein a "blackhole" feature is present in leftover images. For small values of ρ_1 and ρ_2 (e.g., $\rho_1 = 4$ and $\rho_2 = 30$ pixels), instead a fuzzy positive leftover feature is obtained. This is completely the same as our synthetic cases where a nucleus has a tiny η value. In order to verify this, we adopted $R_{\rm N} \sim 0.5$ km as the nucleus size of C/2013 A1 estimated by Farnham et al. (2017) from the HiRISE camera onboard *Mars Reconnaissance Orbiter* (*MRO*) during a close approach to Mars within a distance of $\sim 1.4 \times 10^5$ km (Farnocchia et al. 2014). The corresponding apparent *V*-band magnitude of a bare nucleus of the given size having *V*-band geometry albedo 0.04, and phase coefficient parameter 0.04 mag deg^{-1} will then be $V \approx 25.2$ during the *HST*/WFC3 observation. We measured the total flux centered on the peak in the *HST*/WFC3 image encircled by an aperture of $\rho_{\rm aper} = 15$ pixels in radius, which can be then transformed to apparent magnitude by assuming a Sun-like color. We obtained $V \approx 18.0$. Therefore, the nucleus signal in the same aperture (94.1% of the overall) during the *HST*/WFC3 observation occupied merely $\sim$0.12% of the total flux. Taking the associated uncertainties in our assumption into consideration, we remain highly confident that the nucleus signal did not exceed $\sim$0.1%, exactly falling in the regime where the technique

terribly biases actual nucleus sizes (e.g., Figure 4.9b). Therefore, the failure of the nucleus-extraction technique is totally within our expectation, and we envision that similar failures will occur to other active comets, unless observations are conducted during close encounters which boost the fraction of nucleus signal $\gtrsim$10%. Given this, we suggest that nucleus-size distribution statistics of long-period comets with optical data might not be reliable, since, except a few (Hui 2018), the long-period comets are generally more active than short-period comets, thereby more susceptible to the bias. However, infrared data like those from NEOWISE/WISE, despite suffering from low resolution, can be helpful for studies of cometary nucleus sizes, because the signal from the nucleus is often dominant in the total flux (see Figure 4.10) in the infrared even for active comets in optical wavelengths. In this regard, the infrared observations are able to "downgrade" the activity level of a comet. We thereby infer that the surprisingly flat nucleus-size distribution of long-period comets by Bauer et al. (2017) is probably real, but meanwhile, we encourage more similar or even higher-quality observations in the future.

4.4.3 Hyperactive Comet: the Case of C/1995 O1 (Hale-Bopp)

We downloaded an F675W image of the comet taken by the *HST*/WFPC2 in UT 1996 October 17.64. Details about the *HST* observations are given in Weaver at al. (1997). We conducted the same procedures as in Sections 4.4.1 and 4.4.2. Results of the extracted nucleus-size values from a series of inner and outer radii are listed in Table 4.2, with V-band geometric albedo 0.04 ± 0.03, the phase function coefficient 0.04 mag deg^{-1}, and a mean color of nuclei of nearly isotropic comets ($V - R = 0.44 \pm 0.02$; Lamy & Toth 2009; Jewitt 2015). Our results are consistent with previous attempts to reveal the size of the nucleus (effective radius $R_{\rm N} = 30 \pm 10$ km; Fernández 2002). However, we are aware that the shapes of the leftover completely differ from the *HST*/WFPC2 PSF, where asymmetric patterns similar to strong cometary jets are seen in the images after the coma was subtracted (Figure 4.11). The patterns could not be removed regardless of how we adjusted the coma-fitting region, even if an inappropriately small inner radius $\rho_1 = 4$ pixels was used. This is because the dimension of the jet features is too small compared to the annulus of the coma-fitting

Table 4.2: Results of Nucleus Extraction for C/1995 O1 (Hale-Bopp)

Inner Radius ρ_1 (pixel)	Outer Radius ρ_2 (pixel)	Apparent V Magnitude	Effective Radius R_{N} (km)
4	30	15.66 ± 0.03	28.6 ± 10.7
	60	15.37 ± 0.03	32.7 ± 12.3
	90	15.34 ± 0.03	33.2 ± 12.5
	120	15.38 ± 0.03	32.6 ± 12.2
	150	15.36 ± 0.03	32.8 ± 12.3
7	30	15.15 ± 0.03	36.3 ± 13.6
	60	15.01 ± 0.03	38.5 ± 14.5
	90	15.07 ± 0.03	37.5 ± 14.1
	120	15.10 ± 0.03	37.0 ± 13.9
	150	15.15 ± 0.03	36.2 ± 13.6
10	30	15.01 ± 0.03	38.7 ± 14.5
	60	15.00 ± 0.03	38.7 ± 14.5
	90	15.03 ± 0.03	38.3 ± 14.4
	120	15.11 ± 0.03	36.9 ± 13.8
	150	15.14 ± 0.03	36.4 ± 13.6

Notes. Detailed information about the observations can be found in Weaver et al. (1997). Although nucleus-size estimates are given, it is noteworthy that none of the leftovers resemble the WFPC2 PSF, as there are clear and strong spatial variations that appear to be near-nucleus jets (Figure 4.11). Uncertainties were calculated in the same manner as described in the note of Table 4.1.

region (see Figure 4.11c), thus violating the important presumption of the nucleus-extraction technique – the near-nucleus coma shall be extrapolatable from the outer region. Therefore, solely based upon this aspect, we shall regard the nucleus-size estimates as meaningless, and the method as a failure.

Besides, the other issue that leads to the failure of the method is that comet Hale-Bopp was so active during the observation, such that its coma possibly became optically thick near the nucleus region (Weaver & Lamy 1997). As a result, the dominant flux in the leftover is likely from strong jets in its inner coma, rather than from the nucleus, which coincides in the observed morphology of the leftover. We thus expect a much smaller nucleus size for comet Hale-Bopp than our extracted values. To conclude, this method fails to reveal the nucleus size of comet Hale-Bopp. So will it for other hyperactive comets.

4.4.4 Inference on C/2017 K2 (PANSTARRS)

This comet is identified as a dynamically old member from the Oort cloud, currently on its way to perihelion (Hui et al. 2017; Królikowska & Dybczyński 2018; de la Fuente Marcos & de la Fuente Marcos 2018). Estimates of its mass-loss rate by Jewitt et al. (2017) and Hui et al. (2017) suggest that it is activity level is ordinary in terms of a long-period comet, but on the other hand, remarkable, given the fact that it has been active when it was as far as $r_{\rm h} \approx 24$ AU, which is a record for comets in inbound legs hitherto known (Jewitt et al. 2017; Meech et al. 2017; Hui et al. 2017). Thus, we are curious about its nucleus size, and reanalysed the *HST*/WFC3 observations obtained by Jewitt et al. (2017) from UT 2017 June 27. The images were taken through the broadband F350LP filter and were median combined with registration on the apparent motion of the comet. We applied the nucleus-extraction technique on the coadded image using a series of ρ_1 and ρ_2. Due to the great distance of the comet ($r_{\rm h} = 15.9$ AU) during the *HST* observation, the angular size of the coma where the power law is still a good approximation was not big enough (angular radius $\lesssim 2''$, or 50 pixels; Jewitt et al. 2017), so that we set $\rho_2 \leq 50$ pixels as an upper boundary.

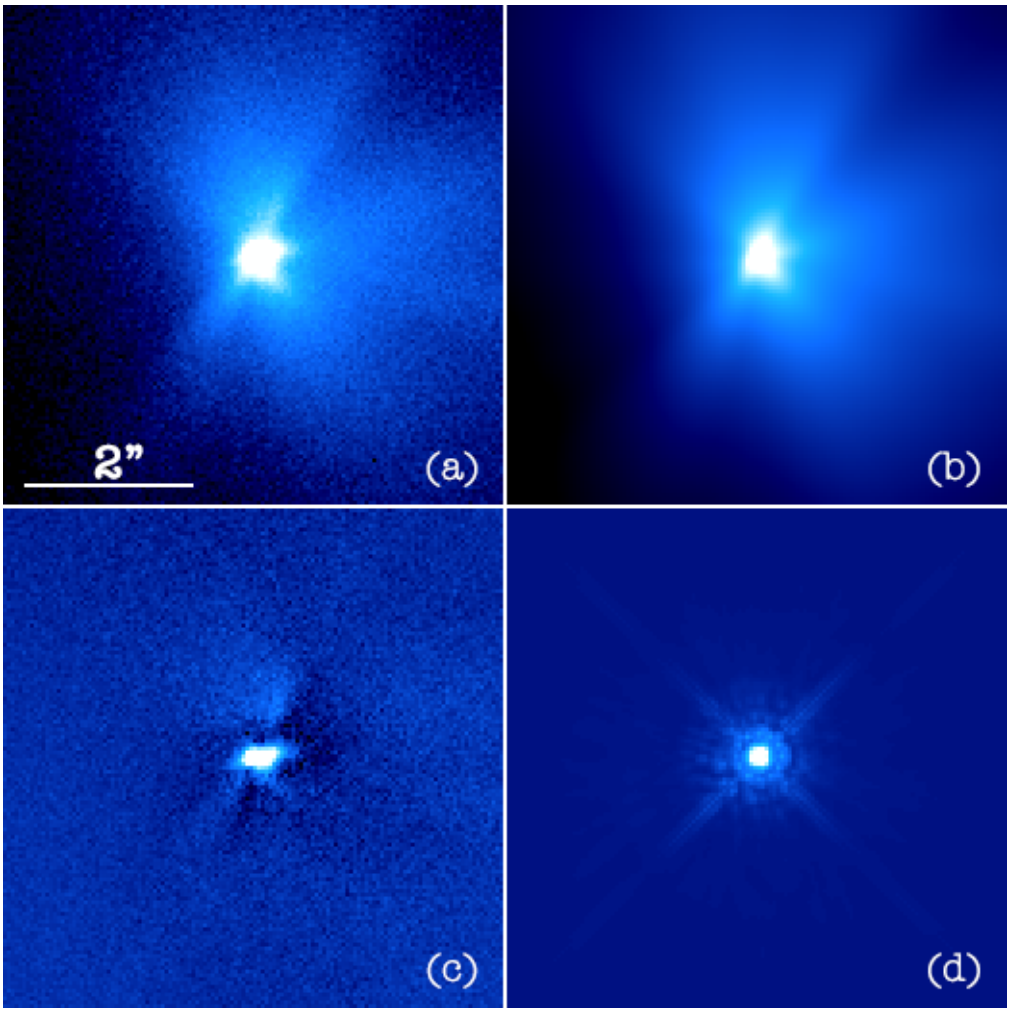

Figure 4.11: Comparison of the observed and model images for the *HST*/WFPC2 C/1995 O1 (Hale-Bopp) data from UT 1996 October 17.64. The upper left and right panels show the observed (a) and modelled (b) images, respectively, which are both stretched logarithmically in the same manner. The coma model was constructed from the annulus with $\rho_1 = 7$ and $\rho_2 = 60$ pixels. The leftover image is displayed in the lower left panel (c), whereas the lower right (d) panel is the PSF of the camera. Also shown is a scale bar. Each panel has a dimension of $5''.9 \times 5''.9$. The difference between the shapes of the leftover and PSF is readily seen, with a normalised rms of the fit $\gtrsim$60 times more than the typical values in our experiment with synthetic comet models.

Table 4.3: Results of Nucleus Extraction for C/2017 K2 (PANSTARRS)

Inner Radius ρ_1 (pixel)	Outer Radius ρ_2 (pixel)	Apparent V Magnitude	Effective Radius R_{N} (km)
6	30	26.66 ± 0.06	4.2 ± 1.1
	40	26.65 ± 0.06	4.2 ± 1.1
	50	26.81 ± 0.07	3.9 ± 1.0
7	30	26.49 ± 0.06	4.5 ± 1.1
	40	26.49 ± 0.06	4.6 ± 1.1
	50	26.78 ± 0.07	4.0 ± 1.0
8	30	26.47 ± 0.06	4.6 ± 1.2
	40	26.50 ± 0.06	4.5 ± 1.1
	50	26.79 ± 0.07	4.0 ± 1.0
9	30	26.44 ± 0.06	4.7 ± 1.2
	40	26.58 ± 0.06	4.4 ± 1.1
	50	26.80 ± 0.07	3.9 ± 1.0
10	30	26.25 ± 0.05	5.1 ± 1.3
	40	26.58 ± 0.06	4.4 ± 1.1
	50	26.76 ± 0.06	4.0 ± 1.0

Notes. Detailed information about the *HST* observation can be found in Jewitt et al. (2017). Although we give nucleus-size estimates, they are expected to be strongly biased, and therefore not reliable, because, if so, the nucleus only contributed a fraction of $\eta \lesssim 0.7\%$ of the total signal. Uncertainties in the apparent magnitudes are statistical errors only, computed from Equation (4.4), which are significantly smaller than the systematic uncertainties.

We summarized the results in Table 4.3. The nucleus sizes were converted from the apparent magnitudes, with the assumed V-band geometric albedo 0.04 and phase slope 0.04 mag deg^{-1}. It seems that the effective nucleus radius of the comet is $\sim$4–5 km. However, we are aware that the obtained nucleus flux is merely $\lesssim$0.7% of the total flux, suggesting the unreliability of the results. If the coma is extrapolatable all the way to the near-nucleus region, the nucleus sizes revealed by the nucleus-extraction technique are expected to be underestimated. Otherwise it is unclear how the estimates are off from the actual nucleus size.

Instead, we prefer a conservative upper limit to its nucleus size using the threshold of $\eta < 10\%$. Therefore the nucleus during the *HST* observation was $V > 23.3$, corresponding to an equivalent circle radius of $R_{\rm N} \lesssim 20$ km. Future high-resolution observations of the comet aiming at better constraining (or revealing) its nucleus size are certainly encouraged when the comet gets much closer to the Earth, which will potentially boost the fraction of nucleus contribution to the total signal within the same photometric aperture.

4.5 Summary

We assessed the widely used cometary nucleus-extraction technique in a systematic way for the first time. Key conclusions are summarized as follows.

1. Nucleus signal obtained from the nucleus-extraction technique can be strongly biased. The fainter the nucleus with respect to the surrounding coma, the more biased is the extracted value. Only when the nucleus signal occupies $\gtrsim$10% of the total signal, can the result be trusted, as the bias will be only a few percent.

2. The bias is stemmed from distortion of the coma surface profile by convolution with PSF, which is probably uncorrectable due to noise. We recommend that the portion that is less perturbed by convolution and also has good SNR shall be used. High spatial resolution images of comets are required in order to avoid embedded biases as much as possible.

3. Large subsampling factors should be adopted to overcome inaccuracy of singularity replacement, and also to get rid of asymmetric artificial patterns otherwise present in residuals.

Acknowledgements

We appreciate help, suggestions and comments from Ariel Graykowski, David Jewitt, James Gerbs Bauer, Xinnan Du, and the anonymous referee. M.-T.H. is financially supported by David Jewitt through a NASA grant.

REFERENCES

[1] Bauer, J. M., Stevenson, R., Kramer, E., et al. 2015, ApJ, 814, 85

[2] Bauer, J. M., Grav, T., Fernández, Y. R., et al. 2017, AJ, 154, 53

[3] Buratti, B. J., Hicks, M. D., Soderblom, L. A., et al. 2004, Icarus, 167, 16

[4] de la Fuente Marcos, R., & de la Fuente Marcos, C. 2018, Research Notes of the American Astronomical Society, 2, 10

[5] Dohnanyi, J. S. 1969, J. Geophys. Res., 74, 2531

[6] Farnham, T., Kelley, M. S., Bodewits, D., & Bauer, J. M. 2017, AAS/Division for Planetary Sciences Meeting Abstracts #49, 49, 403.01

[7] Farnocchia, D., Chesley, S. R., Chodas, P. W., et al. 2014, ApJ, 790, 114

[8] Fernández, Y. R., Meech, K. J., Lisse, C. M., et al. 2003, Icarus, 164, 481

[9] Fernández, Y. R., Kelley, M. S., Lamy, P. L., et al. 2013, Icarus, 226, 1138

[10] Fernández, Y. R. 1999, Ph.D. Thesis, 6150

[11] Fernández, Y. R. 2002, Earth Moon and Planets, 89, 3

[12] Holtzman, J. A., Burrows, C. J., Casertano, S., et al. 1995, PASP, 107, 1065

[13] Hui, M.-T., Jewitt, D., & Clark, D. 2018, AJ, 155, 25

[14] Hui, M.-T. 2018, AJ in press

[15] Jewitt, D., Hui, M.-T., Mutchler, M., et al. 2017, ApJ, 847, L19

[16] Jewitt, D. C., & Meech, K. J. 1987, ApJ, 317, 992

[17] Jewitt, D. 2015, AJ, 150, 201

[18] Johansen, A., Mac Low, M.-M., Lacerda, P., & Bizzarro, M. 2015, Science Advances, 1, 1500109

[19] Królikowska, M., & Dybczyński, P. A. 2018, arXiv:1802.10380

[20] Lamy, P. L., Toth, I., & Weaver, H. A. 1998, A&A, 337, 945

[21] Lamy, P. L., Toth, I., Fernandez, Y. R., & Weaver, H. A. 2004, Comets II, eds. M. C. Festou, H. U. Keller, & H. A. Weaver, University of Arizona Press, Tucson, 745 pp., p.223

[22] Lamy, P. L., Toth, I., A'Hearn, M. F., Weaver, H. A., & Jorda, L. 2007, Icarus, 187, 132

[23] Lamy, P. L., Toth, I., & Weaver, H. A. 2014, ApJ, 794, L9

[24] Lamy, P. L., & Toth, I. 1995, A&A, 293,

[25] Lamy, P., & Toth, I. 2009, Icarus, 201, 674

[26] Li, J.-Y., A'Hearn, M. F., McFadden, L. A., & Belton, M. J. S. 2007, Icarus, 188, 195

[27] Li, J.-Y., Samarasinha, N. H., Kelley, M. S. P., et al. 2014, ApJ, 797, L8

[28] Li, J.-Y., Kelley, M. S. P., Samarasinha, N. H., et al. 2017, AJ, 154, 136

[29] Lisse, C. M., Fernández, Y. R., Kundu, A., et al. 1999, Icarus, 140, 189

[30] Lisse, C. M., Fernandez, Y. R., Reach, W. T., et al. 2009, PASP, 121, 968

[31] Meech, K. J., Kleyna, J. T., Hainaut, O., et al. 2017, ApJ, 849, L8

[32] O'Brien, D. P., & Greenberg, R. 2003, Icarus, 164, 334

[33] Schlichting, H. E., Fuentes, C. I., & Trilling, D. E. 2013, AJ, 146, 36

[34] van Dokkum, P. G. 2001, PASP, 113, 1420

[35] Weaver, H. A., Feldman, P. D., A'Hearn, M. F., & Arpigny, C. 1997, Science, 275, 1900

[36] Weaver, H. A., & Lamy, P. L. 1997, Earth Moon and Planets, 79, 17

CHAPTER 5

Conclusions and Future Work

The main purpose of this thesis is to improve our comprehension of physics of comets and active asteroids, in various aspects, from their non-gravitational effects to other physical properties. In this chapter, we give a summary of the thesis.

An introduction to comets and active asteroids is presented in Chapter 1, where we overviewed the historical development in understanding of these cometary objects, discussed their taxonomies and sources, and provided basic mathematical and physical knowledge and pertaining functions that would be extensively applied in subsequent chapters.

We presented a systematic study of the non-gravitational effects of the known active asteroids in Chapter 2. This work is crucial, because it was the first of such studies ever conducted. As discussed, neglecting potential non-gravitational effects of the small bodies will usually lead to incomplete or even distorted understanding of their past orbital evolution, and consequently misidentifying their source region. Now since we have determined (or at least constrained) the non-gravitational effects for the known active asteroids, more certainty about their histories is added. Overall, based on the available astrometry, only two of the active asteroids – 313P/Gibbs and 324P/La Sagra have shown statistically robust evidence of non-gravitational effects, which is consistent with the fact that the mass-loss rates of the active asteroids are generally much less than typical active comets. Given the result, conclusions from previous dynamical studies about the origin of the active asteroids, basically all of which ignored the non-gravitational forces, should still be valid. Besides, we reexamined parameters in the empirical momentum-transfer law by Marsden et al. (1973). We recommend adopting an anisothermal nucleus model to calculate the non-gravitational parameters for better physical plausibility, although the fit RMS does not necessarily reduce.

In Chapter 3, we discussed our CFHT and VST surveys for Kreutz-family comets and presented a detailed study about near-Sun comet C/2015 D1 (*SOHO*). The two specific surveys both unfortunately ended up with non-detection of any Kreutz-group comets with apparent magnitudes brighter than $m_{g'} \sim 24$ in the CFHT data, and $m_{r'} \sim 20$ in the VST data. Two bright satellite-detected Kreutz-group comets – *SOHO*-2388 and C/2012 U3 (*STEREO*) eluded our detection, although their sky uncertainty regions were confidently covered by our CFHT search, which means that either they brightened much more rapidly than suggested by Knight et al. (2010), or they underwent earlier outburst. During the VST survey, we unfortunately missed the chance of detecting a bright Kreutz-group comet *SOHO*-3069.

C/2015 D1 (*SOHO*) was the first sunskirting comet ever observed from the ground over the past half century. It disintegrated around perihelion, either due to the excessive interior thermal stress or subsequent rotational instability. The enormous mass-loss activity of the comet ($\dot{M}_{\rm N} \sim 10^5$ kg s^{-1}) caused a strong non-gravitational effect in its motion. Post-perihelion ground observatories witnessed its slowly expanding debris cloud. Multi-wavelength observations by *SOHO* together with morphologic monitoring from Xingming Observatory (plus non-detection of remaining nucleus fragments from Lowell Observatory) enabled an unprecedentedly detailed extensive study about the object in terms of its potential composition, dust properties, nucleus size, and disintegration mechanism, which greatly helps improve our understanding of poorly known near-Sun comets.

Statistics of nucleus-size distribution is suggestive of how planetesimals in the early solar system were formed. As a widely used tool for revelation of cometary nucleus sizes, the nucleus-extraction technique is examined systematically in Chapter 4. We therein reported an obvious systematic bias, which results from omission of the coma distortion by convolution with some PSFs. As a result, the specific bias trend is influenced by several factors such as the shape of PSF, the region for fitting comae, and the subsampling factor. According to our experiments, only when the nucleus signal occupies $\gtrsim$10% of the total around the central region, can the bias be minimal and the results revealed by this technique be trusted. Due to noise we doubt that the bias can be correctable. Thus we suggest application of the

technique only for weakly active comets, better in high spatial resolution images, if possible, otherwise the size-distribution statistics of cometary nuclei from this technique may well deviate from reality and lead to questionable conclusions due to the systematic bias.

In the future, the exploration of physics of comets and active asteroids will be continued. For the non-gravitational acceleration of the active asteroids, although we already presented the statistics, it is far from completion, because only loosely constrained non-gravitational parameters were set, usually due to unsatisfactory quality of the astrometric data. Now as the Gaia-DR2 was released in 2018 April, we expect considerable improvements to the astrometry of the active asteroids (Tholen et al. 2017; Lindegren et al. 2018), which greatly benefits orbit determination. Future generation sky surveys such as the Large Synoptic Survey Telescope (LSST) will discover more and fainter active asteroids, which will likely improve our understanding of their physical properties, their origin, and perhaps even untangle the relation between them and water on the Earth.

We will also continue our (short-term and long-term) ground-based surveys for near-Sun comets, particularly the Kreutz-family comets, in the future. Thus far there is no scheduled or planned space mission in the near future that may have similar capacities to the LASCO onboard *SOHO*. So, we may well have a great loss in terms of continuation of monitoring of near-Sun comets once *SOHO* ceases functioning. We also expect some bright members to be discovered by the LSST at large solar elongations.

Due to the existence of the bias in the nucleus-extraction technique, we have yet to establish an unbiased picture about evolutionary paths of comets. Because of the limitation of the technique, we may have to stick to space telescopes such as *HST* and the *James Webb Space Telescope* (*JWST*; e.g., Kelley et al. 2016) for continuous high resolution imaging of weakly active comets. At this moment, we have not yet accumulated a sufficient number of samples with the required quality for performing coma removal. Alternatively, we can make effort to devise some novel image processing techniques to correct for the bias. If this can be accomplished, results from previous works can be debiased and much better comprehension about the evolution of comets will be achieved. Nevertheless we should also revisit other existing methods or develop new ones for characterisation of nucleus sizes of comets, lest

we are misled by the bias in the nucleus-extraction technique. For instance, one can first identify dormant comets amongst asteroids in dynamically comet-like orbits by detection of associated meteor streams (Ye et al. 2017), and then establish their size statistics.

We are aware of several future unmanned space missions to some of the comets and active asteroids in the coming decades. Detailed in situ measurements of these primitive objects will tremendously help our understanding of them and tackle remaining unsolved puzzles around them, and perhaps even around the whole solar system. The bright future will certainly witness boosts in our knowledge regarding physics of comets and active asteroids.

REFERENCES

[1] Kelley, M. S. P., Woodward, C. E., Bodewits, D., et al. 2016, PASP, 128, 018009

[2] Knight, M. M., A'Hearn, M. F., Biesecker, D. A., et al. 2010, AJ, 139, 926

[3] Lindegren, L., Hernandez, J., Bombrun, A., et al. 2018, arXiv:1804.09366

[4] Marsden, B. G., Sekanina, Z., & Yeomans, D. K. 1973, AJ, 78, 211

[5] Tholen, D. J., Ramanjooloo, Y., Fohring, D., Hung, D., & Claytor, Z. 2017, AAS/Division for Planetary Sciences Meeting Abstracts #49, 49, 112.06

[6] Ye, Q.-Z., Brown, P. G., & Pokorný, P. 2016, MNRAS, 462, 3511

APPENDIX A

Asymmetry Coefficient of Spherical Cometary Nucleus

When a comet is close to the Sun, sublimation dominantly consumes the received power from the Sun [see Equation (1.11)]. If we assume that the latent heat is not a function sensitive to temperature T, then the local outgassing flux of the sublimating substance is approximately proportional to the local solar illumination:

$$\frac{(1-A_{\mathrm{B}})\, r_{\oplus}^{2} S_{\odot}}{r_{\mathrm{h}}^{2}} \cos\zeta \approx L\,(T)\, \mathscr{U}\, m_{\mathrm{H}} Z\,(T)\,. \tag{A.1}$$

We assume a perfectly spherical cometary nucleus having radius R_{N}. Let the area of surface element be $\mathrm{d}\mathfrak{S}$. The local outgassing flow exerts a momentum on the nucleus as

$$\mathrm{d}\mathbf{p} = -\mathscr{U}\, m_{\mathrm{H}} Z v \hat{\mathbf{n}} \mathrm{d}\mathfrak{S}, \tag{A.2}$$

where $\hat{\mathbf{n}}$ is the local surface normal. Combined with Equation (A.1), the total momentum driven by all the outgassing material is the integration over the whole nucleus surface

$$\begin{aligned}
\mathbf{p} &\equiv \int_{\mathfrak{S}} \mathrm{d}\mathbf{p} \\
&= \int_{\mathfrak{S}} -\mathscr{U}\, m_{\mathrm{H}} Z v \hat{\mathbf{n}} \mathrm{d}\mathfrak{S} \\
&\approx -\frac{v\,(1-A_{\mathrm{B}})\, r_{\oplus}^{2} S_{\odot}}{L r_{\mathrm{h}}^{2}} \int_{\mathfrak{S}} \hat{\mathbf{n}} \cos\zeta \mathrm{d}\mathfrak{S}.
\end{aligned} \tag{A.3}$$

Here we have assumed that the outgassing speed is independent from the location on the nucleus surface. Obviously, because of the symmetry, the total net momentum is directed in the heliocentric radial direction, whose unit vector is $\hat{\mathbf{e}}_{\mathrm{R}}$ (c.f. Figure 1.5, note that $\zeta = \pi - \psi$).

Equation (A.3) then yields

$$\begin{aligned}\mathbf{p} &\approx \frac{R_{\mathrm{N}}^2 v\,(1-A_{\mathrm{B}})\,r_{\oplus}^2 S_{\odot}}{L r_{\mathrm{h}}^2}\hat{\mathbf{e}}_{\mathrm{R}} \int_0^{2\pi} \mathrm{d}\xi \int_0^{\pi/2} \mathrm{d}\zeta \sin\zeta \cos^2\zeta \\ &= \frac{2\pi R_{\mathrm{N}}^2 v\,(1-A_{\mathrm{B}})\,r_{\oplus}^2 S_{\odot}}{3 L r_{\mathrm{h}}^2}\hat{\mathbf{e}}_{\mathrm{R}}. \end{aligned} \tag{A.4}$$

Similarly, with Equation (A.1), we can express the total production rate as

$$\begin{aligned} Q &= \int_{\mathfrak{S}} Z \mathrm{d}\mathfrak{S} \\ &\approx \frac{\pi R_{\mathrm{N}}^2 v\,(1-A_{\mathrm{B}})\,r_{\oplus}^2 S_{\odot}}{L \mathscr{U} m_{\mathrm{H}} r_{\mathrm{h}}^2}. \end{aligned} \tag{A.5}$$

The effective velocity of the outgassing substance is

$$\begin{aligned} \langle \mathbf{v} \rangle &\equiv -\frac{\mathbf{p}}{\mathscr{U} m_{\mathrm{H}} Q} \\ &\approx -\frac{2}{3} v \hat{\mathbf{e}}_{\mathrm{R}}. \end{aligned} \tag{A.6}$$

Therefore, we obtain $\kappa \approx 2/3$ as the asymmetry coefficient for the spherical nucleus. Realistically, we expect $2/3 < \kappa < 1$, as the outgassing flux is intensified with a higher surface temperature. The minus sign in Equation (A.6) means that the effective velocity is directed towards the heliocentre. In general cases, cometary nuclei are found to have activity concentrated about the subsolar point. As such, we expect that $\langle \mathbf{v} \rangle \cdot \hat{\mathbf{e}}_{\mathrm{R}} < 0$ is always satisfied, which indicates the radial non-gravitational parameter $A_1 \geq 0$. Otherwise the adopted non-gravitational force model is not physically meaningful. For instance, if one simplistically applies a symmetric non-gravitational force model on a comet whose activity is strongly asymmetric about perihelion, it will be possible to obtain $A_1 < 0$.

APPENDIX B

Pseudo-Keplerian Motion of Cometary Dust in Repulsive Inverse Square Force Field

In the first-order approximation, after decoupled from the gas drag, a cometary dust grain is driven by the gravitational force of the Sun and the solar radiation pressure force. Since both forces are directed radially and vary as r^{-2}, where r is the heliocentric distance of the dust grain, so is the net force. Conveniently, the ratio between the magnitudes of the solar radiation pressure force and the solar gravity is denoted as β. The motion of a dust grain with $\beta < 1$ can be readily solved by treating it subjected to a reduced gravitational field and applying traditional Keplerian orbit mechanics, whereas for $\beta = 1$ the particle simply has the uniform linear motion. For $\beta > 1$, a repulsive force comes into power and nevertheless accelerates the particle to escape the solar system. We are unaware of any literatures that illustrate the motion under such a force field with close comparison to the traditional Keplerian motion, and therefore herein we make efforts to do so.

A polar coordinate system is adopted, in which the origin is at the heliocentre, r is the radius, and ϑ is the angular component. Starting from the Lagrangian mechanics, we obtain

$$\ddot{r} - r\dot{\vartheta} = \frac{\mathscr{M}}{r^2}, \tag{B.1}$$

$$r^2\dot{\vartheta} = h, \tag{B.2}$$

where $\mathscr{M} = (\beta - 1)\, GM_\odot$, G is the gravitational constant, $M_\odot$ is the solar mass, and h is the magnitude of the specific angular momentum of the cometary grain. Now eliminate $\dot{\vartheta}$ with Equation (B.2), and introduce $u \equiv 1/r$. Equation (B.1) can be turned into the following inhomogeneous second-order linear ordinary differential equation:

$$\frac{\mathrm{d}^2 u}{\mathrm{d}\vartheta^2} + u = -\frac{\mathscr{M}}{h^2},$$

whose solution can be expressed in the following formalism:

$$u = \frac{\mathscr{M}}{h^2}\left[e\cos\left(\vartheta - \omega\right) - 1\right], \tag{B.3}$$

where e and ω are two constants that can be fixed in accordance with the initial condition. Now use Equation (B.3) to yield r:

$$r = -\frac{h^2/\mathscr{M}}{1 - e\cos\left(\vartheta - \omega\right)}. \tag{B.4}$$

Obviously, the described trajectory is a hyperbola with one of its foci at the heliocentre, which is the origin. However, the branch of the hyperbola is not the same one as in the attractive scenario. Let q denote its perihelion distance. Then we have $q \equiv r_{\min} = -a\left(1 + e\right)$, where $a < 0$ is the semimajor axis of the hyperbola, and $h = \sqrt{-\mathscr{M}\, a\left(e^2 - 1\right)}$.

Now we proceed to find r and ϑ as functions of time. We again combine Equations (B.1) and (B.2) and get

$$\ddot{r} - \frac{h}{r^3} = -\frac{\mathscr{M}}{r^2}.$$

Since we can write $\ddot{r}$ as

$$\ddot{r} = \frac{\mathrm{d}\dot{r}}{\mathrm{d}r}\dot{r},$$

by combining the above two equations, we find

$$\dot{r}\mathrm{d}\dot{r} = \left(\frac{h^2}{r^3} + \frac{\mathscr{M}}{r^2}\right)\mathrm{d}r.$$

Integrating both sides yields:

$$\dot{r}^2 = -\frac{2\mathscr{M}}{r} - \frac{h^2}{r^2} + \mathscr{K}.$$

Here, $\mathscr{K}$ is a constant, which can be determined by examining the particle at perihelion. Thereby we find $\mathscr{K} = -\mathscr{M}/a$. Hence

$$\dot{r}^2 = -\frac{2\mathscr{M}}{r} - \frac{h^2}{r^2} - \frac{\mathscr{M}}{a}. \tag{B.5}$$

Note that one can write the velocity of the particle in terms of unit vectors $\hat{\mathbf{e}}_{\mathrm{R}}$ and $\hat{\mathbf{e}}_{\mathrm{T}}$ as

$$\mathbf{V} = \dot{r}\hat{\mathbf{e}}_{\mathrm{R}} + r\dot{\vartheta}\hat{\mathbf{e}}_{\mathrm{T}}.$$

Combining with Equation (B.2), as a byproduct we obtain the *pseudo-vis-viva equation* in the repulsive force field:

$$V^2 = -\mathscr{M}\left(\frac{2}{r} + \frac{1}{a}\right), \tag{B.6}$$

which closely resembles the one in the traditional Keplerian mechanics.

We now transform Equation (B.5) into the following form

$$\sqrt{-\frac{\mathscr{M}}{a^3}}\mathrm{d}t = -\frac{r\mathrm{d}r}{a\sqrt{(r+a)^2 - a^2e^2}}. \tag{B.7}$$

Now an auxiliary parameter E is introduced, which is defined by

$$r = -a\left(e\cosh E + 1\right). \tag{B.8}$$

Hence, Equation (B.7) can be written as

$$\sqrt{-\frac{\mathscr{M}}{a^3}}\mathrm{d}t = \left(e\cosh E + 1\right)\mathrm{d}E,$$

the integral of which yields

$$\sqrt{-\frac{\mathscr{M}}{a^3}}\left(t - t_{\mathrm{P}}\right) = e\sinh E + E, \tag{B.9}$$

where t_{P} is the perihelion epoch. One can immediately notice the similarity to the traditional Kepler's equation for hyperbolic orbits. Following the convention, we also term the quantity defined by the left-hand side of Equation (B.9) the mean anomaly M, whose quantity can be obtained once $t - t_{\mathrm{P}}$ is given. Then iterative algorithms such as the Newton-Raphson method can be applied to solve for E from the transcendental equation. With Equations (B.8) and (B.4), r and ϑ can be obtained successively.

Although we have completed the task, herein it is also interesting to express ϑ as a function of E. For simplicity, let $\theta = \vartheta - \omega$, which can be called, by following the traditional Keplerian mechanics, the true anomaly of the cometary dust. Combining Equations (B.4) and (B.8), we have

$$\cos\theta = \frac{e + \cosh E}{1 + e\cosh E}, \tag{B.10}$$

or after applying the half-angle formulae, then

$$\tan\frac{\theta}{2} = \sqrt{\frac{e-1}{e+1}}\tanh\frac{E}{2}. \tag{B.11}$$

Now we can conclude that the equations describing the motion of cometary dust driven by the repulsive central force are remarkably similar to those in the traditional Keplerian mechanics, with mere differences of flipping signs. We thus term such motion *Pseudo-Keplerian*.

APPENDIX C

Conversion from Cartesian State Vector to Orbital Elements

C.1 Purpose

Herein we present recipes for conversion of orbital elements from Cartesian state vectors under the inverse square central-force field, attractive and repulsive included. For brevity, hereafter the central forces mentioned are all referred to inverse square forces.

C.2 Initial Condition

A Cartesian state vector is comprised of the following two components:

1. position vector: $\mathbf{r} = X\hat{\mathbf{e}}_x + Y\hat{\mathbf{e}}_y + Z\hat{\mathbf{e}}_z$,
2. velocity vector: $\mathbf{V} = V_x\hat{\mathbf{e}}_x + V_y\hat{\mathbf{e}}_y + V_z\hat{\mathbf{e}}_z$,

which are both at some specific epoch. The origin of the reference system is set to be the heliocentre, whose reference plane is the ecliptic and mean equinox of reference epoch J2000, such that the xy-plane is the one of the Earth's orbit at the reference epoch, x-axis is out along ascending node of instantaneous plane of the Earth's orbit and the Earth's mean equator at the reference epoch, and z-axis is perpendicular to the xy-plane in the directional sense of Earth's north pole at the reference epoch. The three unit vectors are denoted as $\hat{\mathbf{e}}_x$, $\hat{\mathbf{e}}_y$, and $\hat{\mathbf{e}}_z$.

C.3 Central-Force Field

The central-force field is described by

$$\ddot{\mathbf{r}} = (\beta - 1)\,\frac{GM_{\odot}}{r^3}\mathbf{r}, \tag{C.1}$$

where β is the ratio between the solar radiation force and the gravitational force due to the Sun, G is the gravitational constant, and $M_{\odot}$ is the solar mass. If a dust particle is not too light, it has $\beta < 1$, where the particle is subjected to a reduced gravity-like force. Otherwise, if $\beta > 1$, the particle is driven by a repulsive central force. For simplification, we denote

$$\mathscr{M} = |1 - \beta|\, GM_{\odot}, \tag{C.2}$$

such that we have

$$\ddot{\mathbf{r}} = \begin{cases} -\dfrac{\mathscr{M}}{r^3}\mathbf{r} & \text{, if } \beta < 1 \\ \dfrac{\mathscr{M}}{r^3}\mathbf{r} & \text{, otherwise} \end{cases}. \tag{C.3}$$

C.3.1 Attractive Central Force

The steps for converting the Cartesian vector to the orbital elements are listed as follows.

1. Calculate the specific angular momentum $\mathbf{h}$:

$$\mathbf{h} = \mathbf{r} \times \mathbf{V}. \tag{C.4}$$

2. Calculate the eccentricity vector $\mathbf{e}$

$$\begin{aligned} \mathbf{e} &= \frac{\mathbf{V} \times \mathbf{h}}{\mathscr{M}} - \frac{\mathbf{r}}{r} \\ &= \left(\frac{V^2}{\mathscr{M}} - \frac{1}{r}\right)\mathbf{r} - \frac{\mathbf{V} \cdot \mathbf{r}}{\mathscr{M}}\mathbf{V}, \end{aligned} \tag{C.5}$$

   whence the eccentricity e can be easily obtained from $e = \sqrt{\mathbf{e} \cdot \mathbf{e}}$.

3. Compute the orbital inclination i from

$$i = \arccos\left(\frac{\mathbf{h} \cdot \hat{\mathbf{e}}_z}{h}\right). \tag{C.6}$$

   One ought to ensure that i always lies within $0 \leq i \leq \pi$ in radians.

4. Now compute the longitude of ascending node Ω:

$$\begin{aligned}\Omega &= \arccos\left[\frac{(\hat{\mathbf{e}}_z \times \mathbf{h}) \cdot \hat{\mathbf{e}}_x}{|\hat{\mathbf{e}}_z \times \mathbf{h}|}\right] \\ &= \arccos\left[\frac{\mathbf{h} \cdot \hat{\mathbf{e}}_y}{\sqrt{\mathbf{h}^2 - (\mathbf{h} \cdot \hat{\mathbf{e}}_z)^2}}\right]. \end{aligned} \tag{C.7}$$

It must satisfy $0 \leq \Omega \leq 2\pi$. Hence, if $\mathbf{h} \cdot \hat{\mathbf{e}}_x < 0$, then $\Omega = 2\pi - \Omega$.

5. Calculate the argument of perihelion ω as follows:

$$\omega = \arccos\left[\frac{(\hat{\mathbf{e}}_z \times \mathbf{h}) \cdot \mathbf{e}}{|\hat{\mathbf{e}}_z \times \mathbf{h}|\, e}\right]. \tag{C.8}$$

If $\mathbf{e} \cdot \hat{\mathbf{e}}_z < 0$ then $\omega = 2\pi - \omega$.

6. Obtain the perihelion distance q:

$$q = \frac{h^2}{\mathscr{M}\,(e+1)}. \tag{C.9}$$

If the trajectory is non-parabolic, i.e. $e \neq 1$, one can further compute the semimajor axis of the orbit, $a = q/\,(1-e)$.

7. Solve for the true anomaly, θ:

$$\theta = \arccos\left(\frac{\mathbf{r} \cdot \mathbf{e}}{re}\right). \tag{C.10}$$

If $\mathbf{r} \cdot \mathbf{V} < 0$, $\theta = 2\pi - \theta$.

8. Now calculate the eccentric anomaly E. Note that there are three cases: elliptic, parabolic and hyperbolic.

$$E = \begin{cases} \arccos\left(\dfrac{e + \cos\theta}{1 + e\cos\theta}\right) & \text{, if } e < 1 \\ \tan\dfrac{\theta}{2} & \text{, if } e = 1 \\ \operatorname{arccosh}\left(\dfrac{e + \cos\theta}{1 + e\cos\theta}\right) & \text{, otherwise} \end{cases}, \tag{C.11}$$

Alternatively, the eccentric anomaly can be solved from the following way:

$$E = \begin{cases} \arccos\left[\frac{1}{e}\left(1-\frac{r}{a}\right)\right] & \text{, if } e<1 \\ \sqrt{\frac{r}{q}-1} & \text{, if } e=1 \\ \operatorname{arccosh}\left[\frac{1}{e}\left(1+\frac{r}{a}\right)\right] & \text{, otherwise} \end{cases} . \tag{C.12}$$

9. Now one can solve for the mean anomaly M:

$$M = \begin{cases} E - e\sin E & \text{, if } e<1 \\ E + \frac{1}{3}E^3 & \text{, if } e=1 \\ e\sinh E - E & \text{, otherwise} \end{cases} . \tag{C.13}$$

For elliptical orbits, the mean anomaly can be set to some specific range, e.g. $0 \leq M \leq 2\pi$, or $-\pi \leq M \leq +\pi$. Otherwise, the value of M must not be altered because the orbits are not periodic.

C.3.2 Repulsive Central Force

The conversion under repulsive central forces is expected to bear many similarities to the attractive scenario. Equation (C.6), and (C.7) should both remain unchanged because $\mathbf{h}$ is unaffected. The way to obtain the true anomaly is unaltered from Equation (C.10), but the formalism of $\mathbf{e}$ is different. Accordingly the remaining steps all need to be adjusted. First of all, let us derive the formalism of $\mathbf{e}$ under the repulsive-force field.

To do this, we differentiate $\mathbf{V}\times\mathbf{h}$ with respect to time t. Note that we have $\dot{\mathbf{h}} = \mathbf{0}$ due to the conservation of the angular momentum. In combine with Equation (C.3), we can then obtain

$$\begin{aligned} \frac{\mathrm{d}}{\mathrm{d}t}(\mathbf{V}\times\mathbf{h}) &= \frac{\mathscr{M}}{r^3}\mathbf{r}\times\mathbf{h} \\ &= -\frac{\mathscr{M}h}{r^2}\hat{\mathbf{e}}_{\mathrm{T}} \\ &= -\mathscr{M}\frac{\mathrm{d}}{\mathrm{d}t}\hat{\mathrm{e}}_{\mathrm{R}}, \end{aligned}$$

therefore, we yield

$$\mathbf{V} \times \mathbf{h} + \mathscr{M} \frac{\mathbf{r}}{r} = \mathbf{C}_{\mathrm{r}}, \tag{C.14}$$

where $\mathbf{C}_{\mathrm{r}}$ is a constant to be determined by initial conditions. With the pseudo-vis-viva equation (B.6) for the repulsive-force field:

$$V^2 = \mathscr{M} \left(\frac{1+e}{q} - \frac{2}{r} \right), \tag{C.15}$$

we can find $\mathbf{C}_{\mathrm{r}} = \mathscr{M}\,\mathbf{e}$ by examining the condition at perihelion. Therefore, we obtain

$$\begin{aligned} \mathbf{e} &= \frac{\mathbf{V} \times \mathbf{h}}{\mathscr{M}} + \frac{\mathbf{r}}{r} \\ &= \left(\frac{V^2}{\mathscr{M}} + \frac{1}{r} \right) \mathbf{r} - \frac{\mathbf{V} \cdot \mathbf{r}}{\mathscr{M}} \mathbf{V}, \end{aligned} \tag{C.16}$$

as the formalism of the eccentricity vector under the repulsive-force field, which is very similar to Equation (C.5).

Now we present the complete steps in the following.

1. Calculate the specific angular momentum $\mathbf{h}$ with Equation (C.4)

2. Calculate the eccentricity e from Equation (C.16).

3. Compute the orbital inclination i with Equaion (C.6).

4. Compute the longitude of ascending node Ω with Equation (C.7).

5. Calculate the argument of perihelion ω from Equation (C.8).

6. Solve the perihelion distance q from

$$q = \frac{h^2}{\mathscr{M}\,(e-1)}. \tag{C.17}$$

7. Solve true anomaly with Equation (C.10).

8. Then proceed to calculate eccentric anomaly:

$$E = \operatorname{arccosh} \left(\frac{e - \cos\theta}{e\cos\theta - 1} \right), \tag{C.18}$$

or, from the following way:

$$E = \operatorname{arccosh}\left[-\frac{1}{e}\left(1+\frac{r}{a}\right)\right]. \tag{C.19}$$

9. Finally, calculate the mean anomaly:

$$M = E + e\sinh E. \tag{C.20}$$

C.3.3 Force-Free Field

There is a special case when the dust particle has $\beta = 1$, where it moves in a uniform rectilinear trajectory, abstractly, $e = +\infty$. If the position vector $\mathbf{r}$ is neither parallel nor anti-parallel to the velocity $\mathbf{V}$, elements q, i, Ω, ω, and f are still well-defined. The steps for computing these elements are given as follows.

1. Introduce the perihelion vector:

$$\mathbf{q} = \mathbf{r} - \frac{\mathbf{r}\cdot\mathbf{V}}{V^2}\mathbf{V}, \tag{C.21}$$

   whereby we can obtain the perihelion distance $q = |\mathbf{q}|$.

2. Calculate the specific angular momentum $\mathbf{h}$ with Equation (C.4).

3. Compute the argument of perihelion ω from

$$\omega = \arccos\left[\frac{(\hat{\mathbf{e}}_z \times \mathbf{h})\cdot\mathbf{q}}{|\hat{\mathbf{e}}_z \times \mathbf{h}|\, q}\right]. \tag{C.22}$$

   If $\mathbf{q}\cdot\hat{\mathbf{e}}_z < 0$ then $\omega = 2\pi - \omega$.

4. Calculate the inclination i from Equation (C.6).

5. Calculate the longitude of ascending node from Equation (C.7).

6. Compute true anomaly

$$\theta = \arccos\left(\frac{\mathbf{r}\cdot\mathbf{q}}{qr}\right). \tag{C.23}$$

   If $\mathbf{r}\cdot\mathbf{V} < 0$ then $\theta = 2\pi - \theta$.

We should note that if one's intention is to compute state vectors at any desired specific epoch, there is no need to compute the orbital elements for dust particles in the force-free field.

List of Symbols

A Composite non-gravitational parameter

A_{B} Bond albedo

A_{p} Geometric albedo

A_j $(j = 1, 2, 3)$ Non-gravitational parameters in the RTN coordinate system

$\mathcal{A}$ Magnitude of non-gravitational acceleration

$\mathcal{A}_{\mathrm{R}}$, $\mathcal{A}_{\mathrm{T}}$, $\mathcal{A}_{\mathrm{N}}$ Components of non-gravitational acceleration in the RTN coordinate system

$\mathfrak{a}$ Dust grain radius

a Orbital semimajor axis

C_{e} Effective cross-section

c Speed of light

D_{N} Nucleus diameter

E Eccentric anomaly

$\hat{\mathbf{e}}$ Unit vector, $(\hat{\mathbf{e}}_x, \hat{\mathbf{e}}_y, \hat{\mathbf{e}}_z)$ in the Cartesian coordinates, $(\hat{\mathbf{e}}_{\mathrm{R}}, \hat{\mathbf{e}}_{\mathrm{T}}, \hat{\mathbf{e}}_{\mathrm{N}})$ in the RTN system

$\mathcal{E}_{\mathrm{M}}$ Mass erosion ratio

e Orbital eccentricity

G Gravitational constant

g Empirical momentum-transfer law

i Inclination of orbital plane

k_{B} Boltzmann constant

k_{C}	Scaling factor for coma brightness profile
k_{N}	Scaling factor for cometary nucleus
L	Latent heat
M	Mean anomaly
M_{N}	Mass of nucleus
$M_{\odot}$	Solar mass
m_{H}	Mass of hydrogen atom
m_{λ}	Apparent λ-band magnitude
$m_{\odot,\lambda}$	Apparent λ-band magnitude of Sun
P	Orbital period
Q	Molecular production rate
q	Perihelion distance
R_{N}	Nucleus radius
$R_{\odot}$	Solar radius
r	Distance from origin, corresponding vector denoted in bolded font
r_{h}	Heliocentric distance, corresponding vector denoted in bolded font
$S_{\odot}$	Solar constant
$\mathcal{S}$	Subsampling factor
T	Temperature
T_{J}	Jupiter Tisserand invariant
t	Time

t_{P}	Epoch of perihelion passage
$\mathscr{U}$	Molecular weight
V	Magnitude of heliocentric velocity, corresponding vector in bolded font
v	Ejection speed of cometary dust grain
v_{th}	Thermal speed
α	Phase angle
β	Ratio between solar radiation pressure force and solar gravitational force
γ	Slope index of cometary dust-size distribution, **OR** of coma surface brightness profile
Δ	Observer-object distance
ϵ	Emissivity
η	Ratio between cometary nucleus flux and total flux enclosed by common photometric aperture
θ	True anomaly, **OR** azimuthal angle in polar coordinates
κ	Collimation efficiency of mass loss
ρ	Linear radius of photometric radius, **OR** radial distance to origin
ρ_{d}	Bulk density of cometary dust grain
σ_{SB}	Stefan-Boltzmann constant
ϕ	Phase function
Ω	Longitude of ascending node
ω	Argument of perihelion